Development of a diagnostics model for the GEnx-1B turbofan engine using on-wing performance data

M. Otten

Technische Universiteit Delft

TU Delft

Development of a diagnostics model for the GEnx-1B turbofan engine using on-wing performance data

by

M. Otten

to obtain the degree of Master of Science
at the Delft University of Technology,
to be defended publicly on Friday December 10, 2013 at 13:00 PM.

Student number:	4378377	
Project duration:	December 1, 2020 – December 10, 2021	
Thesis committee:	Prof. dr. ir. P. Colonna,	TU Delft, chair
	Dr. ir. W. P. J. Visser,	TU Delft, supervisor
	Ir. P. C. Roling,	TU Delft
	Ir. J. Regueiro	KLM Engine Services, supervisor

This thesis is confidential and cannot be made public until December 10, 2023.

TU Delft

Preface

This master thesis concludes my time as a student at the Technical University of Delft. I'm grateful for the chance to conduct this thesis at KLM Engineering Maintenance. The presence of inspiring people and fascinating engines motivated me everyday as I walked in.

During this thesis, I learned tremendously much about aircraft engines and the maintenance industry. This would not have been possible without the help from others. First of all, I would like to thank Wilfried Visser for his guidance, supervision and feedback throughout this project. I would also like to thank all my colleagues at KLM for the engineering advise, refreshing coffee breaks or the walks around the hangers. Especially, I would like to thank Juan Regueiro for guiding me over the past year. Our weekly meetings and Juan's extensive knowledge of gas turbine modelling always helped me gain valuable insights during this year-long period. Furthermore, I would like to express my gratitude to my family and friends for supporting me over the years and making my student life an unforgettable experience.

Michiel Otten
November 2021

Executive summary

Turbofan engine maintenance costs can be significantly reduced if detailed deterioration information is known a priori. With a thermodynamic gas path analysis (GPA) engine model, the deterioration levels of the individual gas turbine components can be analyzed. KLM Engine Services (ES) uses the GPA software package of the Gas Turbine Simulation Program (GSP) to estimate deterioration. The accuracy of GPA results depends strongly on the accuracy of the engine models.

KLM ES provides maintenance for multiple engines, including the General Electric GEnx-1B engine. This is a modern high bypass ratio turbofan engine that is used on the Boeing-787 Dreamliner. The number of gas path sensors is reduced for modern engines, introducing challenges in developing accurate GPA models. To compensate for the reduction in gas path sensors, a greater quantity of on-wing performance data is stored in the Continuous Engine Operating Data (CEOD) database. CEOD contains gas path sensor data as well as information on the secondary performance parameter settings like variable geometry, bleed flows, active clearance control and power off-take.

At KLM ES, a GEnx-1B GPA model has been developed. This model accurately matches the GEnx-1B gas path measurements for take-off conditions. However, the GEnx-1B engine components operate differently at cruise conditions due to divergent secondary performance parameter settings. Consequently, the secondary performance parameter effects need to be accounted for to perform accurate GPA at cruise conditions. The objective of this thesis is to increase the accuracy of the GEnx-1B engine model for cruise conditions by accounting for secondary performance parameter effects.

To identify the effect of the individual secondary performance parameters, this thesis proposes a method to determine the relationships between the individual secondary performance parameter settings and the consequent performance deviations of the components. Combining a differential algorithm optimization scheme with on-wing engine operating data has resulted in a novel approach to accurately determine these relationships.

The method has been verified with simulated data from a standard GSP turbofan model. The results indicate the algorithm can accurately determine the relationships between secondary performance parameter settings and component performance deviation, which can be used to increase overall turbofan model accuracy.

The method has been validated using GEnx-1B on-wing cruise data from a good condition engine. First, the algorithm has been applied using the baseline GEnx-1B model. However, unrealistic results were obtained. This could be attributed to large deviations in the fan and low pressure compressor (LPC) component sub-models, so these had to be corrected and made more accurate. With the improved GEnx-1B model, realistic relationships between secondary performance and component performance deviation were obtained that are in line with public data. After embedding these relationships in the improved GEnx-1B model, the modelling error was reduced by 65%, clearly indicating the validity and accuracy of the relationships. Applying this new model on performance data from different GEnx-1B engines also resulted in a modelling error decrease of 61%, implying the applicability of the relationships for all GEnx-1B engines.

With the new model, GPA was performed on historical GEnx-1B engine data and compared with GPA using the original less accurate model. The new GPA results show better correspondence with known engine history information such as compressor washes and a turbine blade failure. Also, the root mean square error of the GPA results was reduced by 8%.

The results presented in this thesis indicate that the algorithm can accurately determine relationships between secondary performance parameters and component performance deviation at cruise conditions. Accounting for these relationships in engine models increases model accuracy and consequently GPA accuracy, thereby providing more reliable and accurate information for maintenance decision making.

Contents

List of Figures

List of Tables

Nomenclature

Acronyms

LHV	Lower Heating Value
AM	Adaptive modelling
CEOD	Continuous Engine Operating Data
DE	Differential Algorithm
DOC	Direct operating costs
ES	Engine Services
FCM	Fault-Correction Matrix
FOD	Foreign Object Damage
GPA	Gas Path Analysis
GSP	Gas Turbine Simulation Program
HPC	High Pressure Compressor
HPT	High Pressure Turbine
ICM	Influence-Coefficient Matrix
IGV	Inlet Guide Vanes
ISA	International Standard Atmosphere values
LPC	Low Pressure Compressor
LPS	Low Pressure System: fan and LPC
LPT	Low Pressure Turbine
MOPA	Multiple operating point analysis
MOPA-EA GPA	Multi Operating Point Evolutionary Algorithm based Gas Path Analysis
MRO	Maintenance, repair and overhaul
NLR	National Aerospace Laboratory
OEM	Original equipment manufacturer
SFC	Specific Fuel Consumption
SPP	Secondary Performance Parameter
TBV	Transient Bleed Valve
VBV	Variable Bleed Valve
VSFG	Variable Frequency Starter Generators
VSV	Variable Stator Vanes

Greek Symbols

η	Efficiency
γ	Heat capacity ratio
ρ	Density

Roman Symbols

$\bar{E}$	Error vector
$\bar{S}$	State vector
$\dot{m}$	Mass flow
ω	Spool speed
A_n	Area perpendicular to the flow direction
c	Velocity
c_p	Isobaric specific heat
c_v	Isochoric specific heat
h	Enthalpy
I	Moment of inertia
J	Jacobian
M	Mass flow
N	Rotational speed
P	Power
p	Pressure
Q	Heat addition
R	Gas constant
T	Temperature
t	Time
V	Internal volume
W	Work
C	On-wing ambient and operating condition data
DP	Design point
MEAS	Number of measurements
NP	Number of target vectors
OD	Off-design
OP	Number of operating points
PD	Performance deviation
rms	Root mean square

S Secondary performance parameter data

Z On-wing measurement data

Subscripts

0 Total property

abs Absorbed

amb Ambient

$comp$ Compressor

$crit$ Critical

del Delivered

f Fuel

i Inlet

in Inflow property

is isentropic

j Nozzle

$meas$ Measurement parameter

$mech$ Mechanical

$model$ Parameter from model

out Outflow property

$turb$ Turbine

OP Number of operating points

1 Introduction

Since the introduction of the high bypass turbofan, the commercial air travel market has revolutionised. Due to its high efficiency and power-to-weight ratio, the high bypass ratio turbofan was able to reduce the operating costs of airliners and introduce air travel to a larger public. For modern airliners, the competition is fierce and the reduction of direct operating costs (DOC) is an important driver for a competitive position in the industry.

A key component of the direct operating costs is the maintenance of the turbofan engines. This maintenance is provided by maintenance, repair, and overhaul (MRO) facilities. The original equipment manufacturers (OEM) such as General Electric and Rolls Royce are providers of this service, but also the airliners have their maintenance divisions. KLM is one of the airlines with a large maintenance department. Together with Air France, they form Air France Industries KLM Engineering & Maintenance.

Within KLM Engineering Maintenance, Engine Services (ES) is one of the six maintenance divisions. Engine Services is currently performing overhauls on the KLM fleet engines as well as on engines from other airlines. The capabilities available within ES are performing maintenance on the large list of aircraft engines, among which the CF6-80C2, CF6-80E1, CFM-56-7B, GEnx-1B.

In the past, the MRO business performed maintenance on these engines on a scheduled basis. The desire to lower DOC from the airlines led to a new strategy. Diagnostics for engine performance was introduced. This strategy is based on the identification of engine failures as well as the monitoring of engine degradation. The goal is reducing the unscheduled line maintenance as well as impacting the off-wing maintenance by improved scheduling of maintenance, overhauls, and work-scoping, as this would lead to reduced DOC [56].

1.1. Context & Problem Statement

At KLM Engine Services, engine diagnostics is researched using the Gas Turbine Simulation Program (GSP). This software enables KLM to perform gas path analysis (GPA) to help determine deterioration levels in individual components of gas turbines based on performance data. This process is mainly applied to test cell data for engines with a large number of sensors. In more modern engines, the number of sensors is reduced by the OEM. This introduces challenges in performing accurate GPA. These engines do however record Continuous Engine Operating Data (CEOD).

Within KLM, a GEnx-1B GPA model has been developed. Also, a start has been made on engine diagnostics based on on-wing CEOD to circumvent the reduced sensor problem. A hybrid Evolutionary-Algorithm Multi-Operating Point Gas Path Analysis (MOPA-EA GPA) tool has been developed for the GEnx-1B engine. This tool uses an analysis at the cruise and take-off operating point to determine the state of the components. This tool is promising but there is still room for improvement on accuracy. The current underlying GEnx-1B model does not accurately represent the cruise phase. Since the accuracy of this tool is dependent on the accuracy of the underlying GEnx-1B model, it is needed to improve the current GEnx-1B model for cruise phase.

During the cruise phase, the engine performs differently due to deviant secondary performance parameter settings. The secondary performance parameters contain information about the bleed flows, active clearance control, variable geometry and power take-off. This information is present in the CEOD and not

yet accounted for in the GEnx-1B model. Therefore, it is interesting to research the effect of the secondary performance parameters at the cruise phase to increase the accuracy of the GEnx-1B model.

1.2. Research objective & Questions

From the previous section can be concluded that the accuracy of the GEnx-1B model is to be increased, to improve the MOPA-EA GPA tool reliability. Hence, the main objective of this research is:

> *To increase the GEnx-1B model accuracy for cruise phase, making use of the additional secondary performance parameter information present in the Continuous Engine Operating Data.*

A brief literature study was performed to find key areas of interest to realize the main research objective. This resulted in the definition of the scope of this thesis. This thesis will combine a machine learning approach with theory on secondary performance parameters to determine relationships between the secondary performance parameter effects and the consequent component performance deviation. Combining these two aspects has not been done before and can provide a useful solution to decrease the GPA uncertainty if successful. In order to fulfil this research goal, the main research question and related sub-questions are introduced that will need to be answered. The main research question is:

> *Can relationships based on secondary performance parameters and determined by an evolutionary algorithm increase the accuracy of GPA models and consequently GPA accuracy?*

The proposed sub-questions are given below:

1. Which secondary performance parameters can cause deviant engine performance at different operating conditions?
2. What patterns are present in the secondary performance parameters, and what are the differences between the various operating conditions?
3. How can these differences in secondary performance parameters be compensated for?
4. Does the compensation for secondary performance parameters by using the determined relationships increase the accuracy of a GPA model?
5. Does the compensation for secondary performance parameters by using the determined relationships increase the accuracy of GPA results?

This research will be performed with the information and knowledge present at the MRO facility at KLM Engine Services. Therefore, the validation of the methodology can be performed on actual engine data from KLM GEnx-1B engines in combination with vast MRO experience.

1.3. Structure report

This report consists out of 9 chapters. Chapter 2 introduces the theoretical framework required to fully understand this thesis. Chapter 3 introduces the GSP software package, former performed work at KLM and effects on engine performance. Chapter 4 introduces the methodology to reduce the modelling error based on the secondary performance parameters. Chapter 5 introduces the GEnx-1B case description. Chapter 6 introduces the results from the method applied on the GEnx-1B engine data. In chapter 7, a gas path analysis is performed. Chapter 8 discusses the results, after which chapter 9 displays the conclusions and recommendations.

I

Background information

2

Aero engine gas turbines

Since the introduction of power-by-the-hour, engine health management has become an important part of the operation of an MRO facility [43]. This new business model introduced by Rolls-Royce meant that instead of the conventional 'material and time' based service, a fixed price for engine availability is paid to the MRO (Maintenance Repair&Overhaul) facility. This stimulated the innovation in engine health management systems. This research is performed in collaboration with KLM Engine Services. Engine health management plays an important role in contemporary maintenance practice. This chapter introduces the working of a gas turbine, the various kinds of gas turbine engine deterioration and the methods to identify them.

2.1. Gas turbine components and operation

Gas turbines make use of the Joule-Brayton cycle to generate thrust. This is done in 4 steps from the inlet of the gas turbine towards the nozzle. This section will introduce these four steps and the related components.

In Figure 2.1 a schematic representation of a gas turbine is visible. The air enters the inlet, is compressed in the compressor section. In the combustor, energy is added to the flow. In the turbine, the air is expanded to extract work from the air. This work is used to drive the compressor that is attached to the same shaft. The residual energy in the air is used to generate thrust by ejecting it into the environment from the nozzle. For the Joule-Brayton cycle, these can be set out as four thermodynamic processes:

1. Compression in the compressor.
2. Heat addition in the combustor.
3. Expansion in the turbine.
4. Heat rejection from the nozzle.

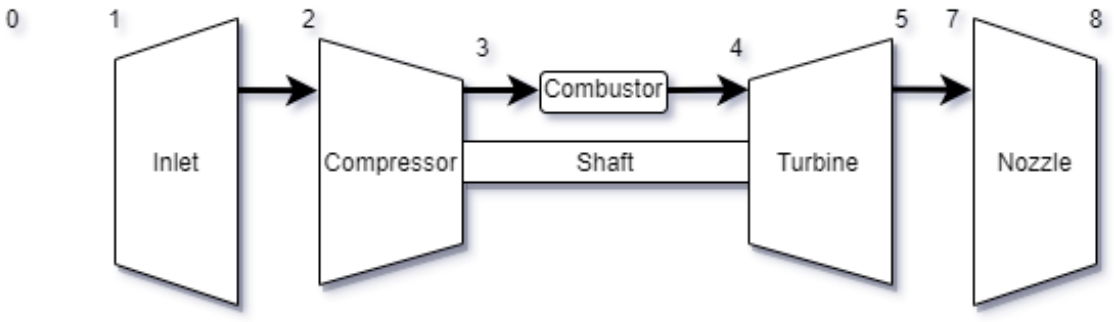

Figure 2.1: Schematic representation of a gas turbine

In order to perform engine health management, these thermodynamic processes need to be modelled. There are four ways of representing a gas turbine ranging from 0-D to 3-D modelling with increasing complexity, accuracy and computational burden [38]:

- A 0-D model is not taking the spatial domain into account and only calculates the averaged gas properties at discrete points in the engine.
- A 1-D model does take the axial flow direction into account, thereby representing the averaged gas properties throughout the engine.
- A 2-D model represents the gas properties at certain stations in the radial direction.
- A 3-D model represents the gas properties at every location throughout the whole engine.

The MRO branch mostly uses 0-D modelling due to its low computational burden and easy implementation. In order to build a 0-D model, the fundamentals of thermodynamics are used. In modelling, the distinction is made between design point modelling and off-design modelling. A design point model specifies the performance of an engine at one operating condition, ambient condition, and power setting. In this calculation, the pressure ratios, efficiencies and rotational speeds are specified. Therefore, the properties can be calculated from inlet to outlet in a single calculation. In Appendix B, the fundamentals of thermodynamics and theory on design point calculation are introduced.

Off-design modelling deals with the performance of the engine when at least one of the operating conditions, ambient conditions or power setting is changed. This analysis involves an iterative calculation scheme by which a steady-state solution is found that satisfies the conservation equations from subsection 2.2.1. Since this thesis mostly deals with off-design modelling, the following section will introduce the mathematical and thermodynamical basis for performing an off-design calculation.

2.2. Off-design calculation

The off-design performance deals with the whole operating range aside from the design point. In contrast to the design point calculation, this analysis requires an iterative approach to solve steady-state off-design solutions. This is caused by the fact that compressors and turbines show highly nonlinear behaviour over their complete operating range regarding their performance and efficiency. To solve such problems, a system of equations is put together and solved by iteration. This section will introduce the required tools to perform the off-design analysis. First, the system of equations is introduced, after which the corrected parameter groups and component maps are discussed.

2.2.1. System of equations

The off-design analysis is based on the following conservation equations:

- Conservation of mass
$$\frac{\delta}{\delta t}(\rho A) + \frac{\delta}{\delta x}(\rho A v) = 0 \tag{2.1}$$
- Conservation of momentum
$$\frac{\delta}{\delta t}(\rho A v) + \frac{\delta}{\delta x}\left(\rho A v^2\right) + A\frac{\delta p}{\delta x} = 0 \tag{2.2}$$
- Conservation of energy
$$\frac{\delta}{\delta t}(\rho A u) + \frac{\delta}{\delta x}(\rho A v h) = 0 \tag{2.3}$$

By using these principles, the components in the gas turbine can be coupled. In 0-D modelling, the outlet of a component is coupled to the inlet of the next component. If the conservation equations are satisfied, thermodynamic feasibility can be assured. By iteration, it is possible to determine a steady-state off-design solution. However, without information about the separate components in off-design conditions, this is not possible. Therefore, the following section introduces performance parameters and component maps.

2.2.2. Off-design component performance

In a gas turbine, multiple components all have their own performance over a range of operating conditions. In this section, the method to evaluate compressor and turbine performance is displayed. To describe the performance of these components at various conditions, a large set of variables is needed. These variables are visualised in Table 2.1.

Symbol	Variable	Unit
D	Characteristic linear dimension	[m]
N	Rotational speed	[rad/s]
m	mass flow	[kg/s]
p_{01}	Total inlet pressure	[Pa]
p_{02}	Total outlet pressure	[Pa]
T_{01}	Total inlet temperature	[K]
T_{02}	Total outlet temperature	[K]
γ	Ratio of specific heat	[-]
Re	Reynolds number	[-]

Table 2.1: Parameters describing performance of gas turbine components, adapted from Moorselaar [50]

Since it is undesirable to evaluate the behaviour of the components with 9 variables, the number of variables can be reduced by using the Buckingham Pi theorem. This is done in various ways resulting in dimensionless groups, quasidimensionless groups and corrected groups. These parameter groups are introduced briefly.

Parameter groups

The dimensionless parameter groups are constructed following the Buckingham Pi theorem. The relevant dimensionless parameters describing turbine and compressor performance are given in Table 2.2. Three sorts of parameter groups are available. They all have their specific use.

The dimensionless parameters are specifically useful if various working fluids need to be considered. Often, the working fluid and geometry of a single gas turbine do not change over the operating range. Therefore, quasi dimensionless parameter groups are also used.

The quasidimensionless parameter groups do not contain variables regarding the working fluid or dimensions. In this representation, the R and D and γ are taken out of the equation. The last group of parameters is the corrected type, this group is proportional to the quasidimensionless group.

As a gas turbine can operate at various conditions, corrected parameters are used. These compensate for the ambient condition and correct to the International Standard Atmosphere values (ISA). This is done by dividing the total properties through the ISA values for pressure and temperature, resulting in the corrected temperature and pressure:

$$\theta = \frac{T_2}{T_{ISA}}, \quad \delta = \frac{P_2}{P_{ISA}} \tag{2.4}$$

The values θ and δ are then used to write the corrected parameters in the form of Equation 2.5. In which values a and b are the gas turbine parameter corrections. The standard values are $a = 0.5$ and $b = 0$ and $a = -0.5$ and $b = 1$ for corrected spool speed and mass flow respectively [57]. These can however differ based on additional parameters like humidity [57]. These corrections are established based on experimental data.

$$X_c \approx \frac{X}{\theta^a \delta^b} \tag{2.5}$$

By plotting these parameter groups against each other, the performance of the main gas turbine components can be represented by graphs. These graphs are called component maps and are treated in the following section.

2.2.3. Component maps

As mentioned, the corrected parameter groups can be used to compare and evaluate the compressor and turbine over their operating range. This is done by using component maps. In this section, the correlations between the parameter groups in these component maps are explained. Furthermore, the use in off-design

	Dimensionless parameter group	Quasidimensionless parameter group	Corrected parameter group
Mass flow	$\frac{\dot{m}\sqrt{RT_{0in}}}{D^2 p_{0in}\sqrt{\gamma}}$	$\frac{\dot{m}\sqrt{T_{0in}}}{p_{0in}}$	$\frac{\dot{m}\sqrt{\theta}}{\delta}$
Pressure ratio	$\frac{p_{0\text{out}}}{p_{0\text{in}}}$	$\frac{p_{0\text{out}}}{p_{0\text{in}}}$	$\frac{p_{0\text{out}}}{p_{0\text{in}}}$
Spool speed	$\frac{ND}{\sqrt{RT_{0in}}}$	$\frac{N}{\sqrt{T_{0in}}}$	$\frac{N}{\sqrt{\theta}}$
Isentropic efficiency	η	η	η

Table 2.2: Dimensionless parameter groups

modelling is discussed.

Compressor
The function of a compressor is to increase the pressure of the working fluid. To do so, the compressor can compress a certain corrected mass flow at a certain rotational speed. This happens with an associated efficiency. The compressor map defines the relationships between the pressure ratio, corrected mass flow, efficiency and corrected rotational speed of one compressor geometry. The compressor maps consist of curves that indicate pressure ratio over a corrected mass flow range at a certain corrected spool speed. Additionally, the constant efficiency contour lines are plotted in the graph, or a separate graph is given to display the efficiency versus the mass flow. An example of these maps is given in Figure 2.2.

These maps contain important information about the performance of one specific compressor. The typical characteristics of a compressor map are described below:

- The operating line is indicated. This line is dependent on the compressor and turbine power matching. If properly done, the line directly relates to the optima of the corrected spool speed lines in the upper graph in Figure 2.2.
- Constant corrected spool speed lines are indicated by the black lines in Figure 2.2.
- The surge line represents the maximum obtainable pressure ratio for a corrected spool speed, without surge occurring. Surge can follow from the stall behaviour of the compressor blades in case of a low corrected mass flow at which the compressor can not withstand the adverse pressure. The stall can lead to reverse flow which can cause large oscillations in the compressor mass flow and therefore throughout the whole gas turbine. This is called surge and can be disastrous for the gas turbine. The line at which this phenomenon can occur is displayed in Figure 2.2.
- The choking area of the compressor map indicates the part of the compressor map where the maximum mass flow is obtained. This behaviour is visible in Figure 2.2, denoted as choking. No increase in mass flow is possible if the back pressure is lowered due to choked conditions.

Turbine Map
In line with the compressor maps, turbine maps also display the relation between the parameter groups. However, for the turbine maps, the efficiency and corrected mass flow are plotted against the pressure ratio. The turbine maps displayed in Figure 2.3 also contain certain characteristics. These are given below:

- The constant corrected spool speeds are displayed as black lines. At a certain corrected mass flow, the curves flatten out. This is caused by the choking mechanism of the turbine. If the back pressure is further reduced, this will not lead to an increase in mass flow.
- The isentropic efficiency is constant over a large range of corrected spool speeds and pressure ratios. This is caused by the accelerating behaviour of the flow through the turbine, enabling it to operate over a broad range of incidence angles without a large efficiency loss.
- The gas turbine will mostly operate with a choked turbine since the design point is located in the choked region.

Using the component maps, the off-design performance calculation can be performed. This is done by iterating until the parameter groups of individual components match each other. The following section describes the calculation strategy.

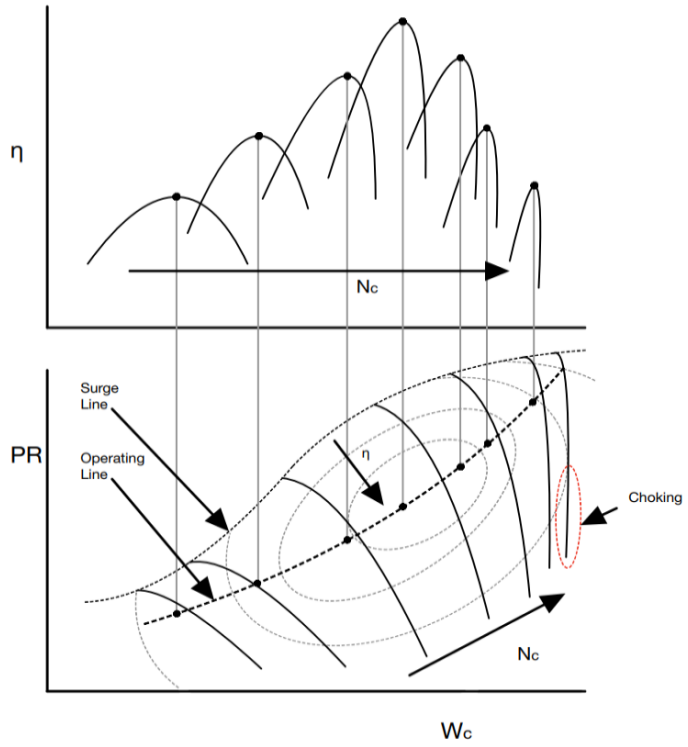

Figure 2.2: Typical compressor map

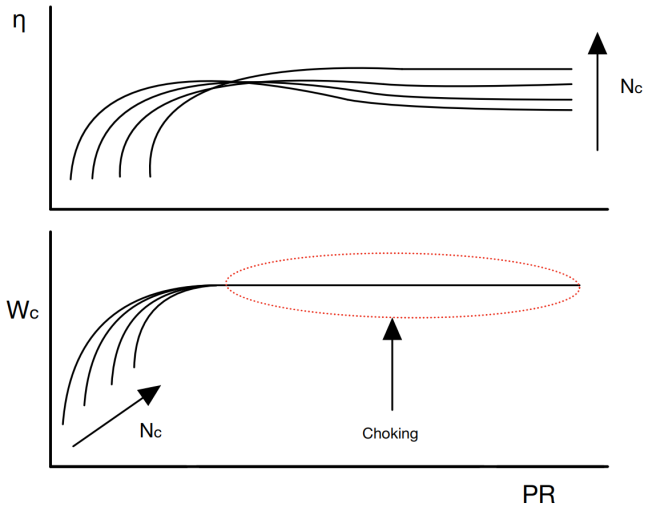

Figure 2.3: Typical turbine map

2.2.4. Off-design calculation scheme

Using the conservation equations, and the component maps, the complete cycle calculation can be performed. For this, the individual components are linked by conservation equations to assure the feasibility of the off-design solution. Using these conservation equations, an iterative scheme is executed to minimise the error between the values of thermodynamic states between components. This requires computational power since computation by hand is too time-consuming. In chapter 3 a software package is introduced that is able to perform off-design calculations.

2.3. Deterioration modes

Like every piece of machinery, gas turbines are prone to wear and tear during their lifespan. The wear and tear of the compressors and turbines can lead to drastic changes in thermodynamic performance. The degradation of a single component influences the behaviour of the complete engine since the individual components are coupled thermodynamically or/and mechanically. This section introduces the deterioration effects that can influence the performance of the gas turbine. The existing deterioration effects are [20]:

- Fouling
- Corrosion
- Erosion
- Abrasion
- Foreign object damage

These forms of deterioration can be divided into two categories. The first category is recoverable degradation, this includes any damage that can be restored by on or off-line maintenance. The second group is non-recoverable damage. This can only be restored by the replacement of parts or an overhaul. The aforementioned deterioration effects are further elaborated upon below. Also, the distinction is made between recoverable and non-recoverable degradation.

2.3.1. Fouling

Fouling is caused by the build-up of material on the compressor, turbine blades, combustor and annulus area. The material originates from smoke, oil mists, carbon and sea salt and is mostly smaller than 2-10 μm [23]. Due to this phenomenon, the surface roughness and (to a certain extend) the shape of the compressor and turbine blades are affected. This can negatively impact the performance of the compressor and turbine [21]. This sort of deterioration can partly be remedied by using water washes. This can be done on-line and is, therefore, recoverable degradation.

2.3.2. Corrosion

The metal surface of the blades in the turbine and compressor are susceptible to corrosion. Corrosion is caused by the chemical reaction between the blades and contamination of the working fluid and fuel [22]. A common form of corrosion is oxidation. By the loss of electrons, the metal blades get positively loaded. This can lead to the formation of a surface metal oxide. Due to the high temperatures, this form of corrosion is mainly observed in the combustor and turbines. Another type of corrosion is hot corrosion. In addition to oxygen, hot corrosion needs the presence of another chemical substance. Due to the presence of contamination in the working fluid and fuel, which can work as a catalyst, oxidation rates can increase. The formation of metal oxide leads to cracks in the turbine blades and can result in performance deterioration. This kind of deterioration effects is non-recoverable. To prevent corrosion, coatings are applied to the blades.

2.3.3. Erosion

Erosion is the damage done to the blades by the impact of particles often larger than 10 μm [22]. This phenomenon can change the profile of the blades and therefore influences the thermodynamic performance of the gas turbine. This kind of deterioration is non-recoverable.

2.3.4. Abrasion
A gas turbine has a certain clearance between the rotor blades and the stator casing. During an overhaul and at the service entry of an engine, the stator casing is coated with an abradable seal. These seals are used to decrease the clearance between the stator casing and the rotor blades, and thereby increase the efficiency [14]. Abrasion in gas turbines is the rubbing behaviour of the rotor on the stator casing seals. During operation, these seals wear out and the clearance between stator casing and rotor increases, decreasing the efficiency. This is non-recoverable deterioration.

2.3.5. Foreign object damage
The last category of deterioration is Foreign Object Damage (FOD). This is damage done by objects sucked into the engine or by pieces broken off the engine components themselves. Also, the accumulation of ice in the inlet can cause damage when sucked into the engine [22]. This is also non-recoverable deterioration.

2.4. Deterioration effect on components
As mentioned, the introduced deterioration modes affect gas turbine performance. How these kinds of deterioration impact the performance of the gas turbine will be explained in this section.

2.4.1. Compressor deterioration
A compressor performance decrease is caused by all the deterioration modes mentioned in section 2.3. The changes in the geometry of the compressor blades lead to reduced efficiency, reduced capability of generating head, and reduced compressor flow capacity [24]. Also, the surge margin can be decreased [44]. These changes can be displayed in the compressor map. This is visible in Figure 2.4. In this figure, the flow capacity is decreased as well as the efficiency. By translation of the constant speed lines along the W_c and η axis, it is possible to change the characteristics of the component to represent the deteriorated component. The amount by which the lines are translated represents the deterioration level. This opens up the opportunity to simulate the effect of component deterioration on gas turbine performance. By using two parameter groups from efficiency, pressure ratio and corrected mass flow the component map can be adapted. The adaption of the third parameter group follows from the adaption of the selected two parameter groups.

2.4.2. Turbine deterioration
The turbine map can be adapted following the same analogy as the compressor map. The turbine can display the same behaviour as the compressor due to the deterioration effects. The thicker boundary layers on the turbine blades reduce the mass flow rate for the same pressure ratio. Also, the efficiency will decrease [6]. This is displayed in Figure 2.5 as the set of red lines. However, the turbine can also have an increased flow capacity through material removal near the nozzle area. The flow capacity is limited by the throat area. If the throat area is increased due to material removal, a higher flow capacity is reached. This is indicated by the set of blue lines. This is however also accompanied by a reduced efficiency as it leads to reduced work extraction [24].

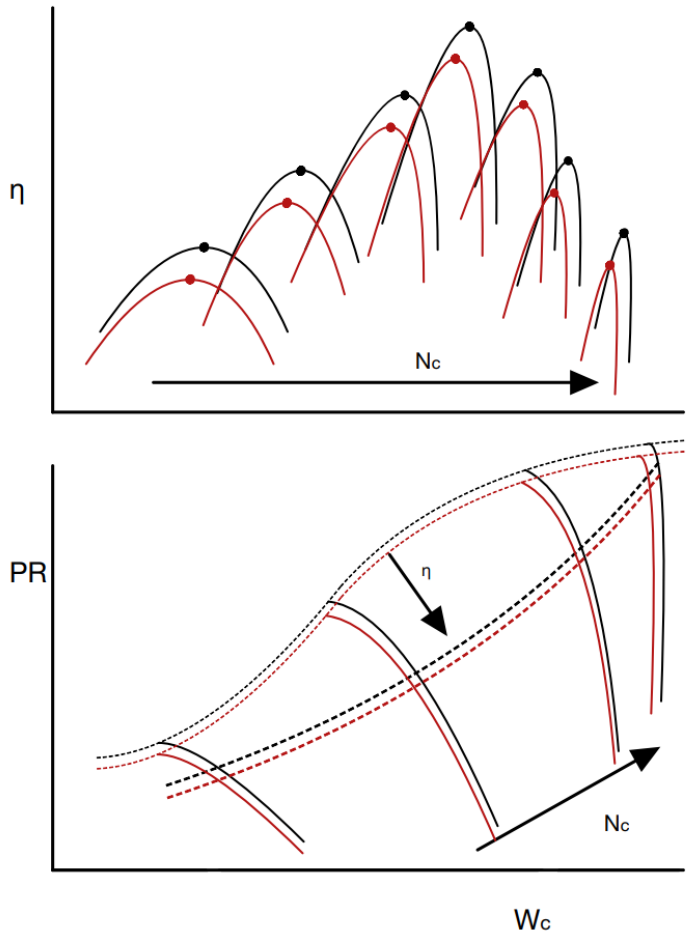

Figure 2.4: Component map of a deteriorated compressor adapted from [12]

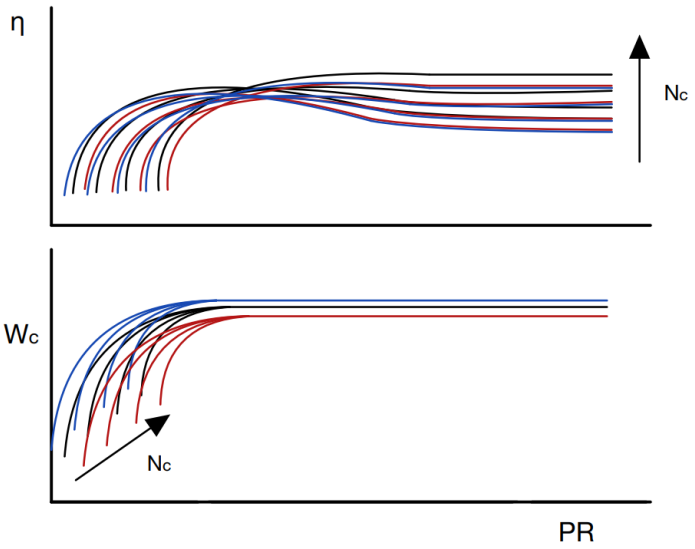

Figure 2.5: Component map of a deteriorated turbine adapted from [12]

All forms of deterioration have their signature effect on gas turbine components. These effects are displayed in Table 2.3 [6]. The next section will introduce methods to estimate these deterioration grades by means of gas path analysis (GPA).

Physical fault	W_c change A	η change B	Ratio A:B
Compressor fouling	⇓	⇓	3-8:1
Turbine nozzle guide vanes fouling	⇓	⇓	2:1
Compressor erosion	⇓	⇓	2:1
Turbine erosion	⇑	⇓	2:1
Compressor corrosion	⇓	⇓	2:1
Turbine corrosion	⇑	⇓	2:1
Foreign object damage(non severe)	⇕	⇓	0.5:1
Abrasion	⇑	⇓	0.5:1

Table 2.3: Effect of deterioration on gas turbine performance adapted from [6]

2.5. Gas path analysis

As explained, gas turbine engines suffer from degradation during service. These physical deterioration phenomena manifest themselves in a change in thermodynamic performance. In turn, the performance change, causes a deviation in pressures, temperatures, fuel flow and rotational speed. Using this analogy, component deterioration can be identified by using the engine sensor data to identify component faults. This is called gas path analysis. Urban [48] was the first to describe these relations. His analogy is visible in Figure 2.6. By assuming a linear relationship between the difference in measurements and the performance parameters of the engine, he was able to estimate the performance of the individual components in the gas turbine. Ever since Urban started the pioneering work on gas path analysis, the industry expanded on finding multiple ways to relate the measured variables (independent parameters) to the performance parameters (dependent parameters). These can be divided into two groups. Both model-based techniques, as well as empirical methods are available.

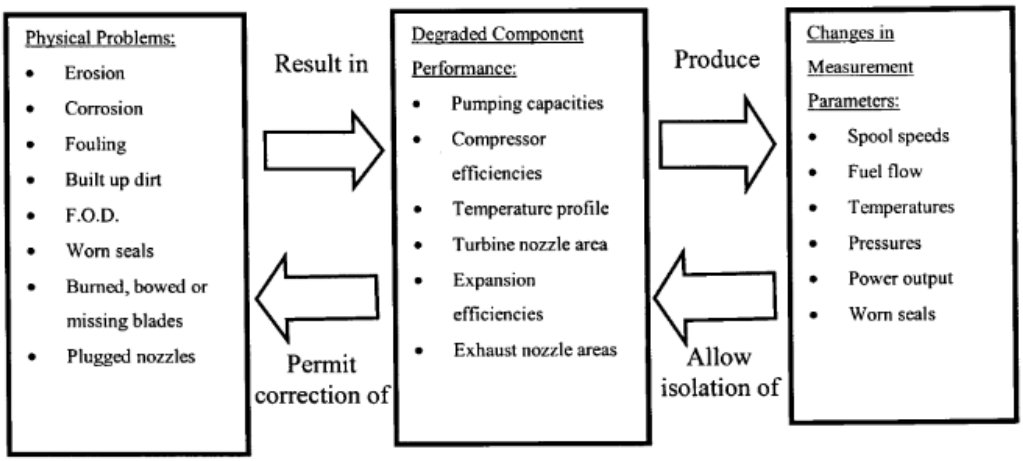

Figure 2.6: Gas path analysis analogy from Urban [48]

2.5.1. Model-based techniques

The model-based techniques require a model of the gas turbine that has to be analysed. With the engine model and measurement data, an estimation can be made about the deterioration state of the components. Possible ways of implementing such a method are discussed below.

Linear GPA

A gas turbine modelling approach has to deal with the highly non-linear relationship between the independent(pressure, temperature, thrust and mass flow rate) and dependent (pressure ratio, flow capacity and efficiency) parameters of the engine. Linear GPA assumes the relationship between these components to be linear, around a certain operating point. This linear relation is given in Equation 2.6 [62]. In which $\bar{z}$ consists of measured parameters and $\bar{x}$ of the performance parameters. H represents the influence-coefficient matrix (ICM). The inverse of H is called the Fault-Correction Matrix (FCM). With the FCM the deviation of the engine component parameters can be calculated. This is a fast and easy method to implement and is able to detect multiple faults but is only valid close to the model reference point, as the linear relation will not hold any more at a different power setting [6]. Also, the number of measured parameters is equal to the number of estimated performance parameters. Modern gas turbines have a reduced number of measurements so this decreases the applicability of this method [6].

$$\bar{z} = H \cdot \bar{x} \tag{2.6}$$

$$\Delta\bar{z} = H \cdot \Delta\bar{x} \tag{2.7}$$

$$\Delta\bar{x} = H^{-1} \cdot \Delta\bar{z} \tag{2.8}$$

Non-linear GPA
Non-linear GPA takes the highly non-linear behaviour of a gas turbine into account. This method implements a Newton-Raphson calculation scheme which iteratively calculates the ICM by using Equation 2.8. From which the FCM is calculated. These results are used to construct the new ICM until convergence is reached. By repeating this process a feasible operating point can be found. This method is implemented by Escher in Pythia [6].

Adaptive Modelling (AM), first introduced by Lambiris et al. [30], applies this method in combination with adaptation of the actual engine model by altering the component maps during the analysis. This component map adaptation is done by applying the analogy from section 2.4. The extent to which the component maps are adapted, represents the component deterioration. This is done to provide a better fit to the measured parameters to achieve more accurate results [54].

Both these methods provide a fast way to perform GPA. However, both these methods require as many measurements as component states that are estimated [6, 54]. Contemporary gas turbine engines have a reduced number of sensors in the gas path. Therefore, these methods are getting less applicable for modern gas turbines.

Genetic algorithm
To overcome this issue, another approach can be used. The non-linear model-based GPA with a genetic algorithm applies machine learning instead of an iterative calculation scheme to produce a feasible set of engine component deterioration states. A genetic algorithm searches for a solution based on evolution theory and natural selection [19]. For GPA purposes, the genetic algorithm produces a set of solutions with engine component states, called a population. Subsequently, the non-linear engine model is run with the estimated component states from the population. The output results are compared to the engine measurement data and the 'fitness value' of the individual solutions is determined. By 'mutation' and 'crossover' within the current population, a new population is generated mostly from the 'fitter' solutions. By applying randomisation, local minima are prevented. Since it does not apply deterministic solving, it is capable of dealing with noise and having fewer measurements available than component states required [11]. The downside of using a genetic algorithm is that they require long computation times.

Empirical techniques
Besides model-based methods, empirical methods also exist. These methods do not consider the thermodynamic behaviour of the gas turbine so no physics model is required. Instead of physics, they are based on a vast amount of data relating known engine deterioration to measurement deviations. Often used methods are neural networks, Bayesian belief networks and Expert systems [32]. Their main advantage is that they do not require a model of the engine. However, to train these empirical models, a large database of gas turbine incident data is required. This is often not available in the MRO environment.

2.5.2. Optimal GPA solution at KLM
In the brief summary of available GPA methods, the main advantages and drawbacks of the different methods are explained. The requirements for a GPA analysis tool for on-wing GPA at KLM are given below:

- Able to deal with more component state parameters than measurements available.
- Able to deal with measurement noise.
- Fast for large scale implementation.
- Able to perform accurate GPA for every power setting.

The purely empirical methods have the advantage that they are able to deal with measurement noise and sensor bias but they require a large dataset of training data with known deterioration states. Since this data is not available, these have not been implemented at KLM. The two options that are most viable for application at KLM are the non-linear adaptive modelling and the non-linear model-based GPA combined with a genetic algorithm. A comparison of their advantages and drawbacks is made:

Non-linear adaptive modelling

Advantages

- More capable of performing fast analysis.

Drawbacks

- Not able to deal with measurement noise and sensor bias.
- Not able to estimate more component states than measurements available.

Non-linear model-based GPA with genetic-algorithm

Advantages

- Able to estimate more component states than measurements available.
- Able to deal with measurement noise and sensor bias.

Drawbacks

- Higher computational burden.

Both methods have been studied at KLM and are further explained in chapter 3.

3

Engine performance modelling for diagnostics and prognostics

For an MRO business as KLM, it is of great value to estimate the aforementioned deterioration states of the engines cost-effectively. Instead of a visual inspection or an overhaul, gas path analysis uses the measurement data of the gas turbine to estimate the individual component performance. This chapter explains the GPA software and methods that are used within KLM ES, after which the former performed research at KLM is introduced. Subsequently, various effects on engine performance are treated.

3.1. GSP

At KLM, the Gas Turbine Simulation Program (GSP) is used to perform gas path analysis. GSP [54] is a non-linear gas path analysis tool developed at the National Aerospace Laboratory (NLR) in collaboration with the TU Delft. It is a 0-D non-linear object-oriented gas path simulation tool that is easy to implement because of its flexibility and 'drag-and-drop interface' [54]. The inlet, fan, compressors, combustion chamber, turbines and exhaust are modelled as objects which can be dragged into the graphical user interface to construct an engine model. A visual representation of an engine model in GSP is displayed in Figure 3.1. Due to its 0-D form, GSP calculates the flow properties at the inlet and outlet of the different components [54]. GSP is capable of performing steady-state calculations as well as off-design and transient calculations.

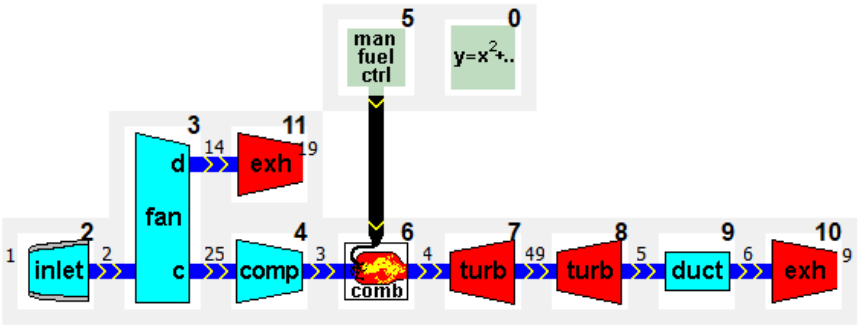

Figure 3.1: Representation of the GEnx-1B engine in GSP

3.1.1. Component models

Most of the components used in GSP are built in the 0-D modelling domain, meaning that they do not calculate the gas properties along the longitudinal axis in the component itself. Only at discrete points in the gas turbine, the gas properties are known. Several components are implemented in the 1-D domain,

namely the multi-reactor combustor and the recuperator are modelled this way [54]. The behaviour of the component is divided into two modelling situations. The on-design and the off-design modelling.

The on-design modelling performance is specified by clicking the component and specifying its characteristics as pressure ratio and isentropic efficiency and areas. Hereby, the design point performance can be determined for every component and altered to fit any gas turbine from industry.

The off-design performance of the components is captured by the component maps. These component maps are introduced in subsection 2.2.3. The location in the component map at which the gas turbine is operating is determined by any two out of the three corrected parameters W_c, PR, N_c. These component maps are specified in MTU map format with beta lines to assure better iteration stability [26]. This also allows for easy altering of the maps by using SmoothT and SmoothC [26]. The simpler components as ducts and exhausts, are modelled with simple relations.

3.1.2. Conservation equations

To link the individual components in GSP, conservation equations are used. The first conservation equation is the conservation of mass mentioned in section B.2. GSP uses this equation to construct Equation 3.1 [54], in which M_v is the mass inside the component, and W_{in} and W_{out} are the mass flow in and out of the component respectively, to describe the mass flow through a component.

$$\frac{dM_v}{dt} = W_{in} - W_{out} \tag{3.1}$$

The relation between the gas properties is given by Equation 3.2, in which V_{comp} is the component internal volume.

$$\frac{dM_v}{dt} = \frac{V_{comp}}{\gamma RT} \cdot \frac{dp}{dt} \tag{3.2}$$

The conservation of energy is given in Equation 3.3. And in the form of the conservation equation for the N_1 and N_2 shafts, Equation 3.4 is used with I as inertial momentum of the spool and P_{abs} and P_{del} power absorbed and delivered.

$$\frac{dM_v}{dt} \cdot u + M_v \cdot \frac{du}{dt} - Q = w_{in} \cdot h_{in} - w_{out} \cdot h_{out} + P_{abs} \tag{3.3}$$

$$\mathrm{I} \cdot \frac{d\omega}{dt} \cdot \omega = P_{abs} + P_{del} \tag{3.4}$$

The last equation is the conservation of momentum given in Equation 3.5.

$$\sum \left(w_{in} \cdot c_{in} + A_{in} \cdot p_{sin} \right) + F_x = w_{out} \cdot c_{out} + A_{out} \cdot P_{out} \tag{3.5}$$

3.1.3. Numerical operation

To describe the operating point of a gas turbine, GSP uses a state vector $\bar{S}$. The state vector contains state variables that describe the operating point of single components. Because the components are linked by the conservation equations or by physical connections, some components share the same state variables. Hence, it is possible to set up a vector containing error variables describing the error between the operating point of the components. This error vector is given in Equation 3.6 in case of convergence. An example of such an error equation is given in Equation 3.7, in which the mass flow through the LPC and HPC is linked by the conservation of mass. The component operating points are described by the spool speed and pressure ratio, which can be used to determine the mass flow by the use of component maps. In GSP the state variables and errors are normalised by dividing them with their design point value for numerical stability [54].

$$\bar{E}(\bar{S}) = \overline{0} \tag{3.6}$$

$$E_1 = \dot{m}_{LPC} f(N_1, \beta) - \dot{m}_{HPC} f(N_2, \beta) \tag{3.7}$$

To reach the solution state vector, the Newton-Raphson numerical method is applied. By linearising Equation 3.6 around the design point, Equation 3.8 is set up in which J is the jacobian representing the partial derivatives of the errors over the state variables [54]. This jacobian can be used in combination with the Newton-Raphson numerical method to approach a solution. The next iteration state vector is given in Equation 3.10, in which $\Delta\bar{S}_i$ is given in Equation 3.11 with the inverse of the jacobian.

$$\Delta \bar{E} = J \cdot \Delta \bar{S} \tag{3.8}$$

$$J_{i,j} = \frac{\Delta e_i}{\Delta s_j} \quad (i, j = 1 \ldots n) \tag{3.9}$$

$$\bar{S}_{i+1} = \bar{S}_i + \Delta \bar{S}_i \tag{3.10}$$

$$\Delta \bar{S}_i = \mathbf{J}^{-1} \cdot \Delta \bar{E}_i \tag{3.11}$$

To control the convergence rate and stability, this equation is expanded with f, this factor is partially automatic and input controlled [54]. This results in Equation 3.12. If an error vector is reached that contains values inside a certain predefined error tolerance band, GSP assumes convergence.

$$\bar{S}_{i+1} = \bar{S}_i + f \cdot \Delta \bar{S}_i \tag{3.12}$$

Now the basics of GSP are set out, the two implementations used at KLM are introduced. First, adaptive modelling is explained after which the MOPA-EA GPA method is treated.

3.1.4. Adaptive modelling

In multiple studies, adaptive modelling (AM) is implemented to estimate gas turbine component deterioration states [50, 52, 55]. Adaptive modelling has the ability to adapt a model inside of the numerical iteration scheme to measured data. The adaption to models is done by altering the component maps by means of map modifiers. After the numerical iteration scheme has converged, the adapted component performance is compared to the original component performance to indicate deterioration level. GSP implements AM by adding an additional internal set of equations to the gas turbine model. These equations assure that the model matches with the measurement data by adapting the additional set of condition parameters called the map modifiers. This implementation is visible in Equation 3.13 [54], which is an extension of Equation 3.8. The matrix consists of the following equations translated to words by Pieters[35]:

- Basic model error equations on the top left side with the unknown state variables s_n.
- Effect of changed component maps on the calculated engine equilibrium on the top right side with the unknown variables s_{cm} as map modifiers.
- Effect of state variables on additional error equations in the bottom left side with the unknown state variables s_n.
- Effect of changed component variables on the additional error equations on the bottom right side with the unknown variables s_{cm} as map modifiers.

For the matrix to be invertible, it has to be a square. The calculation is converged as both sets of error equations are less than the users set requirement [54]. The convergence speed of such a matrix scheme is high due to the internal nature of the calculation. After convergence, the map modifiers indicate the deterioration of the components.

$$\begin{array}{ccc|ccc|cc} f_1(s_1)+ & \cdots & f_1(s_n)+ & f_1(s_{c1})+ & \cdots & f_1(s_{cm}) & = & \varepsilon \\ \vdots & & \vdots & \vdots & & \vdots & & \\ f_n(s_1)+ & \cdots & f_n(s_n)+ & f_n(s_{c1})+ & \cdots & f_n(s_{cm}) & = & \varepsilon \\ \hline f_{m1}(s_1)+ & \cdots & f_{m1}(s_n)+ & f_{m1}(s_{c1})+ & \cdots & f_{m1}(s_{cm}) & = & \varepsilon_{m1} \\ \vdots & & \vdots & \vdots & & \vdots & & \\ f_{mm}(s_1)+ & \cdots & f_{mm}(s_n)+ & f_{mm}(s_{c1})+ & \cdots & f_{mm}(s_{cm}) & = & \varepsilon_{mm} \end{array} \tag{3.13}$$

The adaptive modelling method is a fast method to determine the deterioration, but its applicability on noisy data can lead to inaccuracies. Due to its deterministic nature, the output of every evaluation is determined by the measurement data. If this data contains noise, the Newton-Raphson method can iterate to a non-valid solution to fit the data. Besides, AM can only determine as many component states as measurement points available [54]. With modern gas turbines, this can limit the applicability because of the decreasing number of gas path sensors installed.

3.1.5. Calibration factors

In GSP, a model of an engine is created to match a certain engine type. This model is called the baseline model. The component deviation calculated between the baseline model and the engine under investigation at the same ambient conditions and power settings is purely caused by component deterioration, measurement noise and bias, engine to engine variation and modelling error. These errors can corrupt the component deterioration evaluation. To reduce these errors, AM implements calibration factors [55]. These calibration factors match the design point of the baseline model to the operating point of the engine under investigation. A calibration factor is visible in Equation 3.14. The P is a performance parameter and the subscripts $meas$ and $model$ indicate the measured and the model parameter set.

$$f_c = \frac{P_{i\,\text{meas}}}{P_{\text{i model}}} \tag{3.14}$$

Such calibration step is visualised in Figure 3.2. The model calibration step is performed by running the reference model at its design point and dividing all the measured performance parameters by the model performance parameters. These calibration factors are then used to scale all the performance parameters before executing the actual AM calculation. This can be problematic when the measured dataset is not taken at the same power setting. This is visualised in Figure 3.2. The left image represents a calibration step at equal power settings. The right represents a calibration at an unequal power setting. This leads to the calibration factor trying to compensate for the different power setting. This is essentially off-design GPA and can lead to inaccurate deterioration results [52].

Also, the calibration factor is calculated with a certain setting of secondary performance parameters, which will be introduced in section 3.3. These secondary performance parameters influence the gas turbine behaviour and if not taken into account, it can affect the GPA results [25].

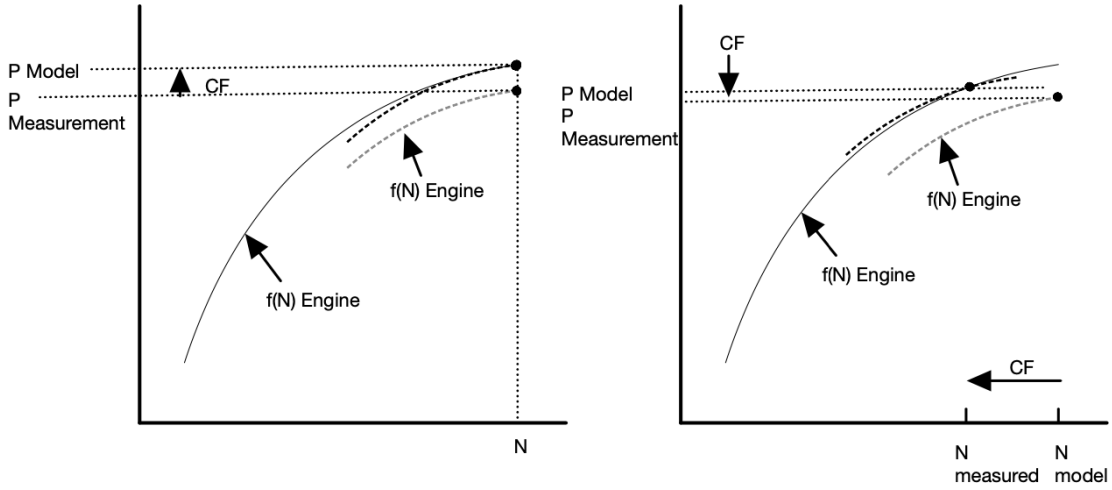

Figure 3.2: Working principle of calibration factor adapted from [52]

3.1.6. MOPA-EA GPA

As mentioned in subsection 3.1.4, adaptive modelling can only determine as many component states as measurements available. Since modern gas turbines have a reduced number of gas path sensors, the applicability of AM is limited. An alternative also used at KLM ES is the genetic algorithm in combination with the multi-operating point analysis. First, the principle of the genetic algorithm is introduced after which the multi-operating point analysis is explained.

Genetic algorithm

The genetic algorithm is a heuristic optimisation algorithm. The genetic algorithm applies the principle of natural selection and 'survival of the fittest' to come to a certain optimised solution. In nature, survival of the fittest is driven by the individual competition between animals. The fittest animals have the largest chance

of survival [16]. Consequently, the population of fit animals is able to produces more offspring, and the least fit produce less offspring. The next population mostly possesses characteristics from the fittest individuals from the last population. The genetic characteristics of the next population are determined by mutation and crossover between the individuals from the last population.
This process is mimicked by the genetic algorithm. For an optimisation problem, an objective function can be defined. An example of an objective function is given in Equation 3.15, with x,y,z as variables. These variables can all be modelled as scaled binary strings to form an individual from a population. Such representation is given in Equation 3.16. At initialisation, a population is created from multiple of these individuals. The object function is evaluated for the whole population and the next generation is created, based on the *fitness* of the individuals in the population.

This is done by *crossover* and *mutation*. Crossover is combining the binary strings of two individuals to produce one offspring individual. The individuals from which this next generation is created are based on their *fitness*. This makes optimisation possible. Mutation is the principle of randomly changing the binary values in the matrix as given in Equation 3.16. This randomisation ensures that the algorithm does not get stuck in local minima. This process is iterated until an acceptable value of the objective function is reached.

$$obj = f(x, y, z) \tag{3.15}$$

$$Individual = \begin{bmatrix} 1 & 1 & 0 \\ 0 & 1 & 0 \\ 1 & 0 & 0 \\ 0 & 0 & 1 \\ 0 & 0 & 1 \\ 1 & 1 & 1 \\ 1 & 0 & 1 \\ 1 & 1 & 0 \\ 1 & 0 & 1 \\ 0 & 1 & 1 \end{bmatrix} \tag{3.16}$$

From this principle, many variants emerged that use the same principle. One of these variants is the differential evolution (DE) algorithm introduced by Storn and Rainer [46]. Instead of a binary string, the variables are coded as floating values. The principles behind DE are similar to the approach used in the genetic algorithm. This algorithm is applied by Grönstedt [11] in gas path analysis to determine the component deterioration states by running the engine model with populations filled with deterioration states and comparing measurement values to model outputs. His approach will be further introduced in the following section.

MOPA

In order to perform gas path analysis, Grönstedt [11] combined the DE with multi-operating point (MOPA) gas path analysis. MOPA uses multiple operating points to evaluate the components degradation for which the assumption is made that the deterioration states of the components are independent of the operating point. This was first introduced by Stamatis et al. [45]. He identified the possibility of using multiple operating points to decrease the component analysis uncertainty. The choice of these operating points is also important for the results, Sampath et al. suggest that the reliability increases when the two operating points are further apart [39].

Grönstedt [11], implemented this strategy in combination with the relation proposed by Zedda et al, Equation 3.17 [64]. This equation is used to relate the measurement set z to the non-linear relation h dependent on x, the deterioration states of the components and w the ambient and operating conditions. v represents the measurement noise. The resulting, to be minimised, object function is visible in Equation 3.18 [11].

$$z = h(x, w) + v \tag{3.17}$$

$$f(x) = \sqrt{\frac{\sum_{i=1}^{n}\sum_{j=1}^{m}\left(\frac{z_{i,j}-h_i(x,w_j)}{z_{i,s}\sigma_i}\right)^2}{m \cdot n}} \tag{3.18}$$

Equation 3.18 is used to minimise the difference between the measured values z and the outputs of the model h at operating points n within a dataset of m measurements. σ is used to deal with the noise of the measurements by increasing or decreasing their influence accordingly.

By using the former mentioned DE, accurate values for component conditions can be found by on-wing analysis. This is performed by Rootliep [37] at KLM. The following section introduces further research performed at KLM regarding gas path analysis.

3.2. Former performed relevant research at KLM

Within KLM, multiple studies have been performed regarding gas path analysis. In this section, the relevant studies are set out. These studies involve on-wing analysis, off-design analysis and the modelling of the GEnx-1B.

3.2.1. On-wing analysis

In order to reduce the costs of maintenance, on-wing condition monitoring has become more interesting for the MRO business. Verbist, Moorselaar and Rootliep [37, 50, 52] have performed on-wing gas path analysis. These studies will be introduced in this section.

Gas path analysis for enhanced aero-engine condition monitoring and maintenance

Verbist [52] researched the capabilities of gas path analysis to be more effectively used in the maintenance process of gas turbines within KLM. His dissertation covered the topics of improving the accuracy and reliability of on-wing gas path analysis, measurement uncertainty and the steps required for creating a GPA framework to involve in an MRO business. Verbist study was applied on the CF6-80C2 by means of AM.

He concluded that the accuracy and reliability of on-wing GPA are influenced by a couple of factors:

- Measurement error: The measurement error in on-wing data is determined by the accuracy of the sensors. Verbist performed a Monte Carlo simulation to display the effect of the measurement uncertainty. He concluded that measurement noise leads to a component deterioration state deviation of maximum ±0.5%, with the highest standard deviation on the LPC component. This is based on the accuracy of the CF6-80C2 sensor package [52]. The fact that AM is deterministic aggravates the influence of noise on the GPA results.

- Missing sensors: As mentioned, missing sensors increase the GPA uncertainty of the corresponding component. The main difference between the test cell data and on-wing GPA is the missing thrust sensor. The thrust sensor can be compensated for by using the $P_{s,14}$, the fan discharge, as an alternative for the thrust. This proved to be an accurate replacement. This sensor is however not present on the GEnx-1B engine.

- Modelling error: Another contributor to inaccurate GPA is the modelling error. These modelling errors stem from a difference in characteristics between the engine on which the model is calibrated and tuned and the engine that is to be analysed. As mentioned in subsection 3.1.5, this error can be decreased by using calibration factors. Verbist introduced off-design calibration, which uses the calibration method from subsection 3.1.5 for every power setting individually. A type of modelling error that can not be compensated for by calibration factors are the bleed flows. In the CF6-80C2, bleed air is retracted from the core. Verbist concluded that not incorporating the bleed flows drastically reduces the reliability of the GPA results. Also, the power off-take that is present on-wing can cause some inconsistencies between the model and the on-wing situation. These are assumed to be negligible because the power extraction is limited compared to the total power of the N2 shaft(0.4% of the HPT power delivery) [52].

- Incorrect component maps: The last source of error can be related to the component maps. The off-design performance of the model is characterised by the components maps. If off-design gas path analysis is performed, the errors in the component maps can propagate into the deterioration results. Verbist used speed line relabeling in combination with AM to tune the component maps. This strategy is built on the assumption that deterioration values are independent of the corrected spool speeds [53]. In order to determine speedline values that result in the lower deviations, an iterative process was performed to decrease the root mean square deviation of the estimated component deterioration

states. The formerly mentioned modelling error effects also affect the on-wing component map tuning due to additional uncertainty.

Verbist also suggested a solution to incorporate GPA into the MRO strategy. By creating a framework with engine number specific information on calibration factors, engine performance data, maintenance and workscope data, and GPA data. Verbist created a framework that displayed promising results for the CF6-80C2 maintenance.

Since this thesis contains a case study regarding the GEnx-1B engine, the following studies from Moorselaar and Rootliep [37, 50] are also introduced. Moorselaar developed the GEnx-1B model and performed GPA with the AM tool. Rootliep performed GPA with the same GEnx-1B model by applying the MOPA-EA GPA tool.

Gas Path Analysis on the GEnx-1B at KLM Engine Services
Moorselaar [50] created a model of the GEnx-1B engine in order to perform gas path analysis. The GEnx-1B engine is a state of the art engine. With regards to gas path analysis, the engine is different from the former generation of engines because it is equipped with a lower number of sensors. The GEnx-1B lacks a pressure measurement behind the fan, booster, and high-pressure turbine. This introduced additional uncertainty into the modelling of the engine. For the design point additional assumptions were made to make the engine model comply with the measurement data. Also, the component map tuning procedure is affected by the missing measurements, adding more uncertainty. Moorselaar successfully created an accurate design point model fitting the measured parameters from the KLM test cell. Furthermore, he tuned the component maps between take-off and max continuous with acceptable accuracy.

Besides model creation, the missing gas path sensors are limiting the accuracy and applicability of the AM simulation. As mentioned in subsection 3.1.4, the AM GPA tool is only able to estimate an equal number of deterioration modes as the available number of sensor measurements. He concluded that the AM tool is mostly impacted by the missing pressure sensor behind the HPT. The AM tool wrongfully contributes deterioration on the LPT to the HPT as an efficiency decrease. Also, due to the missing pressure sensor behind the fan, on-wing analysis of the fan deterioration is not possible. As the fan and the LPT are not as prone to deterioration, the conclusion was drawn that the GEnx-1B AM tool is useful for determining LPC, HPC and HPT deterioration from test cell and on-wing analysis.

To improve the model, Moorselaar recommended tuning the component maps for a large spool speed range. Both in the test cell as on-wing. Tuning for additional power settings in the test cell could lead to a better-defined fan component map. Besides, the effect of the bleed flows, power off-take, active clearance control and the variable geometry are not included in the model. Including these effects could reduce the modelling error [52].

Finally, he recommended finding a way around the limitation of only being able to estimate an equal number of deterioration modes as the available number of sensor measurements.

Turbofan Condition Monitoring using Evolutionary Algorithm based Gas Path Analysis
Following up on the research performed by Moorselaar[50], Rootliep [37] performed research to develop a method to determine more deterioration grades than measurements available. Instead of using the deterministic AM strategy, which is prone to noise and not capable of estimating more conditions N than measurements M, an evolutionary algorithm was used in combination with the MOPA approach. The evolutionary algorithm was used to find the optimum fit for the condition variables. The specific type of evolutionary algorithm that was used, is the differential algorithm. The approach used by Rootliep is described in subsection 3.1.6.

It was concluded that the MOPA-EA GPA tool is able to estimate more component conditions than measurements available. An analysis was performed to determine the sensitivity of the system to the condition parameters. It was concluded that mainly the $p_{s,3}$, $T_{t,49}$ and the fuel flow are sensitive to component deterioration. The N_2, $T_{t,25}$ and $T_{t,3}$ are a lot less sensitive to component conditions. Furthermore, an analysis was performed to determine the capabilities of the MOPA-EA GPA tool to determine the condition parameters for individual components. It was concluded that the GEnx-1B core components conditions are best identifiable.

Also, the MOPA operating points have been evaluated to determine the most accurate combination of power settings. Power settings that differ 5-8% gave the most accurate results. More than two operating points gave decreasingly accurate results. As a result, the MOPA analysis was run at take-off and a lower N_1 spool speed around cruise.

The MOPA-EA GPA tool proved to be capable of estimating condition parameters with sufficient accuracy for single and multiple deteriorated components on simulated data. In the single and double deteriorated

component cases, the MOPA-EA tool was able to determine the magnitude of the deterioration. The multiple deteriorated component analysis, which used the cruise operating point, experienced reduced accuracy but was still able to determine the trend of the deterioration on the components.

Rootliep validated his tool using in-flight data from a GEnx-1B engine that experienced multiple water washes and a turbine blade failure. It proved to indicate the expected effects corresponding to compressor fouling and the turbine blade failure. The source of data for this analysis was the continuous engine operating data (CEOD). Filtering was applied before the GPA was performed to reduce the scatter and secondary performance parameter deviations.

Despite the good performance, the MOPA-EA GPA also had a major drawback. Its computational burden is high due to its heuristic nature.

As recommendations for additional research, Rootliep suggested:

- Improving the GSP computational time by altering the source code of GSP. This should be done in collaboration with NLR.
- Further investigation of the capabilities of the GEnx-1B model at representing cruise power setting, which is off-design modelling.

Following recommendations, the off-design performance is further investigated in the following section.

3.2.2. Off-design performance

Within KLM multiple studies have been focused on increasing the off-design capabilities of GPA. Van Dorp [49] suggested the multi-reference point method and the baseline calibration method for increasing the off-design capabilities of CF6-80C2 model. Den Haan and Beishuizen [1, 3] increased the off-design gas path analysis accuracy by tuning the component maps for the CF6-80C2. These methods will be introduced.

Multiple reference point method

The multiple reference point method creates a separate model for every power setting. This eliminates the use of component maps altogether. By creating multiple models, accurate GPA can be performed at multiple power settings. The drawback of this method is that if the data point deviates from the exact power setting the model was created for, the results can have a severely reduced accuracy [3].

Baseline calibration method

Van Dorp [49] used the calibration factors introduced in subsection 3.1.5 to construct a polynomial function that describes the difference in performance between the model and the actual engine over the whole power setting range. Such function is visible in Equation 3.19. By applying the function to scale the performance parameters, off-design gas path analysis was performed without the need for multiple engine models. The principle is displayed in Figure 3.3.

$$f_i\left(n_1\right) = \frac{P_{\text{i, baseline}}\left(n_1\right)}{P_{\text{i, model}}\left(n_1\right)} \tag{3.19}$$

Improving compressor maps

Den Haan[3] applied the third method to perform accurate off-design GPA. First, he created a CF6-80C2 model and subsequently applied component map tuning to increase the off-design accuracy. The main advantage of component map tuning is that, if accurate component maps are created, only one model is needed to perform GPA for multiple power settings. Often, accurate component maps are not available for the MRO facility, only the OEM possesses the component map. Therefore, the component maps have to be recreated by establishing a fit between the results from the model and the measurement data. Den Haan concluded that this was a very laborious task if done by hand but managed to achieve an accuracy of ±0.5% difference between the measured temperatures and pressures at Max Continuous (MC) conditions. Beishuizen [1] expanded upon the component map tuning by Den Haan because he found a relation between the deterioration levels and the spool speed if AM was applied. Since the deterioration is assumed to be independent of the spool speed, this relation was to be removed. The data Beishuizen used to tune the component maps were test cell and on-wing data. Beishuizen was successful in removing the relation between the spool speeds and the deterioration levels for the fan LPC and HPC, the turbine maps were only tuned with test cell data. He applied speed line form alteration, efficiency alteration and speed line reallocation.

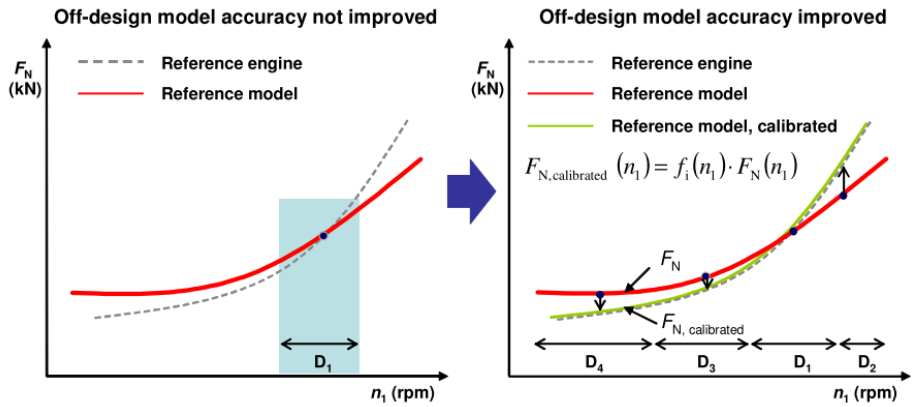

Figure 3.3: Baseline calibration method [49]

He however noted that the adaptions he made were not in line with physics. Compressor maps resemble real-world behaviour, and the maps created contained kinks and impossible efficiency islands [1].

As mentioned, Verbist and Moorselaar [50, 52] also tuned the component maps to display better off-design accuracy. Verbist only used speed line relabeling, whereas Moorselaar used speedline relabeling in combination with reallocating speedlines. The test cell component map tuning was performed to decrease the difference between the measurement and the model output. On-wing, they both used the AM tool with the goal of decreasing the relation between the spool speed and deterioration levels. This is due to the measurement noise being present on-wing, making it hard to reduce the difference by iteratively changing the component maps.

3.2.3. Conclusions on former performed research

From former performed research can mainly be concluded that:

- A decrease in sensors decreases the accuracy of the model creation due to the need for additional assumptions [50, 52].
- On-wing GPA is less accurate compared to test cell GPA due to the decrease in available sensors, measurement noise and unsteady ambient conditions [50, 52].
- The best strategy to perform off-design GPA at KLM is using GSP with component maps. However, the results depend on the correctness of these maps [1, 3].
- Bleed flows and power off-take effects should be considered in GPA [52].
- The MOPA-EA GPA has reduced accuracy on the GEnx-1B model when the cruise operating point is included [37].
- The effect of measurement noise on GPA is relatively small compared to the other sources of error [52].
- The AM strategy is becoming less applicable because of the reduced number is sensors available in contemporary engines [50].
- The MOPA-EA GPA tool is capable of dealing with measurement noise and a reduction of sensors [37].

3.3. Effects on engine performance

From the former performed research, it is clear that the Hybrid MOPA-EA GPA tool has reduced accuracy when used with on-wing GEnx-1B cruise data. Therefore a study is set out to identify the possible causes for the reduced accuracy of the GEnx-1B model at the cruise phase. This chapter is divided into three sections. The first section deals with the gas turbine component related possible causes for inaccuracies. These are called secondary performance parameters. The second part deals with ambient and flight condition influences and the third part deals with further uncertainties of on-wing GPA.

3.3.1. Secondary performance parameters

Modern gas turbines are controlled in an ingenious way to improve the performance. To do so, the engine adapts certain system setting to the operating condition. The GEnx-1B engine contains four of these systems, the bleed flows, variable geometry, active clearance control and power off-take. These parameters will be referred to as secondary performance parameters (SPPs). Since they alter the operation of the engine and are not included in the current GEnx-1B model, it is interesting to investigate how they work, what their effect is, and how they could be implemented in model creation. First, the active clearance control for the turbines is treated. After which the bleed flows, power off-take, and variable geometry are discussed.

Active clearance control and cooling

Gas turbines have a certain clearance between the stator casing and the rotor blades. By means of active clearance control, this clearance can be minimised to increase the efficiency or enlarged to prevent abrasion [31]. Both the engine induced loads as flight loads can cause abrasion. Engine induced loads include centrifugal forces, thrust, and thermal loads. The flight induced loads include gravitational forces and aerodynamic and gyroscopic loads [31]. By using thermal control, the tip clearance can be kept at an optimal value in order to prevent abrasion and keep the efficiency high. A typical active clearance control transient for a flight pattern is given in Figure 3.4.

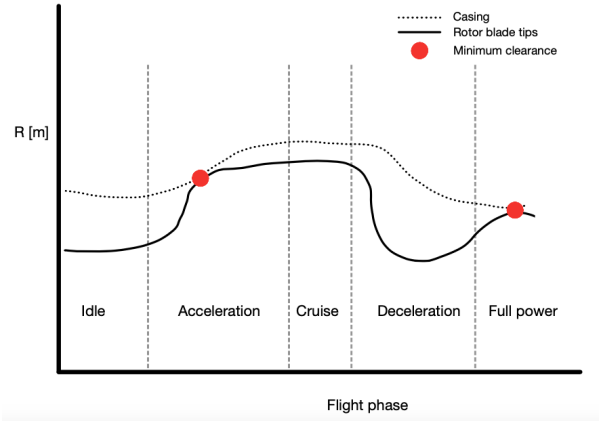

Figure 3.4: Typical tip clearance transient vs flight phase, adapted from [33]

To understand how tip clearance can influence the efficiency of turbomachinery components, it is useful to introduce the mechanisms for entropy creation. Entropy creation is the source of loss in turbomachinery components. It is created by the following three fluid dynamic processes [4]:

1. Viscous friction in the boundary layer or mixing processes.
2. Heat transfer.
3. Shock waves.

A tip clearance in turbomachinery components can lead to a mass flow from the pressure side of a rotor blade to the suction side. This leakage flow mixes out above the blade, which inherently will cause a static pressure rise and entropy production through loss mechanism 1. Also, a vortex at the suction side of the blade is created. This vortex will eventually also mix with the main stream through the turbomachinery component. Due to the flow velocity difference, this mixing will also be accompanied by mixing losses [4]. The tip leakage vortex is visualised in Figure 3.5.

The loss associated with the tip clearance can account for 30% to 45% of the total efficiency loss in the turbine stage and rotor respectively [42]. The effect of increasing the tip clearance on the turbine efficiency is studied by Yoon et al. [63]. This research pointed out that the efficiency loss caused by tip clearance is dependent on the stage loading and whether the turbine is shrouded or not. The results from this study indicate that for unshrouded turbines with a stage reaction of 50%, an isentropic efficiency loss of 2% is to be expected for a 1% tip clearance increase (% of span). The results from this study are visible in Figure 3.6. The flow capacity is also influenced by the tip clearance. However, this is influenced by a smaller magnitude.

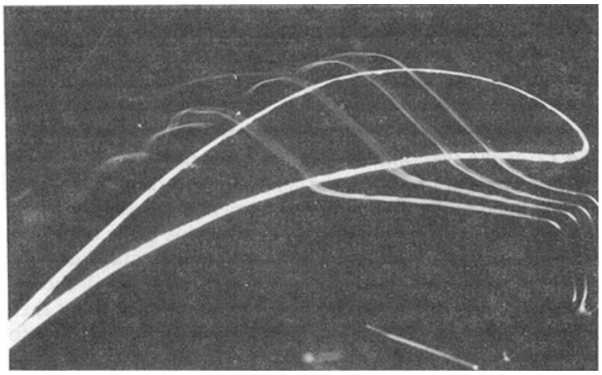

Figure 3.5: Tip leakage vortex [4]

Following Holeski [15], a 1% increase in tip clearance relative to the blade span results in an increase of 0.8% in flow capacity. This is supported by Escher [6], which relates the relation between the efficiency loss and flow capacity increase for turbine tip clearance as 2:1.

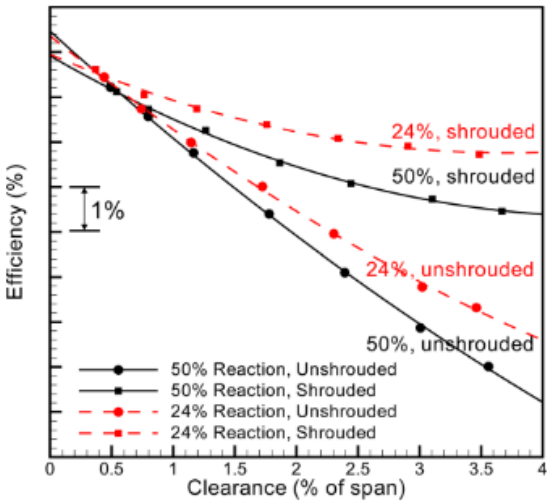

Figure 3.6: Effect of tip clearance on isentropic efficiency [63]

For engine performance modelling, this can cause difficulties. Since the engine performance is slightly different for varying tip clearances, every tip clearance might need its own component maps. Modern gas turbine engines collect data from the active clearance control system. This can be used to find regimes in the data with similar tip clearance. Also, multiple component maps can be made for multiple tip clearances.

Another option is introducing tip clearance correction factors into the GPA calculation [18]. However, this is not possible in the current GSP environment.

Bleed Flows

Gas turbines also incorporate bleed flows. Bleed flows subtract air from the core flow to be put to use in secondary systems or to improve the surge margin of the compressor. The Variable Bleed Valves (VBV) and Transient Bleed Valves (TBV) are used to improve the operation of the compressors. Often variable bleed valves are located aft of the booster and interconnect the path of the high-pressure compressor inlet to the bypass flow. This system is used to prevent stall of the LPC [13]. They discharge in the bypass flow. The transient bleed valves are located aft of the HPC. The purpose of the system is to unload the compressor during start-up and acceleration from idle [58]. They discharge in the bypass flow.

To understand how these bleed valves work, the effect of the bleeds on the velocity triangles of the compressor is indicated in Figure 3.7. The red velocity triangle in the figure displays low speed stall. By opening the bleeds downstream of the compressor, the axial velocity of the flow can be increased to prevent this

undesired behaviour. Since work is performed on air that is offloaded to the bypass, VBVs and TBVs have a negative impact on the specific fuel consumption (SFC) [58]. Also, the turbine inlet temperature will rise due to the air subtraction [7]. Since these bleeds do not alter the compressor geometry, the bleed settings will not change the compressor map. Only the boundary conditions imposed on the compressor change. Bleed flows subtracted from the compressor for secondary systems are often inter stage bleeds. Since these alter the compressor geometry, every bleed valve setting needs a separate compressor map [58]. There are multiple ways to account for these bleed flows. One option is splitting the compressor at the location of the bleed flow into multiple compressors [13]. If this is done, the compressor bleeds can be applied at the station between the compressors. This has the downside that requires multiple compressor maps for the individual compressors. A second option is assuming that all the bleed leaves the compressor at the exit. The last option is specifying a dH fraction factor. This specifies the bleed location in the form of how much of the total enthalpy rise in the compressor is applied to the bleed air. This is method is applied in GSP and does not alter the component maps [47].

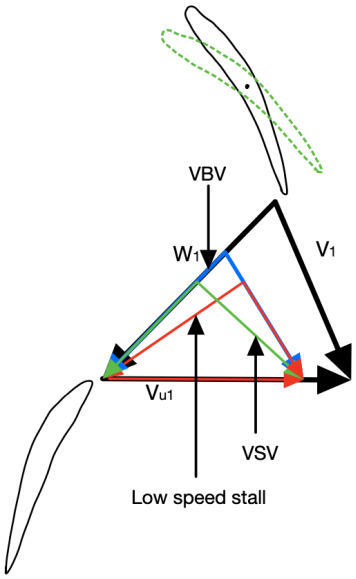

Figure 3.7: Effect of variable bleed valves and variable stator vanes on velocity triangles

In former studies, the VBVs and TBVs are assumed constant because no data was available [50, 52]. If sufficient data is available, the bleed flows can be incorporated in the GSP models.

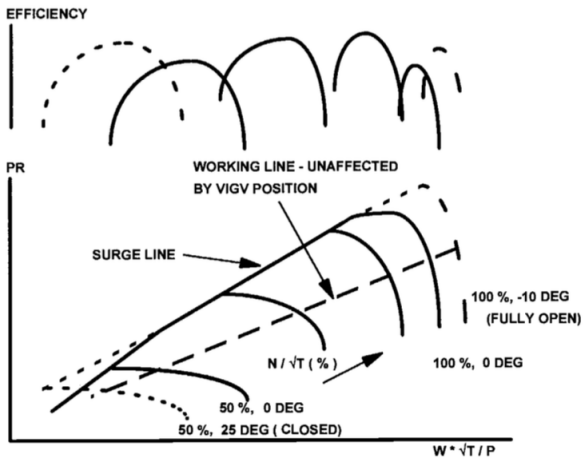

Figure 3.8: Effect of variable inlet guide vanes and variable stator vanes on compressor map [58]

Variable geometry
The Variable Stator Vanes (VSV) and Inlet Guide Vanes (IGV) assure stable operation in off-design conditions. They prevent surging of the compressor by changing their angle relative to the flow. This effect is also displayed in Figure 3.7. Closing the VSVs/IGVs induces a higher tangential inflow velocity at the rotor and a reduced axial velocity. This effect results in a decreased pressure ratio and corrected mass flow for the same corrected spool speed line [58]. The effect of the IGVs and the VSVs on the compressor map is visible in Figure 3.8. A first estimation of the ratio between the change in pressure ratio and corrected mass flow caused by the changed VSV position is 1 to 1[27]. The efficiency is a different case. In the case of VSV drift, in which the VSV angle deviates from the nominal angle, an efficiency decrease can be the result [27]. On the other hand, VSV positions can be optimised to increase the efficiency of the compressors [61]. The working line in the compressor map is unchanged by the VSVs/IGVs position, since it is determined by the components downstream.

Often the IGVs and VSVs are a function of corrected spool speed. This enables capturing their variation in one compressor map. Additionally, VSV and IGV scheduling can vary for different altitudes and transient operation. This might be beneficial for the efficiency of the turbine connected to the same spool [58]. The information about the VSV and IGV scheduling can be used to incorporate in GPA software. Further information on how the VSV/IGV schedules can be identified in compressor maps can be found in Otten [34].

Power off-take
The electric system for the cabin air and other auxiliary components of the aircraft needs a power source. The required power can be subtracted from the N_2 shaft. Power extraction from the N2 shaft will lead to an increase in turbine inlet temperature and a decreased surge margin [40]. In most GPA programs, Power off-take can be modelled directly.

3.3.2. Flight condition effects
Besides the secondary performance parameter effects that are caused by the engine itself, the on-wing situation also changes the environmental conditions. These effects are introduced in this section. The effect considered are the humidity effect, the inlet and the Reynolds number effect.

Humidity effect
In contrast to test cell data, the CEOD do not contain information about the humidity. Gas turbine performance is strongly influenced by humidity, since the gas properties R and γ of the working fluid change. From former research carried out by [36, 51] can be concluded that:

- Due to absolute humidity variation, GPA can lead to incorrect overestimating the compressor isentropic efficiency by 1% and underestimation of 1% for the turbine isentropic efficiency in very humid conditions.
- For the GE CF-6 engines, the EGTM can vary up to 12 K at take-off altitude due to humidity.
- A thrust loss of 0.6% per 1 wt% resulting in a maximum thrust loss of 2% in very humid conditions.

This indicates that humidity should be considered when performing GPA at take-off. At higher altitudes, this is not expected because the absolute humidity above 6000m can be neglected [17, 25]. Therefore cruise data has strong potential for GPA due to less variation of ambient conditions.

Inlet
The inlet bellmouth in the test cell is different compared to the on-wing inlet situation. Whereas the test cell inlet is focused on providing non-distorted flow for the engine, the on-wing inlet is designed to decrease the Mach number at the fan face at cruise conditions [29]. Therefore, it acts as a diffuser to decrease the Mach number from flight Mach number to Mach 0.6-0.7.

The performance of a subsonic inlet is dependent on the throat Mach number and the contraction ratio. The contraction ratio is the ratio between the ingested stream tube area A_0 and the inlet capture area A_C. At take-off, the flight Mach number is low and therefore, the ingested stream tube is larger than the inlet capture area, $A_0/A_C > 1$. This can cause separation at the lip of the inlet and therefore a total pressure loss and non-uniform flow at the fan face [28]. When the flight Mach number increases, the ingested stream tube area decreases, $A_0/A_C < 1$ and separation is prevented.

Therefore, the inlet causes a twofold in discrepancies in GPA. Firstly there is a difference between the on-wing take-off and test cell situation due to a different inlet shape. On-wing take-off conditions deal with separation and non-uniform inflow. This can lead to the fan operating in multiple parts of the compressor map, also in suboptimal areas of efficiency [28]. The distorted areas of the fan will operate closer to the surge margin. This can affect the GPA results.

Secondly, there is also a difference between the on-wing take-off and cruise situation. In cruise, the contraction ratio is small and no separation is expected. This can cause a difference between cruise and take-off performance.

Reynolds number effect

The Reynolds number also influences gas turbine performance. Since Reynolds number is dependent on Mach number and altitude [25], it is important to consider its effect. The variation with altitude and Mach number is displayed in Figure 3.9. The civil aircraft operating range is given in Figure 3.9.

Schaffler [41] performed an experiment to indicate the effect of Reynolds number and blade roughness on axial compressors. As is visible in Figure 3.10, the polytropic efficiency increases with increasing Reynolds number until the critical Reynolds number which is determined by the surface roughness. Also, a decreasing Reynolds number increases the viscous losses. Therefore increasing the altitude has a detrimental effect on compressor efficiency. This indicates the importance of considering the Reynolds number in GPA.

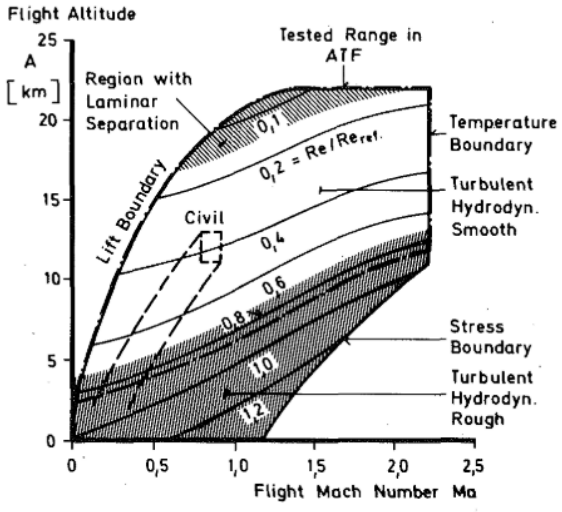

Figure 3.9: Effect of altitude and mach number on Reynolds number [41]

3.3.3. Uncertainties

Besides on-wing effects, on-wing data also introduces other uncertainties. The uncertainties discussed are the measurement error and the steady-state assumption.

Measurement error

The sensors of gas turbine engines all have their accuracy and range. Since the measurement error of these sensors can propagate through into the GPA results, it is of importance to know their accuracy. By using a Monte Carlo simulation, these effects can be quantified [50]. This is performed for the GEnx-1B engine. The conclusion was that the components on the N_2 shaft are most prone to sensor noise. The AM Monte Carlo simulation found a standard deviation of 0.25-0.5% on the component deviations for the HPC and HPT flow capacity and isentropic efficiency [50]. Since the pressure sensor between the LPC and HPC is not present in the GEnx-1B, this was deemed a logical result.

Thermal steady-state assumption

For GPA, a certain steady thermal state of the engine is assumed. In the test cell, this thermal state can be assured by a 10-minute warming up period for the engine. For on-wing take-off analysis, this assumption

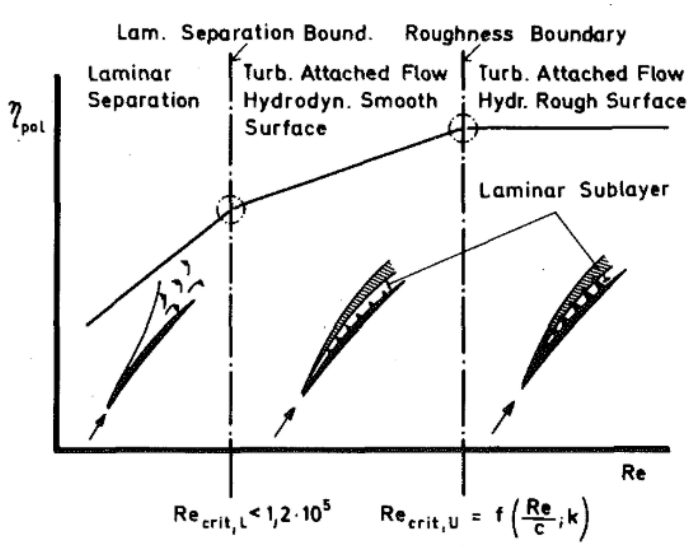

Figure 3.10: Effect of Reynolds number on polytropic efficiency [25]

does not always hold. The research from Röell [36] had shown that this steady-state assumption in take-off data is not valid. The thermal state of the engine is identified as the main contributor to the standard deviation of the EGTM for on-wing take-off on the CF-6. Using cruise data, in which thermal stability is assured, can potentially reduce the uncertainty effects of on-wing GPA.

3.3.4. Conclusion on effects on engine performance

From this section can be concluded that the secondary performance parameters can drastically influence gas turbine performance, and should therefore be taken into account in GPA. Also, the flight condition effects and further uncertainties should be included in the GPA analysis. If the setting of the secondary performance parameters and the ambient conditions differ for cruise and take-off, including these in GPA can potentially increase the accuracy of the GPA model.

3.4. Conclusions

A brief literature review uncovered that the cruise operating point is not accurately modelled by the current GEnx-1B model. As GPA results are influenced by the quality of the engine model, the research objective of this project is to increase the accuracy of the GEnx-1B model at cruise conditions.

This model is created by Moorselaar [50], and it is capable of accurately representing the take-off operating point. Also, its component maps have been tuned over a large range of corrected spool speeds. The main area of potential improvement in order to increase the accuracy of the model for cruise conditions is the incorporation of the secondary performance parameters. Hence, this thesis will introduce a method to account for the secondary performance parameters to increase the accuracy of GPA models. The following section describes the methodology.

II

Accounting for secondary performance parameters in gas path analysis

4

Methodology

As indicated by the former chapter, secondary performance parameters influence the gas turbine behaviour. Since the current GEnx-1B model does not account for these effects, it is interesting to research the possibility of improving GPA models by taking these effects into account. In this chapter, the methodology is set out. In the first section, a general introduction to the simulation framework is given. The second section explains methods to account for the secondary performance parameters, after which the third section introduces the algorithm to do so. Subsequently, a proof of concept is displayed on simulated data. Lastly, an analysis is performed on the algorithm settings after which conclusions are drawn.

4.1. GSP

In this section, the GPA software is introduced after which a standard GSP model is displayed. This model will be used for the proof of concept of the algorithm.

4.1.1. GSP API

For this project, two main software packages are used. GSP and 32-bit Python 3.8 with the Spyder 4.1.5 environment. GSP is a program implemented in the object-oriented Borland Delphi environment. The specific version used is the GSP Application Programming Interface (API) version. This API version enables communication with 32-bit Python via a Dynamic-Link Library (DLL), which essentially is a Windows application written in C++. 32-bit Python is used instead of the more commonly used 64-bit version due to compatibility issues with the DLL. This setup enables direct control of the GSP functionalities from the Python environment.

4.1.2. BIGFAN model

Within the GSP environment, engine models can be created, and simulations can be performed. To describe the simulation procedure and test the methodology, a standard model from the GSP library is introduced. Based on this model, the simulation inputs and outputs are displayed.

Since this report contains a case study regarding the high-bypass ratio GEnx-1B turbofan engine, a likewise high-bypass ratio engine is used for testing the methodology. GSP contains the standard BIGFAN model which is a two-spool engine with a bypass ratio of 5. The graphical representation is given in Figure 4.1.

To simulate an engine at various ambient conditions, power settings and deterioration grades, GSP is controlled by the API block in Figure 4.1, which is linked to python. The ambient conditions are specified by the ambient pressure, temperature, Mach number and humidity. The power setting can be specified by the N_1 rotational speed or the fuel mass flow. The component deterioration is specified as a delta efficiency $\Delta\eta$ and delta flow capacity W_c for the individual components. As explained in section 2.4, these delta parameters modify the component maps influencing the gas turbine model performance. These are called map modifiers.

When a simulation is run, GSP calculates various properties at the distinct station numbers following 0-D simulation practice. For gas path analysis, often pressures temperatures, rotational speeds and fuel mass flow are measured in the gas path. Therefore these properties are used as output from the engine model to compare with the measurements.

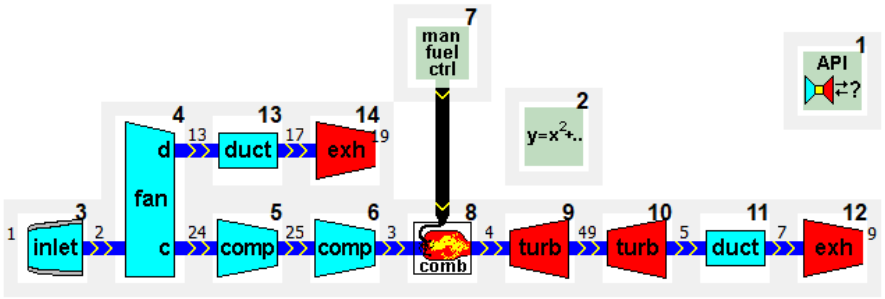

Figure 4.1: BIGFAN GSP model

4.2. Accounting for secondary performance parameters

As mentioned in section 3.3, most secondary performance parameters influence the gas turbine performance. Therefore, if not taken into account by the engine model, they can cause a deviation between the sensor measurements and the model output. When performing GPA, these deviations can show up as component deterioration. Therefore, accounting for these effects by adapting the model prior to performing GPA can reduce the error in the results. The possible secondary performance effects identified in section 3.3 are the power off-take, the bleed flows, the turbine clearance and the variable geometry. Since the current GEnx-1B model does not incorporate these effects, it is interesting to research the possibility of incorporating these parameters in the engine model. A distinction is made between two types of secondary performance parameters.

- Secondary performance parameters modelled as imposed on the gas turbine as a whole, not changing the performance of individual components. Also called effects on system performance.
- Secondary performance parameters that influence individual component geometry and, therefore component performance. Also called effects on component performance.

In this section, the method of modelling the secondary performance parameters imposed on the gas turbine is introduced. Subsequently, the method of accounting for the secondary performance parameters that alter the component geometry is explained. Finally, a method for parametrisation is introduced.

4.2.1. Effects on system performance

This first category consists of secondary performance parameters that are modelled as effects on the system as a whole. This category contains the power off-take and the bleed flows. These secondary performance parameters can be modelled directly into the GPA analysis by making use of the GSP functionality.

Power Take-Off

The Power Take-Off can be modelled in GSP by specifying a certain value of kW that is extracted from an axis [47]. If this power value is known, it can be modelled directly.

Bleed flows

There are two types of bleed flows: inter-stage bleed flows and inter-component bleed flows. For modelling both types, the GSP functionality can be used. The inter-component bleed flows can be modelled by indicating a fraction of mass flow or corrected mass flow [47]. In the case of available data, this can increase the accuracy of the model. The inter-stage bleed flows can also be accounted for by the bleed flow functionality of GSP. With this functionality, the location of the bleed in the component can be specified by setting the dH fraction [47]. This parameter defines the fraction of the total enthalpy rise already added to the extracted air before it is bled off.

Since these secondary performance parameters can be modelled directly by using the GSP functionality, they will not be further analysed in this thesis. The following section will introduce secondary performance parameters of which the effect cannot be directly modelled.

4.2.2. Effects on component performance

As indicated in section 3.3, the tip clearance and variable geometry have their distinct effect on component performance. Since the performance of gas turbine components is mapped in component maps, alteration of the component maps based on the secondary performance parameter value introduces the possibility to account for the variation of these secondary performance parameters. To do so, the map modifiers $\Delta\eta$ and W_c can be related to the setting of the secondary performance parameter. The expected effect of the secondary performance parameters is introduced in the following section.

Tip clearance

As mentioned in section 3.3, the tip clearance affects the performance. An increase in tip clearance in the turbines leads to a decreased efficiency and an increase in flow capacity. A correction in the component map can be implemented to account for these performance differences.

Variable geometry

As mentioned in section 3.3, often, the variable stator vane and inlet guide vane position is a function of corrected spool speed. In case of an additional relationship, this can also be implemented in the component maps. Closing the vanes can reduce the flow capacity of the compressor and increase or decrease the efficiency.

To summarise, these effects are visualised in Table 4.1. In contrast to the effect on system performance, the exact magnitude of the effect on component performance from these secondary performance parameters is not clear. Hence their effect needs to be identified. The following section will first introduce a method to relate a certain secondary performance parameter setting to a ΔW_c or a $\Delta\eta$.

Secondary performance parameter	W_c change	η change
Compressor VSV/IGV closing [27]	⇓	⇳
Turbine clearance decrease [6]	⇓	⇑

Table 4.1: Effect of secondary performance parameter on component performance map

4.2.3. Secondary performance parameter parameterisation

As indicated in the former section, a method for parameterisation of the tip clearance and variable geometry effect on component performance is needed. When operating conditions change, secondary performance parameters (SPPs) adapt to the new conditions. Since a GPA model is calibrated for a certain setting of these SPPs, another operating condition can deviate in terms of these settings. To capture these differences in the GPA model, relationships are drawn up between the SPP setting and the map modifiers ΔW_c and $\Delta\eta$. The parameterisation function used to define these relationships is visualised in Equation 4.1. In this equation, the parameters are defined as follows:

- SPP_{DP} is the setting of the SPP in the design point of the model.
- SPP_{OD}, is the SPP setting for various operating points (off-design).
- PD is component performance deviation $\Delta\eta$ or ΔW_c for the component map that is influenced by the secondary performance parameter.
- Performance deviation coefficients a and b define the magnitude of the relationship.

$$PD_{component,performance\ deviation}(a,b) = a\left(\left|\frac{SPP_{OD}-SPP_{DP}}{SPP_{DP}}\right|\right) + b\left(\left|\frac{SPP_{OD}-SPP_{DP}}{SPP_{DP}}\right|\right)^2 \tag{4.1}$$

One such relationship is shown in Figure 4.2. The shown curve relates the VSV/IGV setting difference between the calibrated model (DP) and a certain off-design operating point (OD) by defining a $\Delta\eta$ for the HPC. For example, a relative difference of 0.15 in VSV/IGV angle would result in an efficiency increase of 1% for the HPC. The relationships always go through the origin because a 0% deviation in SPP setting would mean no performance difference compared to the SPP setting the model was created for. The larger the difference

between the SPP setting at which the model is calibrated (design point DP) and the actual SPP setting (off-design OD), the larger the performance deviations.

Since the exact magnitude of the relationships is unknown, the following section introduces an algorithm to find the relationships.

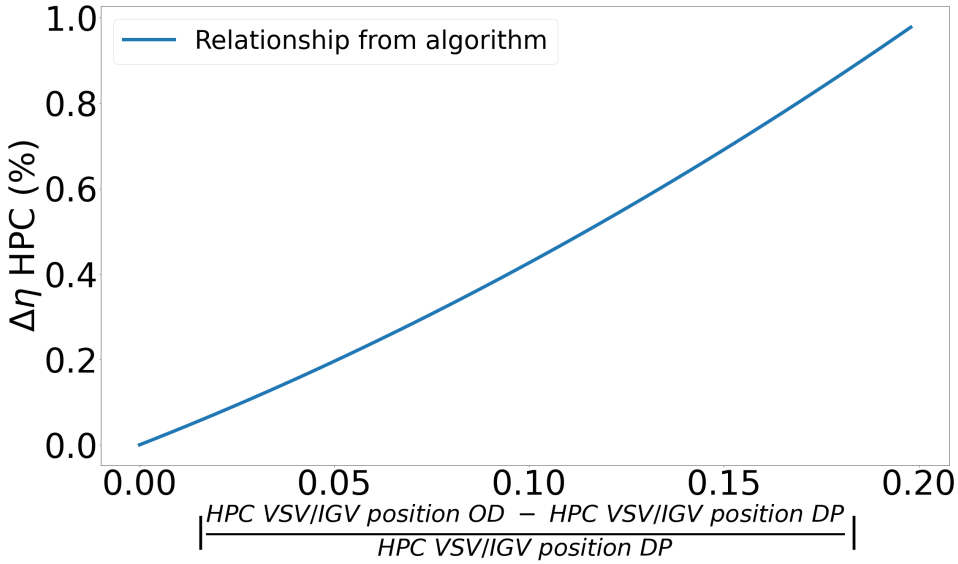

Figure 4.2: Example of relationship between SPP deviation and component performance deviation

4.3. Algorithm

As mentioned, gas turbine performance data is influenced by secondary performance parameter settings. Hence, the output from an engine model deviates from the engine measurements if the model is calibrated for different SPP settings. This deviation can be used to identify the former mentioned relationships that capture SPP effects.

In this section, an algorithm is introduced. This algorithm tries to find a set of relationships to create a better fit between model output and a dataset with measurements that are influenced by the secondary performance parameter effects. By reverse engineering, relationships can be determined. If accurate relationships are defined, they can be embedded in the engine model to increase its accuracy. First, the objective function is introduced, after which the evaluation function and the optimisation algorithm are introduced.

4.3.1. Objective function

The goal of the algorithm is to decrease the deviation between the on-wing measured parameters (Z) that are influenced by secondary performance parameters and the model output (R). Therefore an objective function is constructed that evaluates this difference by using a root mean square of this deviation for the number of operating points evaluated. Multiple operating points are evaluated because the effects of individual secondary performance parameter effects are not revealed by a single operating point evaluation. This is essentially application of the MOPA strategy [45] from section subsection 3.1.6.

The objective function is given in Equation 4.2 in which OP is the number of operating points and $MEAS$ is the number of measurements and model outputs.

$$f(x) = \sqrt{\frac{\sum_{t=1}^{OP}\sum_{m=1}^{MEAS}\left(\frac{Z_{t,m}-R_{t,m}}{Z_{t,m}}\right)^2}{OP \cdot MEAS}} \tag{4.2}$$

To evaluate this objective function, the GSP model is run at various operating conditions with a certain set of relationships. The procedure is specified in the following section.

4.3.2. GSP code

To evaluate the objective function, a certain function is needed. This function is given in pseudocode in algorithm 1. This function is able to test a set of performance deviation coefficients on multiple on-wing operation points. The inputs to the function are:

- Set of performance deviation coefficients $u_{i,G+1}$, which is generated by the optimiser. These determine the shape of the relationships.
- Z On-wing measurement data with number of operating points OP and measurement values MEAS.
- C On-wing ambient and operating condition data with number of operating points OP.
- S SPP information with number of operating points OP and number of secondary performance parameters SPP.

To test a set of relationships, GSP is run at multiple operating points with corresponding secondary performance parameter settings. For every operating point, the SPP settings are used together with the relationships to determine the performance deviation ΔW_c and $\Delta\eta$ of the influenced components. With the component performance deviation implemented in the model, the model is run and the output is compared to measurement data.

A good set of relationships gives a low objective function value because the difference between the model output and the measurements is small. To optimise the vector of performance deviation coefficients to get the best fit with the measurement data, a differential algorithm is used. In the following section, this algorithm is introduced.

Algorithm 1: Evaluation function GSP

Input: $u_{i,G+1}$,Z,C,S,
Output: Object function value
Initialization engine model ;
for *t=1:OP* **do**
  for *s=1:SPP* **do**
    Calculate performance deviations for the various SPPs S from generated performance deviation coefficients;
    $PD_{s,\eta}(u_{i,G+1}) = u_{1,i,G+1}\left(\left|\frac{S_{t,s}-SPP_{DP}}{SPP_{DP}}\right|\right) + u_{2,i,G+1}\left(\left|\frac{S_{t,s}-SPP_{DP}}{SPP_{DP}}\right|\right)^2$
    $PD_{s,W_c}(u_{i,G+1}) = u_{3,i,G+1}\left(\left|\frac{S_{t,s}-SPP_{DP}}{SPP_{DP}}\right|\right) + u_{4,i,G+1}\left(\left|\frac{S_{t,s}-SPP_{DP}}{SPP_{DP}}\right|\right)^2$
  end
  Run GSP engine model at various conditions with performance deviation for the engine components to create model output data F;
  $F_{t,m} = GSP(PD_\eta, PD_{w_c}, C_j)$
end
Evaluate object function which is the root mean square of the difference between the measured values on-wing and the output of the GSP model f(x)=$\sqrt{\frac{\sum_{t=1}^{OP}\sum_{m=1}^{MEAS}\left(\frac{Z_{t,m}-R_{t,m}}{Z_{t,m}}\right)^2}{OP\cdot MEAS}}$

4.3.3. Differential algorithm

The differential algorithm is a heuristic optimisation algorithm that is able to cope with multiple local minima and noisy data [46]. It mimics evolution theory as explained in subsection 3.1.6.

Optimising the vector of performance deviation coefficients is a multi-variate problem. Since multiple SPPs can affect the same output parameter, it is expected that multiple local minima exist. This can cause problems when using gradient-based optimisers because these can get stuck in local minima. The ability of heuristic optimisers to deal with a solution space with multiple local minima makes it a suitable algorithm for this application. Besides, the on-wing data contains noise. Since it is also able to work with noisy data, it is a solid choice for this optimisation.

The differential algorithm follows the same analogy as the genetic algorithm from subsection 3.1.6. The algorithm is divided into four steps: initiation, crossover, mutation and selection. These steps are shortly explained below and also given in the pseudocode in algorithm 2.

1) Initiation
For the algorithm to be initiated, a population with target vectors $x_{i,G}$ with $i = 1,2,3,...,NP$ is generated covering the entire parameter space. In this application, the target vectors contain sets of performance deviation coefficients that determine the relationship between the secondary performance parameters and the performance deviation of the components. With this initial population, algorithm 1 is run one time to get the objective function values for the target vectors. The second step is mutation.

2) Mutation
In the mutation step, target vectors are combined to create mutant vectors. This is done by the following procedure. A mutant vector $v_{i,G+1}$ is created for every target vector by using Equation 4.3. In this equation $r_1, r_2, r_3 \in \{1,2,\ldots,NP\}$ are random non-equal integers defining the indexes of the individuals that are combined. The selected integers define which three target vectors are combined to construct the values for the mutant vector. These r values should also be different from i, setting the minimal population size NP at 4. F is the amplification factor $\in [0,2]$ that determines the influence of the mutation. With these mutant vectors, the crossover is performed.

$$v_{i,G+1} = x_{r_1,G} + F \cdot \left(x_{r_2,G} - x_{r_3,G}\right) \tag{4.3}$$

3) Crossover
Crossover is introduced to increase the diversity of the variables for the individuals in the next generation population. In this step, the mutant vector and the target vectors are combined to form new trial vectors. These trial vectors are then used to compute the objective function value. The crossover is defined by and performed on the mutant vector $v_{i,G+1}$ and the target vector $x_{ji,G}$ to form the trial vector $u_{ji,G+1}$:

$$u_{ji,G+1} = \left(u_{1i,G+1}, u_{2i,G+1}, \ldots, u_{Di,G+1}\right) \tag{4.4}$$

In which:

$$u_{ji,G+1} = \begin{cases} v_{ji,G+1} & \text{if (rand}\, b(j) \leq CR) \text{ or } j = \text{rnbr}(i) \\ x_{ji,G} & \text{if (rand } b(j) > CR) \text{ and } j \neq \text{rnbr}(i) \end{cases} \tag{4.5}$$

With rand $b(j)$ as random number generator $\in [0,1]$. CR $\in [0,1]$, as the crossover constant to be determined by the programmer and rnbr(i) as a random index number to assure that $u_{ji}, G+1$ contains at least one variable from $v_{ji}, G+1$. This trial vector $u_{ji}, G+1$ is used as input to the GSP code specified in algorithm 1 and has as output the objective function value.

4) Selection
To determine if the trial vector $u_{ji,G+1}$ should be included in the next generation $x_{ji,G+1}$, the objective function value is evaluated and compared to the objective function value of current $x_{ji,G}$. This is called the greedy criterion. Only if $x_{ji,G+1}$ gives a favorable objective function value, $x_{ji,G}$ is replaced. This is iterated until the maximum number of iterations is reached.

As the trial vector will only replace the target vector, if it results in a lower objective function value, the next generation will exist out of generation with target vectors corresponding to lower objective function values. The mutation within the next generation will therefore mutate with target vectors that give a better fit between on-wing and model output data. If this continues throughout the generations, this will result in optimisation. By this principle, a set of performance deviation coefficients can be found that decreases the difference between the model and the on-wing data to within satisfactory bounds. By applying this on a dataset from a new engine from which the information about the SPPs is available, the performance deviations caused by the SPPs can be identified and captured in relationships for every SPP. A flowchart of the methodology is given in Figure 4.3.

Algorithm 2: Differential algorithm for component map adaptation based on SPP setting

Output: Best found solution

1) Initialisation

Generate initial population x^0 of performance deviation coefficients[D · NP];

for *i=1:NP* **do**

  Objfunval=$GSP(x_{i,0}$,Z,C,S)

end

while *count<Q* **do**

  for *i=1:NP* **do**

    2) Mutation

    Generate three random indexes r_1, r_2 and r_3 with $r1 \neq r2 \neq r3 \neq i$;

    $v_{i,G+1} = x_{r1,G} + F \cdot \left(x_{r_2,G} - x_{r_3,G}\right)$ creates the mutant vector;

    3) Crossover

    A trial vector is created for the target vector and the mutant vector in the crossover;

    $u_{i,G+1} = \left(u_{1i,G+1}, u_{2i,G+1}, \ldots, u_{Di,G+1}\right)$

    In which; $u_{ji,G+1} = \begin{cases} v_{ji,G+1} & \text{if (randb}(j) \leq CR) \text{ or } j = \text{rnbr}(i) \\ x_{ji,G} & \text{if (rand } b(j) > CR) \text{ and } j \neq \text{rnbr}(i) \end{cases}$

    Evaluate object function from algorithm 1;

    Objfunval=$GSP(u_{i,G+1}$,Z,C,S)

  end

  4) Selection

  Based on the object function values the trial vector is evaluated. If the objective function value from the trial vector $u_{i,G+1}$ is lower than the objective function value from the target vector $x_{i,G}$, $u_{i,G+1}$ replaces x_i in $x_{i,G+1}$

end

;

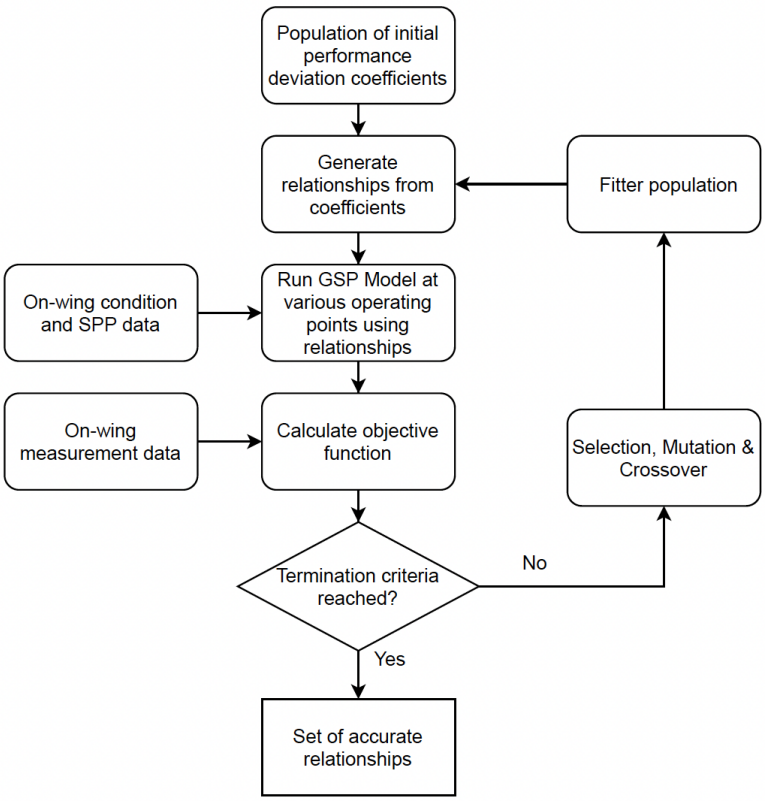

Figure 4.3: Flowchart of methodology

4.4. Proof of concept on simulated data

To verify the algorithm, a trial is performed with simulated data based on the BIGFAN model. For this trial, relationships are determined between the SPP setting and the performance of the HPC, the HPT and the LPT. These relationships are first introduced, after which the results of the algorithm are clarified. The results contain an analysis on a model with a complete sensor set, reduced sensor set and an analysis with noisy data.

4.4.1. Simulated secondary performance parameters

For the compressor and the turbines, two different forms of secondary performance parameters are used in the trial. For the HPC, closing variable stator vanes are used that reduce the flow capacity and increase the efficiency slightly. For the HPT and LPT, a clearance decrease is simulated, which causes a reduced flow capacity and increased efficiency. To quantify these effects, relationships are constructed that link these properties by using Equation 4.1. Therefore coefficients are chosen. These are visualised in Table 4.2.

performance deviation coefficient	value	description
a	5	First efficiency coefficient HPC
b	10	Second efficiency coefficient HPC
c	-4	First efficiency coefficient HPT
d	-7	Second efficiency coefficient HPT
e	8	First efficiency coefficient LPT
f	10	Second efficiency coefficient LPT
g	-6	First flow capacity coefficient HPC
h	-2	Second flow capacity coefficient HPC
i	3	First flow capacity coefficient HPT
j	6	First flow capacity coefficient HPT
k	-8	First flow capacity coefficient LPT
l	-6	Second flow capacity coefficient LPT

Table 4.2: Coefficients used to make sample data

With these coefficients, simulated data is created. This is done by creating a dataset with operating points with varying power setting N_1, in combination with randomised SPP settings. The SPP settings are converted to $\Delta\eta$ and ΔW_c for the HPC, HPT and the LPT by Equation 4.1. The engine model is run, and the model outputs are saved.

When the model is run without taking the secondary performance parameters into account, the model output data will deviate from the created dataset. The goal of the algorithm is to be able to find the relationships that were used to create the simulated data.

To test the algorithm, a first analysis is run with a set of model outputs that fully defines the performance of the HPC, HPT and LPT. This means that the output set contains the pressures and temperatures at the inlet and outlet of these components. Subsequently, an analysis is performed with reduced measurements to represent the GEnx-1B engine, which is the subject of the case study. Finally, to test the capabilities of the algorithm to deal with noise, an analysis is performed on noisy data.

The next section will introduce the results of the algorithm. The results are evaluated in two ways:

- Rms_{OP}, root mean square error of the deviation between the simulated measurement points and the model output, which is the objective function value.
- Rms_{curves}, root mean square error of the deviation between the determined relationships by the algorithm and the simulated relationships.

This is done to see if a low rms_{OP} value of the algorithm also means that the determined relationships are similar to the simulated relationships (low rms_{curves}).

4.4.2. Results of algorithm with complete sensor set

To display the working of the algorithm, a run is performed with a measurement set that fully defines the in and outlet conditions of components that are influenced by the SPPs. The measurement set used contains values from TT_{25}, TT_3, TT_4, TT_{49}, TT_5, PT_{25}, PT_3, PT_4, PT_{49}, PT_5, W_f and N_2. The station numbering follows Standard ARP engine station numbering [58]. A graphical representation is given in Appendix B.

To visualise the performance of the algorithm to reproduce the relationships that are defined by the coefficients from Table 4.2, the generated relationships are plotted against the simulated relationships in Figure 4.4.

With the full sensor set, the simulated relationships are reproduced by the algorithm very accurately. This is also represented by the rms_{OP} value, which is 0.00165. The rms_{curves} value is 0.0185. To further decrease the deviation, the algorithm can be run for a longer time. Due to its heuristic nature, the chances of a good solution become larger if the algorithm goes through more iterations. Overall, the performance of the algorithm is very good, and the relationships can be used to increase the accuracy of the engine model.

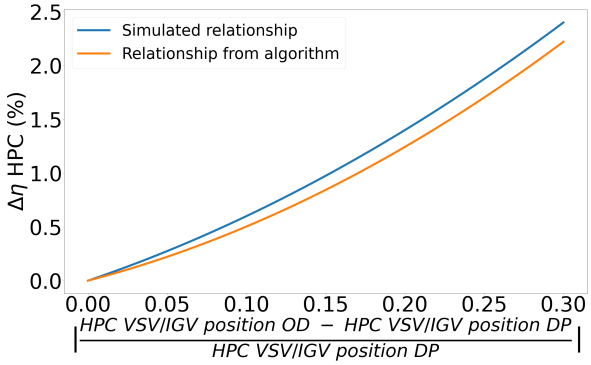

(a) $\Delta\eta$ vs HPC VSV/IGV deviation relationships

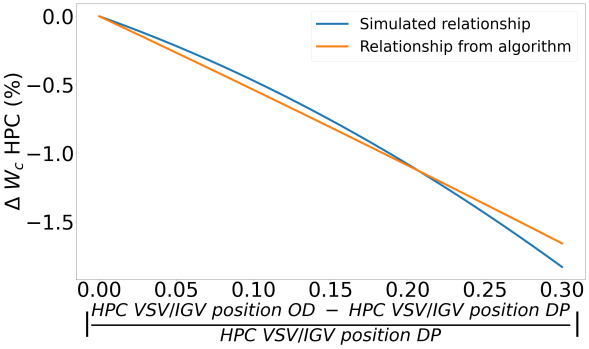

(b) ΔW_c vs HPC VSV/IGV deviation relationships

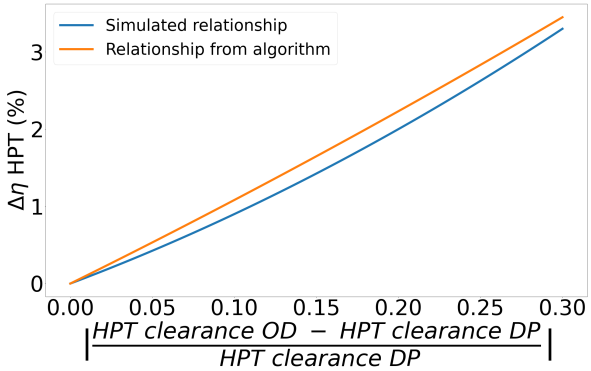

(c) $\Delta\eta$ vs HPT clearance deviation relationships

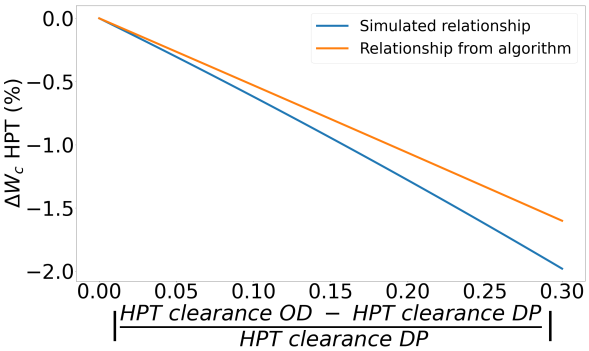

(d) ΔW_c vs HPT clearance deviation relationships

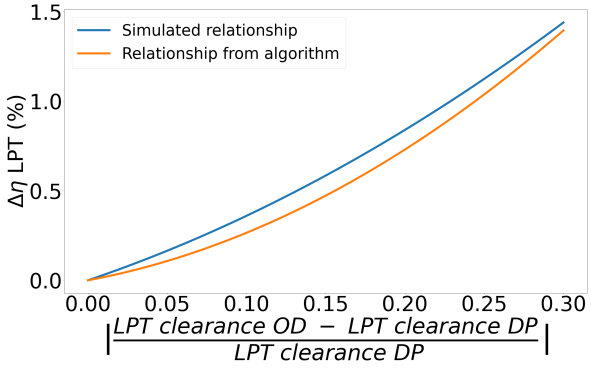

(e) $\Delta\eta$ vs LPT clearance deviation relationships

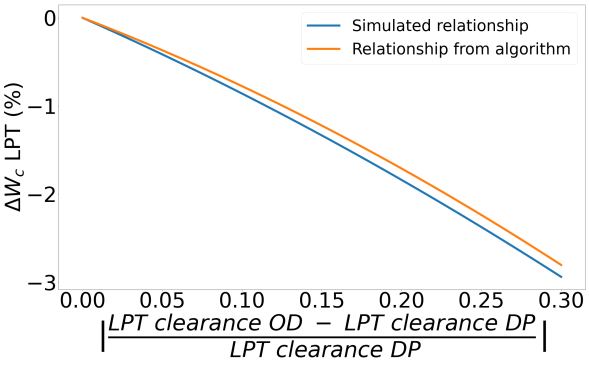

(f) ΔW_c vs LPT clearance deviation relationships

Figure 4.4: Simulated relationships vs relationships from algorithm with all measurements

Optimiser results

The results from the optimisation are also displayed in Figure 4.5. In this figure, the rms_{OP} and the performance deviation coefficient values are displayed through the iterations. Also, the final vector with performance deviation coefficients is displayed here plotted against the simulated values. What is interesting to see is that the output of the algorithm in terms of performance deviation coefficients is not equal to the input of the simulated coefficients. This is caused by the fact that the parametrisation of the relationships can have multiple combinations of the two variables to form an approximately equal curve, as indicated by Figure 4.4.

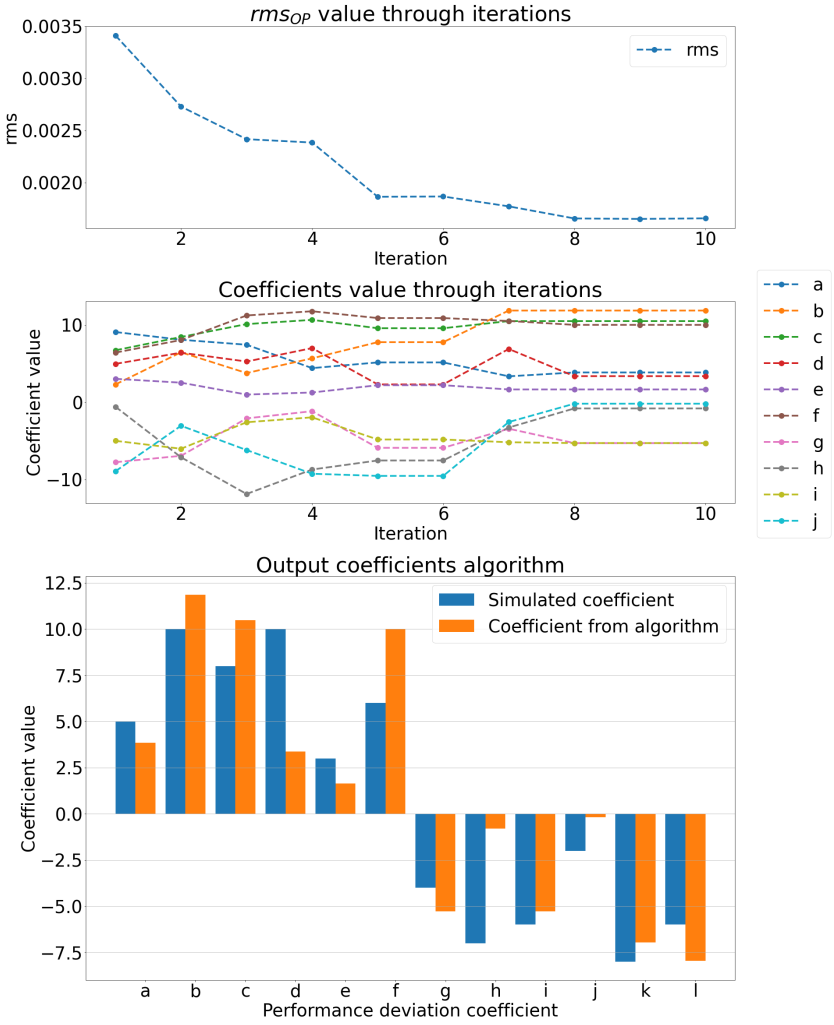

Figure 4.5: Results from simulation with complete sensor set

4.4.3. Results of the algorithm with reduced sensors

Since the GEnx-1B engine is the subject of the case study presented in this thesis, it is interesting to evaluate the performance of the algorithm when it is used with the GEnx-1B measurement set. This measurement set contains the following measurements: TT_{25}, TT_3, TT_{49}, PS_3, W_f and N_2. This measurement set does not completely define the inlet and outlet conditions around the components. To display the ability of the algorithm to deal with this matter, the results are introduced below.

The results are displayed in Figure 4.6 in the same format as before. The algorithm is clearly capable of determining the relationships that were used to generate the simulated dataset with a certain degree of tolerance. However, as is visible in Figure 4.6a, Figure 4.6b, Figure 4.6c, the generated relationships deviate more from the simulated relationships compared to the case with the complete sensor set. This can be explained by the phenomenon of smearing.

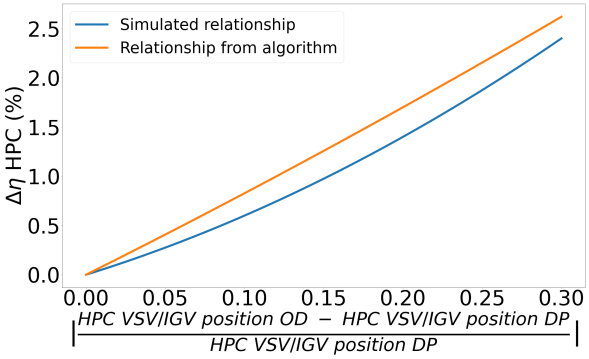

(a) $\Delta\eta$ vs HPC VSV/IGV deviation relationships

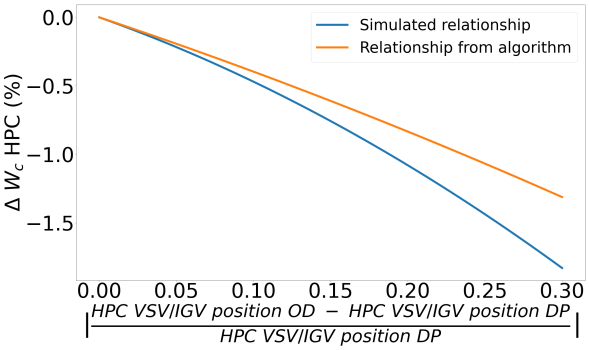

(b) ΔW_c vs HPC VSV/IGV deviation relationships

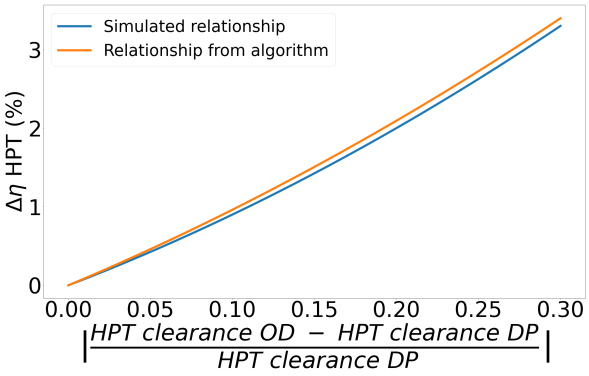

(c) $\Delta\eta$ vs HPT clearance deviation relationships

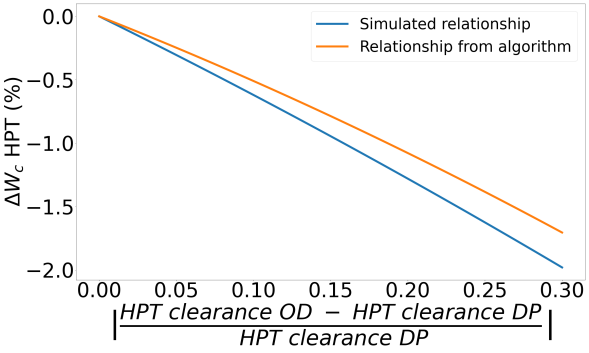

(d) ΔW_c vs HPT clearance deviation relationships

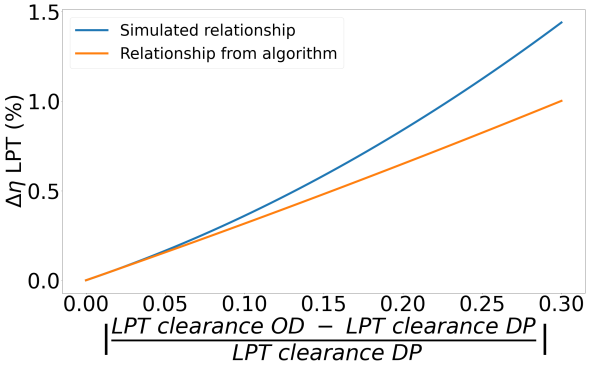

(e) $\Delta\eta$ vs LPT clearance deviation relationships

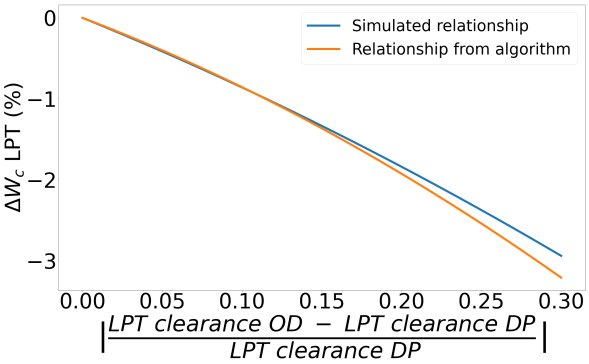

(f) ΔW_c vs LPT clearance deviation relationships

Figure 4.6: Simulated relationships vs relationships from algorithm with reduced sensors

Smearing
Smearing means that a certain performance deviation in one component is wrongfully assigned to a different component. If components are not fully defined, meaning information is missing at the in and/or outlet of the component, the component performance can not be completely determined. Due to the complex working of gas turbines, a deviation in LPT performance can influence the measurements around the HPC. To display this behaviour, a sensitivity analysis is performed and visualised in Figure 4.7. This figure displays the effect of a 1% increase in flow capacity and efficiency on the measurement set parameters. A negative value means that the output of the model is decreased by the 1% positive performance deviation.

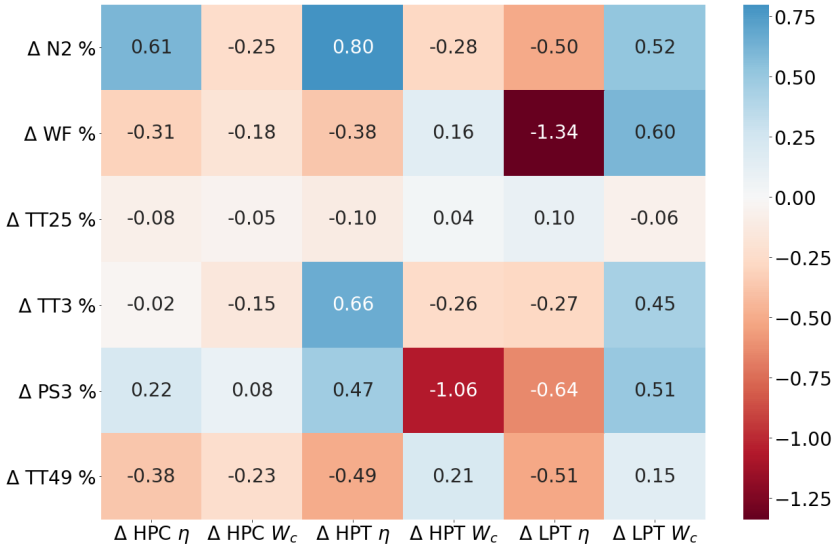

Figure 4.7: Sensitivity analysis

As is visible, the component performance does not only affect the values at their inlet and outlet conditions. This can explain the fact that a higher $\Delta\eta$ for the HPC can be compensated for by a lower $\Delta\eta$ for the LPT. Hereby, a low rms_{OP} value can be obtained that is not the global minimum. The amount of smearing is quantified by the rms_{curves} value. In this case the rms_{curves} is 0.0313. This is clearly higher than the fully defined case.

Optimiser results
The results from the algorithm run are visualised in Appendix C in Figure C.1. In this figure, the rms_{OP} from the objective function and the performance deviation coefficients are plotted against the iteration number. The final rms_{OP} value is 0.27. This is higher than the case with the full sensor set. This is caused by smearing, which decreases the ability of the algorithm to approach the simulated relationships.

4.4.4. Results of the algorithm on noisy simulated data

Each sensor in a gas turbine is influenced by noise and bias. Noise is the random deviation of a measurement from the averaged measured value. This can be modelled as a probability density function. Bias is the deviation of the averaged measured value from the actual value. This is visualised in Figure 4.8.

The algorithm adapts its relationships to minimise the difference between the model output and the measured values. Therefore, if the measurement values are off due to noise and bias, this influences the algorithm output. This section will perform an analysis to evaluate the capability of the algorithm to deal with this issue. First, the method for noise simulation is introduced, after which the results are discussed.

Noise simulation
The severity of the noise coming from the sensors is determined by the accuracy of the sensor set. To perform a representative analysis, the simulated noise is based on the sensor set of the GEnx-1B engine. The GEnx-1B engine sensor set with its corresponding accuracy is displayed in Table 4.3. To simulate the accuracy of the sensors, a probability density function is constructed for every measurement. The standard deviation is chosen such that 2σ equals the accuracy of the sensor. This means that approximately 95.5% of the simulated noise falls within the sensors specified accuracy.

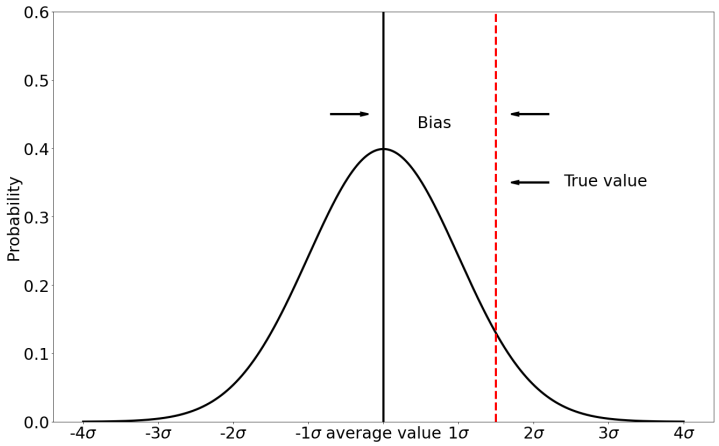

Figure 4.8: Probability density function

The bias of the sensor set is unknown, which can influence the results of the algorithm. However, if the relationships are created for the same engine that is to be trended, this does not pose a large problem. This is caused by the fact that the bias of the sensors is constant. Therefore, the bias is excluded from this analysis and only the noise is simulated.

Sensor	Accuracy	Units
N1,N2	±0.12	RPM
W_f	±3.5% of measurement	pph
$T_{t,12}, T_{t,25}, T_{t,3}, T_{t,49}$	±0.4% of measurement	$°C$
$P_{t,2}$	±0.01	psia
$P_{s,3}$	±0.36	psia

Table 4.3: Accuracy of sensor set GEnx-1B engine [9, 10]

Results noisy data

In Appendix C in Figure C.2, the results from the algorithm on noisy data are displayed. The algorithm is capable of reproducing the three flow capacity ΔW_C relationships very accurately. Also, the HPT $\Delta\eta$ curve is corresponding with the simulated relationship. Again, the $\Delta\eta$ relationships for the LPT and HPC are not accurate. This is caused by smearing, leading to an overestimation of the LPT efficiency and underestimation of the HPC efficiency. The noise does not seem to affect the relationships when compared to the non-noisy data.

Optimiser results

The optimiser results are given in Appendix C in Figure C.3. The rms_{OP} value is a factor 10 higher compared to the rms_{OP} from the noise-free analysis. This is caused by the noise itself, inherently causing a deviation between the model and the measurement points. Since the generated curves show the same shape as the simulated curves, the algorithm is deemed capable of working with noisy data. This is also represented by the rms_{curves} which is 0.0212, which is even lower than the non-noisy case.

4.5. Algorithm settings

The former section has shown that the algorithm is capable of identifying simulated SPP effects. Now it is interesting to see what the influence of the algorithm settings is on the results. In this section, the conclusions from a sensitivity analysis on the algorithm settings are displayed. Subsequently, the effect of varying the algorithm bounds is identified.

4.5.1. Differential algorithm settings

As indicated, the algorithm features parameters that can be tuned to the specific application. The settings that can be varied are the population size NP, maximum iterations Q, crossover constant CR, the amplification factor F and the number of evaluated operating points OP. To indicate the effect of varying the algorithm settings, a sensitivity analysis is performed. In this analysis, one algorithm parameter is changed, and the other parameters are kept constant. The whole sensitivity analysis, including all the parameter definitions, is displayed in Appendix D. The conclusion from the analysis is displayed below. The algorithm settings that will be used are:

- CR=0.5
- F=[0.5,1]
- Q=10
- OP=30
- NP=5

These parameters are chosen because of the criteria of limited running time and optimal rms_{curves}.

4.5.2. Bounding algorithm

The performance deviation coefficients from the algorithm can also be bounded. Since information is known from literature, the bounds can be chosen in a way that the flow capacity and the efficiency are increased or decreased in line with what to expect from the secondary performance parameter. In the former sections, this is done such that the efficiency coefficients are positive $\in [0,12]$ and the mass flow coefficients are negative $\in [-12,0]$. In this section, the effect of enlarging the bounds is explored. Both the flow capacity as the efficiency performance deviation coefficient bounds are taken as $\in [-12,12]$. The results from the broader bounds are given in Appendix C in Figure C.4 and Figure C.5. This analysis indicates that some coefficients are negative instead of positive. However, this does not result in wrong relationships as is displayed in Figure C.4. Due to the parametrisation, some curves are only concave instead of convex. The rms_{curves} is 0.0319, which is in the same order as the unbounded runs. Therefore, unbounding the algorithm does not have a major impact on the results of the algorithm.

4.6. Conclusions methodology

From the proof of concept can be concluded that:

- The algorithm is capable of identifying relationships between SPPs and performance deviations.
- Reducing the number of measurements increases the chance of smearing.
- The algorithm is capable of working with noisy data.
- A low rms_{OP} does not necessarily mean a low rms_{curves}, due to smearing effects.
- Broader bounds do not drastically decrease the algorithms ability to re-create the simulated relationships.

It is concluded that the algorithm can be used on the GEnx-1B case study to identify the SPP effects. The next chapter will introduce this case study.

III

Case study

5

Preparation case study GEnx-1B engine

This chapter provides the preparation to apply the methodology from Part II on the GEnx-1B case study. This chapter is divided into 6 sections. The first section introduces the GEnx-1B engine and the research hypothesis. The second section presents the available data and displays the corrected rotational spool speeds at take-off and cruise. The third section introduces the secondary performance parameters. The fourth section introduces the bounding of the algorithm. The fifth section explains the reference engine selection. In the last section, the current GEnx-1B model is presented.

5.1. GEnx-1B engine

For this case study, the GEnx-1B engine is used. This is a high-bypass ratio double spool turbofan engine that is used to power the Boeing-787 Dreamliner. The GEnx-1B has an overall pressure ratio of 46.3, and a bypass ratio of 9.1 at take-off. It features highly curved composite fan blades to reduce the weight and increase the efficiency by 15% with respect to its predecessor, the GE CF-6 [8].

The engine is displayed in Figure 5.1 with the corresponding station numbers specified in Table 5.1. This follows the standard ARP engine station numbering and nomenclature [58]. KLM operates this engine on its Boeing 787-9 aircraft, hence sensor data is available from the operation of the GEnx-1B. Moorselaar [50] created an engine model for the GEnx-1B in order to perform GPA. This engine model has the take-off power setting as the design point and is capable of representing the measurements at this power setting with good accuracy. When this engine model is used for cruise conditions, the output deviates from the engine measurements. The hypothesis in this thesis is:

> *The modelling error for the cruise power setting can be reduced by accounting for the secondary performance parameters with relationships determined by an evolutionary algorithm.*

To assess the validity of this hypothesis, the following sections will further introduce the case study. First, the available data is introduced.

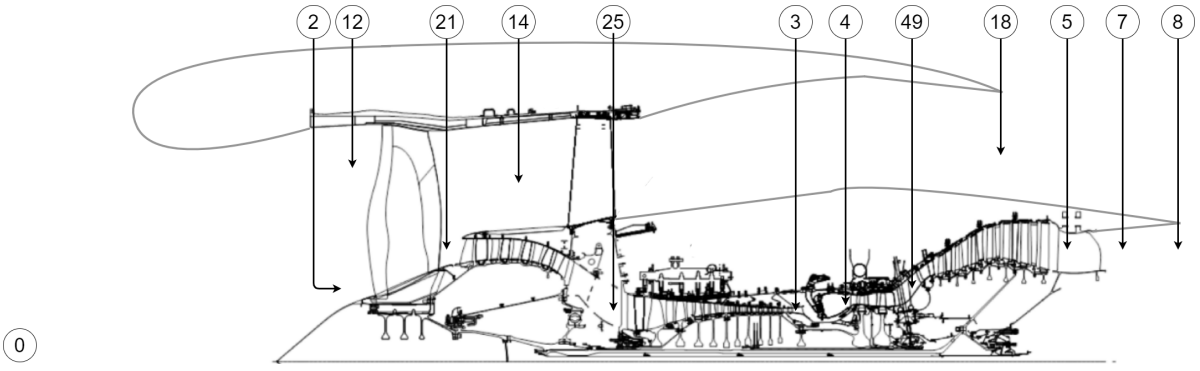

Figure 5.1: GEnx-1B station numbering [9]

Station number	Station	Station number	Station
2	Fan hub inlet	4	Combustor outlet
12	Fan tip inlet	49	HPT outlet
21	LPC inlet	18	Bypass Nozzle throat
14	Bypass stream	5	LPT outlet
25	HPC inlet	7	Core nozzle inlet
3	HPC outlet	8	Core nozzle throat

Table 5.1: Standard ARP engine station numbering [58]

5.2. On-wing data

On-wing data from the GEnx-1B engine is available to KLM as continuous engine operating data (CEOD). This section introduces the data format, as well as the GEnx-1B corrected spool speeds during operation.

5.2.1. Continuous engine operating data

Modern gas turbines have a reduced number of gas path sensors compared to their predecessors. For the GEnx-1B, multiple pressure and temperature measurements are missing throughout the engine, which makes gas path analysis more complicated. To compensate for these missing sensors, CEOD is introduced. CEOD is one of the improvements that came with the introduction of the GEnx-1B engine. CEOD constantly captures the value of over 300 parameters stemming from the GEnx-1B engine [2]. In addition to the gas path sensors, the CEOD contains information about the secondary performance parameters. The CEOD parameters are visible in Table 5.2. These require some introduction. The primary parameters are the gas path sensors. They display the pressures, temperatures, rotational speeds, and fuel flow. The secondary performance parameters display the setting for the bleed flow valves, Total Engine Horsepower extraction (power off-take), variable geometry and information about the active clearance control and clearances in the turbines. In former performed research at KLM, the variation of these parameters have not been included in the GEnx-1B GSP model. Since these parameters influence the performance characteristics of the engine, the CEOD is of great value for accurate GPA. The following section will display the operational corrected spool speeds of the GEnx-1B engine after which the data from the secondary performance parameters is introduced. Information on the data pre-processing and the input from this data to GSP is available in Appendix E.

5.2.2. GEnx-1B corrected spool speeds

The corrected rotational speeds disclose much about the operation of the GEnx-1B engine. They are displayed for both the N_1 as the N_2 spool in Figure 5.2a and Figure 5.2b respectively. As is clear, the corrected N_1 rotational speed at cruise is similar to the rotational speed at take-off. The corrected rotational speeds of the corrected N_2 spool are higher at cruise compared to take-off.

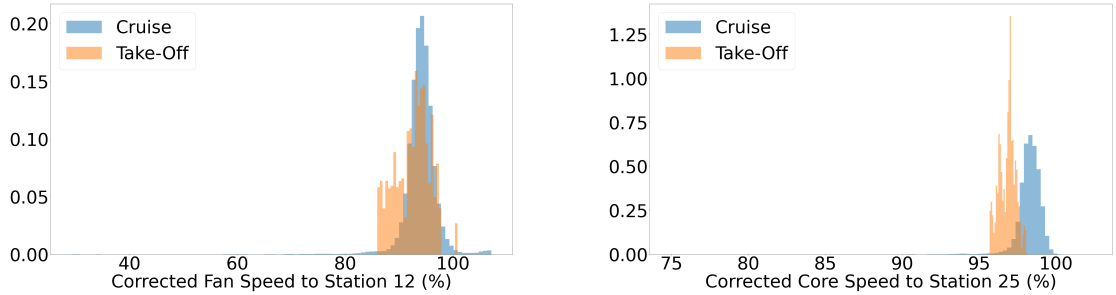

(a) Corrected fan speed

(b) Corrected core speed

Figure 5.2: GEnx-1B corrected spool speeds

Table 5.2: CEOD data parameters GEnx [9]

Parameter	description	Unit	Refresh rate
$T_{t,2}$	Total fan inlet temperature	[°C]	60ms
$T_{t,25}$	Total HPC inlet temperature	[°C]	60ms
$T_{t,3}$	Total HPC outlet temperature	[°C]	60ms
$T_{t,49}$	Exhaust gas temperature	[°C]	60ms
$P_{t,2}$	Total fan inlet pressure	[psia]	60ms
$P_{S,3}$	Static HPC outlet pressure	[psia]	60ms
N_1	Fan rotational speed	[rpm]	60ms
N_2	Core rotational speed	[rpm]	60ms
W_f	Fuel mass flow	[pph]	60ms
$HPTACCV_{pos}$	Selected HP Turbine Active Clearance Control Valve Position	[%]	60ms
$LPTACCV_{pos}$	Selected LP Turbine Active Clearance Control Valve Position	[%]	60ms
$CCCV_{pos}$	Selected Core Compartment Cooling Valve Position	[%]	60ms
VBV_{pos}	Selected Variable Bleed Valve Position	[%]	60ms
TBV_{pos}	Selected Transient Bleed Valve Position	[%]	60ms
VSV_{pos}	Selected Stator Vane Position	[%]	60ms
PTO	Total Engine Horsepower Extraction	[hp]	960ms
BAI_{pos}	Selected BAI(Booster Anti-Ice) Bleed Valve	[-]	60ms
W_{25}	Calculated core airflow	[pps]	60ms
$\Delta N2$	Core speed rate of change	[% N2/s]	60ms
AHPTC	Actual HP Turbine Clearance (calculated)	[in]	60ms

5.3. Secondary performance parameters

The additional information in the CEOD can be used to improve the accuracy of the GSP model. In this section, the additional information from the secondary performance parameters is introduced, after which the patterns in the data are explained. This is done by displaying the SPP settings for the take-off and cruise operating point in normalised histograms. Subsequently, the parameterisation method of the SPPs is explained that will be used in the algorithm. This is done for every secondary performance parameter. First, the bleed flows are treated, after which the power off-take, active clearance control for the turbines and variable geometry are discussed.

5.3.1. Bleed Flows

The GEnx-1B also incorporates bleed flows. Bleed flows subtract air from the core flow to be put to use in secondary systems or to improve the surge margin of the compressor. In the GEnx-1B engine, four sets of bleed valves are present. The variable bleed valves (VBV), transient bleed valves (TBV), booster-anti ice bleed (BAI) and the cowling anti-ice bleeds (CAI). From the VBVs and the TBVs, the valve positions are known but are only opened at firing up the engine or in rare cases during cruise. Since these cases are easily filtered out, the choice is made not to consider them in the algorithm.

The booster-anti ice bleeds retract air from the 7th stage of the HPC. This air is used to heat the booster for anti-ice purposes. A maximum value of 2% of the core flow is extracted. The CEOD data contains two metrics regarding this setting. One value gives the operating mode indicating on or off. The other value gives the pressure in the duct leading to the booster. This pressure is used by the EEC to estimate the amount of bleed that is extracted. From this information, it is visible that the pressure in the duct only spikes at limited moments, meaning the valve is mostly closed. Therefore it is filtered out and also not used in the analysis.

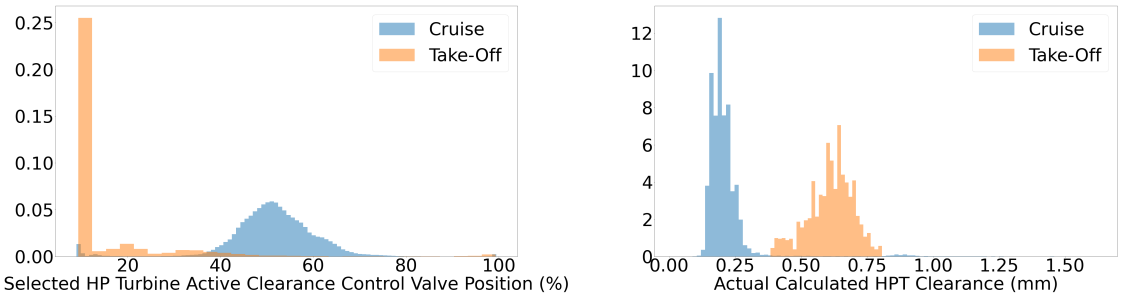

(a) HPTACC valve position at cruise and take-off

(b) HPT actual clearance at cruise and take-off

Figure 5.3: Data on HPT active clearance control

The CAI can subtract up to 3.3% of the total core flow at stage 7. The bleed setting is given in values 0, 1 or 2. At KLM no information is available on the specific meaning of these settings. During cruise, it is assumed to be turned off due to the low humidity at that altitude. For model development, data was used in which the bleeds were also assumed to be turned off [50]. Therefore, it is not considered for adapting the model.

5.3.2. Power off-take

The electric system for the cabin air and other auxiliary components of the aircraft needs a power source. The required power is subtracted from the N2 shaft by the Variable Frequency Starter Generators(VFSG) with an assumed efficiency of 92.8%. The horsepower extraction is given in the CEOD. This information is used in the GSP model to simulate the load on the N_2 spool. This is implemented in all engine models used in the case study.

5.3.3. Active clearance control

In the GEnx-1B engine, the high pressure turbine active clearance control valve (HPTACCV) and low pressure turbine active clearance control valve (LPTACCV) regulate the clearance between the casing and rotor blades for reasons mentioned in section 3.3. By using thermal control, the clearance can be kept at an optimal value. The HPTACCV and LPTACCV control these systems for the HPT and LPT. These valves are controlled by the EEC. Their positions are specified in percentages. For the HPT, GE also provides a calculated clearance (AHPTC). To understand how GE designed the GEnx-1B engine, it is interesting to analyse the behaviour of these SPPs in various conditions. First, the HPTACC is analysed, after which the LPTACC is treated. Besides the HPTACC and the LPTACC, the core compartment cooling valve (CCCV) regulates the air to cool the under-cowl environment. In contrast to the LPTACCV and HPTACCV, the valve setting is only known in open or closed conditions. This flow leaves the engine through the core engine vent. The influence of the CCC is not expected to be as influential since it does not change the tip clearances. Therefore, it will not be further treated.

Data patterns HPTACC

The HPTACC is designed to increase the efficiency of the turbines. How this system operates is different for various operating conditions. Multiple interesting relations can be found in the flight data. The first relation is found between the HPTACCV and the operating condition. This is visualised in Figure 5.3a. As is visible, the valve is opened further at cruise condition. In search of a pattern of the valve position with another parameter, no unambiguous relation was found, although it is clear that it reacts on the N_2 spool speed, $T_{t,49}$ and the ambient temperature. This is also logical because the air temperatures influence the expansion of the blade and casing, and the rotational speed influences the blade length. Therefore, it seems that GE uses a multivariable control system to steer the valve position.

Since the actual calculated HPT clearance is also available, it is possible to visualise the resulting difference in clearance at take-off and cruise. Figure 5.3b shows the calculated clearance at cruise and take-off. As is visible, the clearance at take-off is kept higher, which will probably result in a lower HPT efficiency. This is likely done to avoid the risk of abrasion in the transient condition during take-off.

Data patterns LPTACC

The LPTACC control valve position has no complicated control system. The LPTACC control valve position has a clear relation with the operating condition. This relation is visualised in Figure 5.4a. This figure displays the relation between the LPTACC valve position and the altitude. At higher altitudes, the valve is more open. This distinct pattern is also visible in Figure 5.4b, which displays the normalised histogram of the LPTACC valve positions in multiple flights. The blue pillars represent the various cruise altitudes.

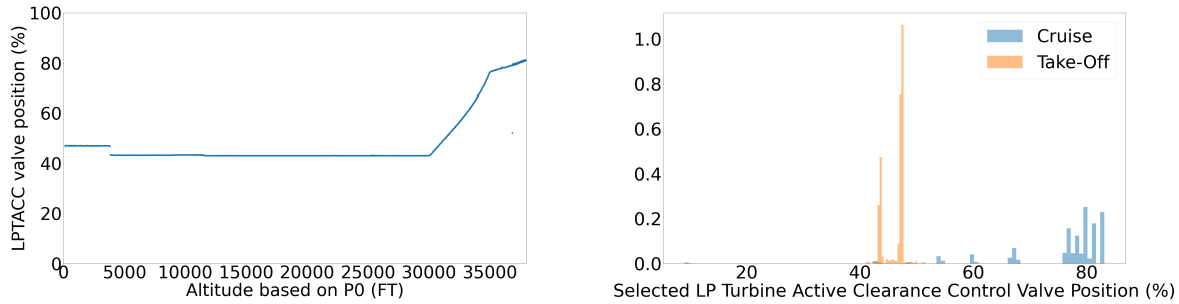

(a) LPTACC valve position versus altitude

(b) LPT actual clearance at cruise and take-off

Figure 5.4: Data on LPT active clearance control

Parametrisation of the active clearance control

To compensate for the effect of the active clearance control, this additional data is used as independent variables in the algorithm. For the compensation of the clearance of the HPT, the actual calculated clearance is used. This variable has the most direct relationship with the HPT performance since the performance is dependent on the clearance. For the LPT, the ACCLPT valve position is used, as no more accurate variable is available. Since the ACCLPT valve position varies with altitude, the algorithm will indirectly compensate for altitude. Since the direct relation between the ACCLPT valve condition and the actual clearance is unknown, no direct relation will be constructed between the clearance and the performance deviation. This limits the possibility to compare the performance increase with literature. However, it still enables the algorithm to find a relation between the operating condition and the LPT performance. For both the AHPTC as well as the LPTACC valve position, the difference between the average value at take-off and the value at cruise is taken as the independent variable for the algorithm.

5.3.4. Variable geometry

The Variable Stator Vanes (VSV) and Inlet Guide Vanes (IGV) assure stable operation in off-design conditions. They prevent surging of the compressor by changing their angle relative to the flow. In the GEnx-1B engine, these are present as IGVs at the HPC inlet and stages 1-4 VSVs in the HPC. Their position is determined by the EEC and it is given in percentage. They are actuated by the same lever arm, this means that their position relative to each other is scheduled. The schedule of the VSVs and IGVs is given in Figure 5.5. A higher percentage means that the VSVs/IGVs are more open. As is visible, the VSV/IGV position is a function of corrected core speed and the flight altitude. The points on the top left with the higher VSV/IGV position represent the take-off condition and the region in which the aircraft climbs at cruise altitude. It is clear that these operating modes are not identical to the steady-state cruise operating mode.

Therefore, the relationships from the algorithm should be able to account for this difference.

Parametrisation of variable geometry

The two parameters that seem to determine the VSV/IGV position are the corrected core speed and the altitude. The relation with corrected core speed is mapped in the compressor maps of the model, but the relation with the altitude is not. Since the relation with the corrected core speed is mapped in the compressor map, the algorithm should only compensate for the difference in VSV/IGV position versus the altitude. Therefore the performance deviations are dependent on the deviation of VSV/IGV angle between the design point of the model and the cruise operating point, which is in turn dependent on altitude.

To summarise, the variable geometry and active clearance control are parameterised for the algorithm by the following parameters:

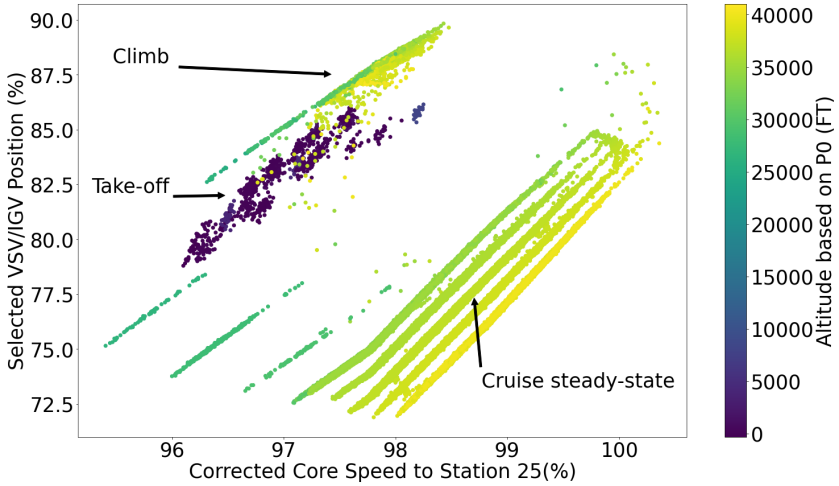

Figure 5.5: VSV/IGV position versus the corrected core speed and altitude

- HPC variable geometry is parameterised as the VSV/IGV position which has a relationship with the flight altitude.
- HPT clearance is parametrised as the actual calculated HPT clearance.
- LPT clearance is parameterised by the ACCHPT valve position.

The power off-take is simulated directly into GSP, and the bleed flows are not considered because not enough data is available.

5.4. Bounding the algorithm

With the parametrisation in place, this section defines the bounds for the algorithm. Since the effect of these secondary performance parameters should fall within a certain limit, the algorithm is bound. The bounds are defined as a maximum and minimum performance deviation for the most deviating SPP setting. They are displayed in Table 5.3. By keeping the bounds large, it is possible for the algorithm to determine relationships that contradict the expected effect of the secondary performance parameters. If the algorithm is capable of finding patterns that comply with the literature, this would be a successful result.

SPP	Upper bound performance deviation[%]	Lower bound performance deviation [%]
HPC VSV/IGV ΔW_c	4	-20
HPC VSV/IGV $\Delta\eta$	3.5	-2
HPT clearance ΔW_c	2	-3.5
HPT clearance $\Delta\eta$	3.5	-2
ACCLPT valve position ΔW_c	2	-3.5
ACCLPT valve position $\Delta\eta$	3.5	-2

Table 5.3: Bounds for the algorithm

5.5. Engine selection

With the data pre-processing in order, a reference engine should be selected to run the algorithm on. KLM operates multiple Boeing 787-9 aircraft, meaning a choice can be made on which engine to use. For model creation, a well-performing engine should be used, since the deterioration should be determined with respect to a 'new' engine.

Which engine to choose is based on the exhaust gas temperature margin hot day (EGTMHD), which is a good indicator of engine state. Also, the algorithm is run on CEOD. Therefore, it is important that CEOD is available for that particular motor. The CEOD becomes available for KLM after a certain number of cycles (the number of cycles can not be disclosed due to confidentiality). This poses a problem because the engines do not perform as well as an engine in 'new' state after that certain amount of cycles. However, one GEnx-1B engine suffered from an HPT blade burndown. This resulted in the need for a full overhaul of the engine and restoring good engine performance. The CEOD from re-entry of service is available for KLM. Therefore, this engine is chosen as reference engine and based on the data from this engine, the algorithm will produce relationships to account for the secondary performance parameters. Due to confidentiality, the engine serial number (ESN) can not be disclosed. It will be referred to as ESN956XXXA.

To test if the determined relationships also work on other engines, multiple engines are selected that feature approximately the same EGTMHD as the ESN956XXXA. These engines will be referred to as ESN956XXXB to ESN956XXXF. For illustration, the EGTMHD for both ESN956XXXA and ESN956XXXB is displayed in Figure 5.6. The two vertical lines indicate the time period from which the CEOD data is gathered. For the ESN956XXXA, it is clear that the period is just after the long overhaul. The jumps in the EGTMHD are caused by the water washes. In the next section, an analysis is performed on the data from ESN956XXXA, to indicate the performance of the current GEnx-1B model.

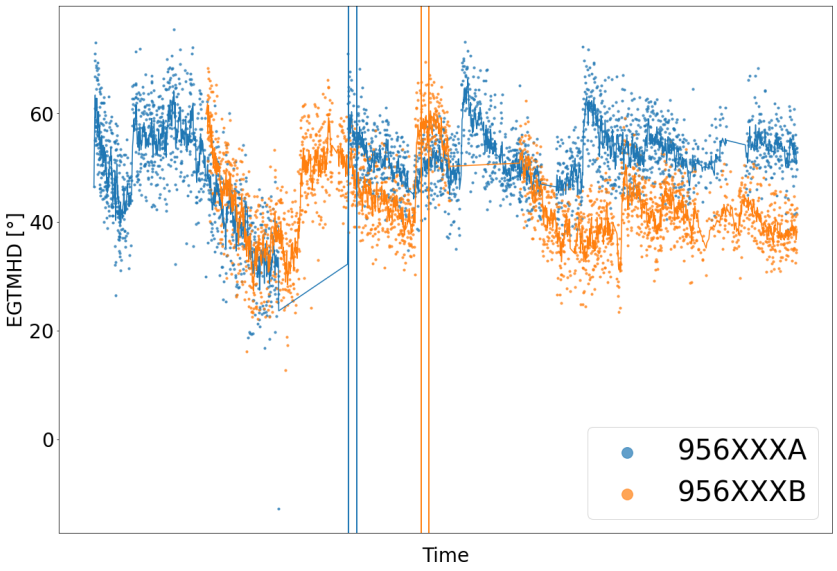

Figure 5.6: EGTMHD for the reference engines

5.6. Current state GEnx-1B model

The current GEnx-1B model developed by Moorselaar [50] accurately represents the take-off operating condition. The model reference point is based on the take-off condition and calibrated with test cell data. The component maps are tuned with on-wing take-off data. In this section, the baseline model is introduced as well as an improved model with a modified LPC and fan component. For both models, the level of accuracy will be introduced.

5.6.1. Baseline model

The baseline model shows a good average representation of the take-off condition measurements. In Table 5.4 the performance is set out. A negative value means that the model overestimates the parameter value. Both for cruise and take-off conditions, the average error for the various measurements is displayed. Also, the standard deviation of the error is shown. This metric is important because it indicates the spread of the error. The spread of the error indicates effects that are not modelled. Since the secondary performance parameters are currently not accounted for, this parameter is important to evaluate the results of the algorithm.

To come to these values, the model was run for 100 take-off and cruise on-wing operating points from the time periods mentioned in section 5.5. Afterwards, the output data was compared to the on-wing measure-

ments. As is clear, the cruise operating point is drastically less accurate.

To compensate for the secondary performance parameter effects, the algorithm is run in section 6.1. However, based on the results from section 6.1, it was identified that the secondary performance parameters are not the only factor that causes the deviation between the cruise and take-off deviation.

Therefore, the need for an improved model was identified to display the capabilities of the algorithm. This improved model is needed since the baseline model deviates too much from the on-wing data with regards to the fan and LPC from now on referred to as low pressure system (LPS). This model will be introduced in the following section.

Measurement	Avg error at cruise[%]	$\sigma_{error\ cruise}$	Avg error at take-off[%]	$\sigma_{error\ take-off}$
N_2	1.40	0.52	-0.19	0.18
W_f	-15.25	1.42	-1.45	1.18
$T_{t,25}$	1.21	0.56	0.52	0.36
$T_{t,3}$	-1.59	0.81	-0.76	0.87
$T_{t,49}$	-8.93	1.13	0.21	0.71
$P_{s,3}$	-4.53	0.79	-0.88	0.47

Table 5.4: Baseline model accuracy

5.6.2. Improved GEnx-1B model with adjusted low pressure system

The results from section 6.1 will indicate the need for an adapted model because the deviation can not fully be decreased by accounting for the secondary performance parameters. This improved model contains a modifier for the fan and the low pressure compressor mass flow capacity and efficiency.

The ΔW_c for the fan and LPC are -3 and -1, respectively. The $\Delta\eta$ modifiers for the fan and LPC are 3.8 and 2.8. This choice is made because the cruise operating point in the fan and LPC map does not change appropriately compared to what is expected at cruise conditions. At cruise the LPC and fan efficiency is reduced severely, causing the measurement deviations that are displayed in Table 5.4. Therefore the efficiency of the fan is increased up to the design efficiency to compensate for the wrong operating region. Also, the mass flow capacity is adapted such that the error in $T_{t,25}$ is reduced.

The deviations of the improved model with the adapted low pressure system are displayed in Table 5.5. Again, a negative value means that the model overestimates the parameter value. To be able to analyse the results, the specifics of the model components are given in the following section, after which a sensitivity analysis is performed.

Measurement	Avg error at cruise[%]	$\sigma_{error\ cruise}$
N_2	2.73	0.30
W_f	-2.67	1.51
$T_{t,25}$	-0.93	0.43
$T_{t,3}$	0.71	0.32
$T_{t,49}$	-3.91	0.68
$P_{s,3}$	1.89	0.94

Table 5.5: Accuracy of improved GEnx-1B model with adapted low pressure system

5.6.3. Analysis GEnx-1B model

For a proper evaluation of the results, it is important to know the specifics of the current models. As explained, off-design GPA relies on component maps to specify component performance. This section will display the

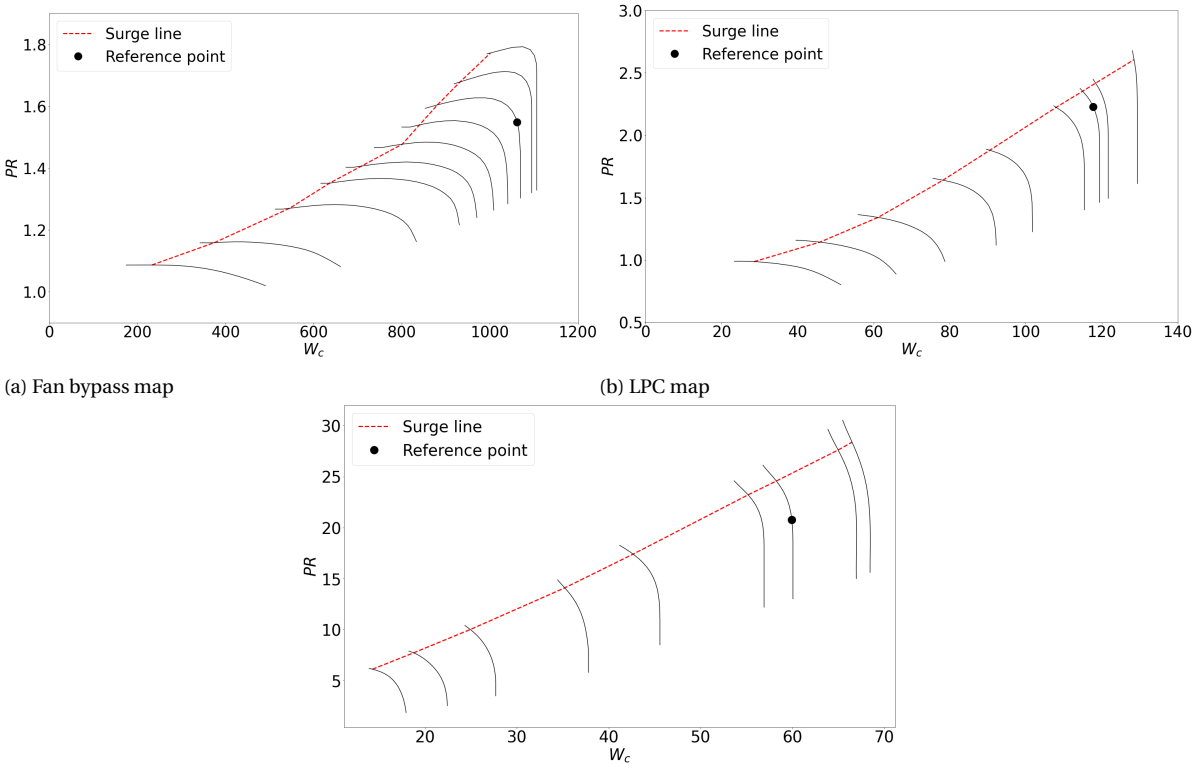

(a) Fan bypass map

(b) LPC map

(c) HPC map

Figure 5.7: Compressor maps GEnx-1B model

component maps used in the models in combination with the reference points used in the model. Also, the reference point nozzle information is displayed.

Compressor maps
In the GEnx-1B models, three compressor maps are present. The first map is the fan bypass map displayed in Figure 5.7a. The black point denotes the reference point of the model. In the case of the GEnx-1B model, this is the take-off point. In the current models, the reference point is chosen with a large surge margin. The second map is the LPC map. This map is used for simulating the fan core and the booster. This is possible because they are connected to the same axis. For the fan core map, a smaller surge margin is chosen as reference point. The same holds for the HPC map. The design efficiencies of the fan bypass, LPC and HPC are 0.92 0.90 and 0.87, respectively. This information will be used to interpret the results.

Turbine maps
The turbine maps are less complicated because the turbines mostly operate in one operating point since their design operating point is located in the choking condition. Therefore, their operating efficiency is 0.93 and 0.94 for the HPT and LPT, respectively, which does not change much under the influence of different operating conditions.

Nozzle design parameters
The nozzle Mach numbers at take-off condition are 0.74 and 0.87 for the bypass and core nozzle, respectively. The nozzle velocity coefficients are 0.915 and 0.9 for the bypass and core nozzle, respectively.

5.6.4. Sensitivity analysis GEnx-1B model
To indicate the effect of certain component performance deviations on the measured parameters, a sensitivity analysis is performed on the GEnx-1B engine baseline model. The results from the improved model are approximately the same. Hence, they are not given.

The results are displayed in Figure 5.8. On the x-axis, the performance deviations are displayed, which are increased by 1%. On the y-axis, the difference in model output value is displayed where a positive value

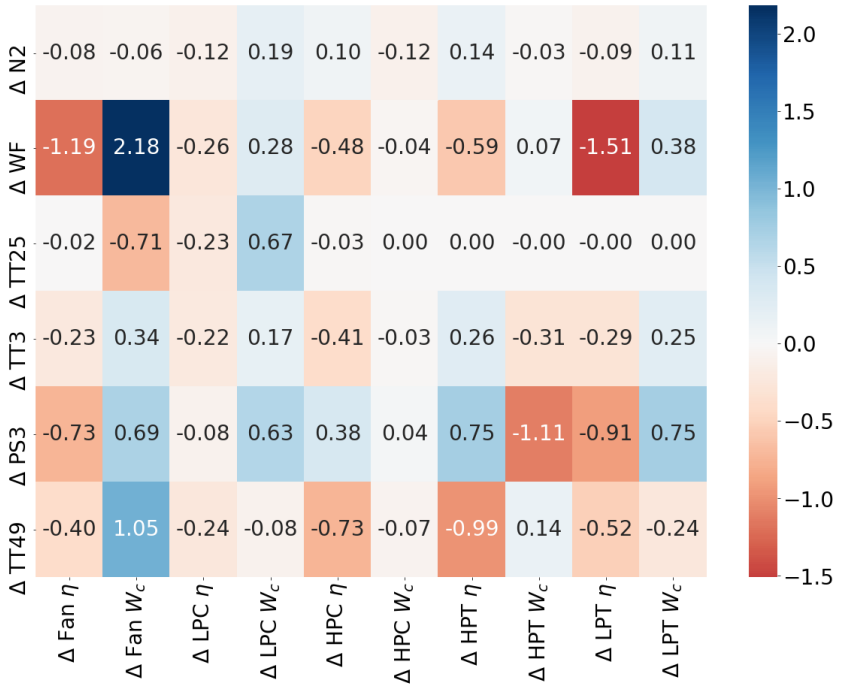

Figure 5.8: Sensitivity analysis GEnx-1B engine

indicates that the model output was increased. This gives valuable insight into the behaviour of the model, and can be used to interpret results. As is clear, the engine follows standard deterioration behaviour for a twin spool turbofan. The following chapter will display the results of the case study.

6

Results case study on GEnx-1B engine

In this chapter, the algorithm is run on the on-wing cruise data from the ESN956XXXA engine. As mentioned, the secondary performance parameters that are included are the power off-take, HPC variable geometry, HPTACC and LPTACC. The power off-take is modelled directly into GSP, and therefore not further treated. The HPC variable geometry, HPTACC and LPTACC are compensated for by the algorithm. The following section will introduce the results from the algorithm on both models. First, the results achieved by the algorithm on the baseline model will be displayed and discussed. Subsequently, the results from the algorithm on the improved model are evaluated. Finally, the determined relationships will be used on datasets from other GEnx-1B engines.

6.1. Results algorithm on baseline model

In this section, the algorithm is run on the baseline model. First, the accuracy increase achieved with the determined relationships is introduced, after which the effect of the individual secondary performance parameters is discussed.

6.1.1. Accuracy increase

In Figure 6.1, the results from the algorithm in terms of accuracy increase are displayed. The blue columns denote the deviation between the current baseline GEnx-1B model output and the GEnx-1B cruise measurement data. The orange columns display the results when the determined relationships from the algorithm are used to account for the active clearance control and the variable geometry. Figure 6.2 shows 300 measurement points and their individual deviation from the model output. In both these graphs, a negative value means that the model output is higher than the on-wing measurement. These measurements are taken from the ESN956XXXA engine dataset during the time period indicated in section 5.5.

Absolute deviation

The absolute deviation between the model and the on-wing cruise data is decreased by the determined relationships from the algorithm. However, the difference is not decreased towards zero percentage. The $T_{t,49}$ and W_f deviations are decreased by the largest amount. The deviation in N_2, $T_{t,25}$ and $P_{s,3}$ is not decreased by a large margin.

To understand why this is happening, it is useful to recall how the objective function was defined. It is defined as the root mean square of the deviation between the model output and the on-wing data. As the initial deviations for the $T_{t,49}$ and W_f are the largest, the lowest objective function value is achieved by driving these errors down by a large margin. This can come at the cost of the other parameters. Therefore, the rest of the deviations is not decreased by a large margin.

As will become apparent in the following section, the determined relationships for efficiency are all approximately against the bounds towards enhancing the performance of the component, resulting in unrealistic high efficiencies.

This indicates that the engines mass flow and efficiencies of the fan and the LPC (the low pressure system LPS) at cruise conditions are not correct. The too-high fuel mass flow can be caused by the fact that the model

has to use to much power to rotate the N_1 spool at a certain rotational speed. This can also cause the $P_{s,3}$ value to be overestimated by the model, because the N_2 axis also has to account for this additional required power.

The algorithm compensates for the suspected incorrect mass flows and wrong LPS efficiencies with the relationships, as will be apparent from the results of the individual relationships. What is also interesting to see is that $T_{t,25}$ is barely influenced by the relationships. This is supported by the sensitivity analysis from subsection 5.6.4 and is a consequence of the fact that no upstream influence is present in the model. The N_1 rotational speed is the controlled parameter in the model. As $T_{t,25}$ is the temperature measurement downstream of the LPC, and the combination of the fan and LPC performance determine the LPC operating point, this value is dependent on the performance of the fan and LPC.

Since none of the SPPs affect the LPC or the fan, $T_{t,25}$ is barely influenced.

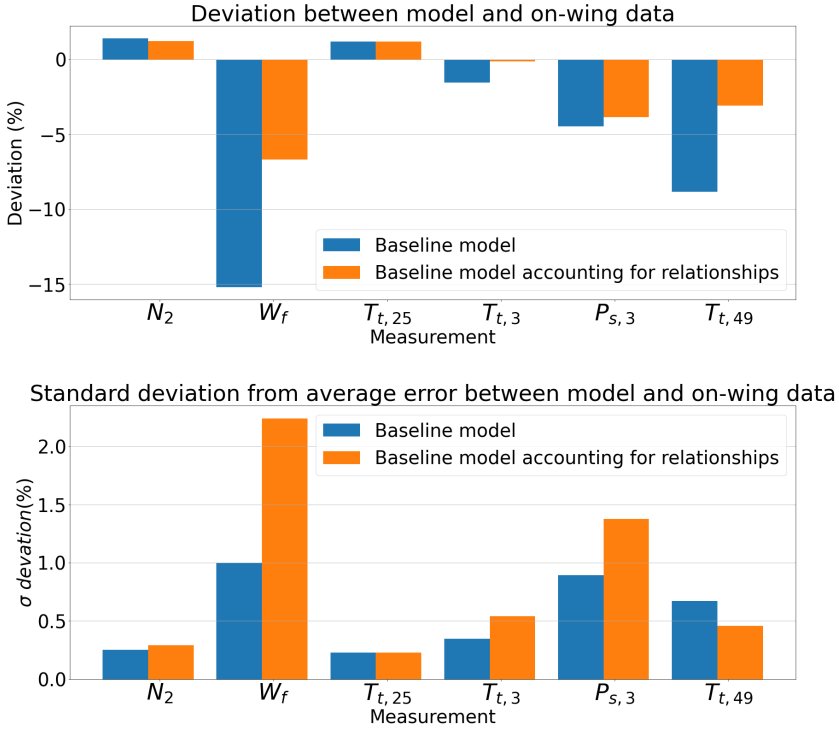

Figure 6.1: Algorithm deviation results between model output and on-wing measurements for standard GEnx-1B model

Standard deviation of error

The standard deviation of the error is an important parameter to judge the working of the algorithm. Since the setting of the secondary performance parameter determines the performance deviation of the component, only a difference in SPP setting can change the component performance. So if the standard deviation of the error is decreased, a certain degree of uncertainty is taken away from the model that was caused by the secondary performance parameter. As can be seen from Figure 6.1, the standard deviation of the error between the model and the on-wing data points is increased drastically. This is also shown in Figure 6.2. This is caused by the fact that the algorithm needs to compensate for too-large differences causing the algorithm to approach the bounds of the coefficients. This will further be elaborated on in the following sections. Again, only $T_{t,25}$ is not influenced by the algorithm.

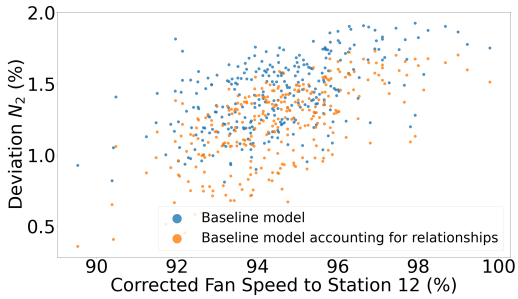

(a) N_2 deviation from baseline GEnx-1B model accounting and not accounting for relationships

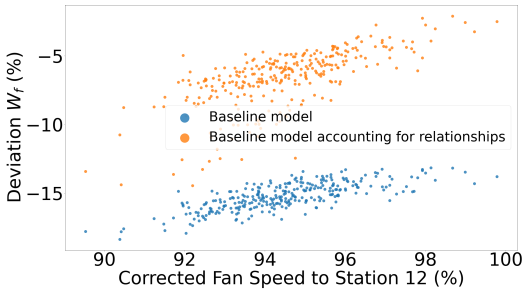

(b) W_f deviation from baseline GEnx-1B model accounting and not accounting for relationships

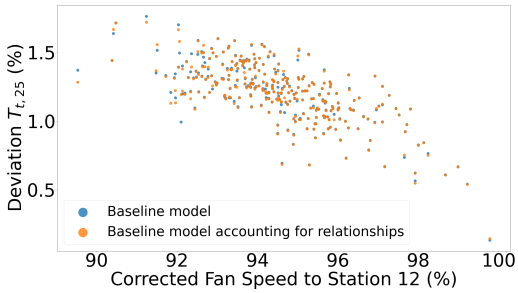

(c) $T_{t,25}$ deviation from baseline GEnx-1B model accounting and not accounting for relationships

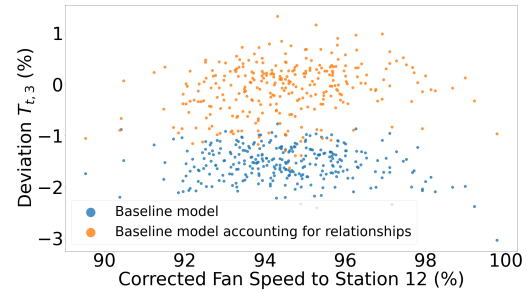

(d) $T_{t,3}$ deviation from baseline GEnx-1B model accounting and not accounting for relationships

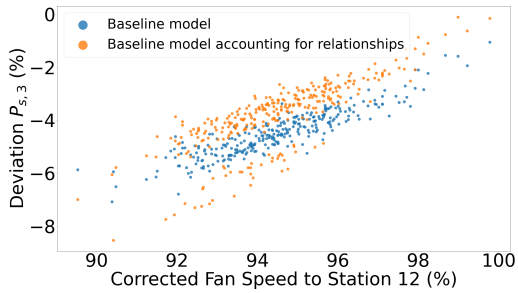

(e) $P_{s,3}$ deviation from baseline GEnx-1B model accounting and not accounting for relationships

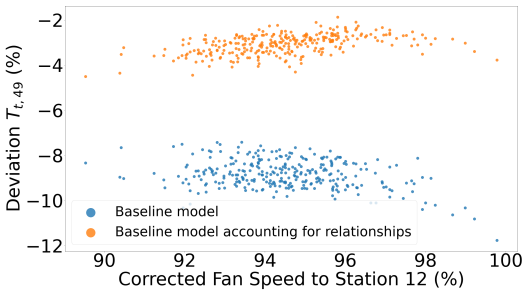

(f) $T_{t,49}$ deviation from standard GEnx-1B model accounting and not accounting for relationships

Figure 6.2: Deviation of parameters for baseline GEnx-1B model accounting and not accounting for relationships

6.1.2. Individual relationships

In this section, the resulting relationships are displayed. This is done by displaying the difference between take-off and cruise in SPP setting on the x-axis and the corresponding performance deviation on the y-axis. First, the HPC variable geometry relationships are displayed, after which the active clearance control for the HPT and LPT are treated.

HPC variable geometry

In Figure 6.3, the performance deviations based on the VSV/IGV position setting are set out. The x-axis displays the difference between the VSV/IGV setting at cruise (OD) versus the setting at take-off (DP). The VSV/IGV position is opening more along the x-axis. The y-axis displays the performance deviation that is used in the algorithm based on the SPP setting. Figure 6.3c displays the deviation between the model output and the on-wing data versus the altitude, which determines the VSV/IGV angle deviation.

At cruise, the VSVs/IGVs are more closed compared to take-off. The curves found by the algorithm indicate that the efficiency goes up based on the VSV/IGV difference. Also, the mass flow capacity goes down with closing the vanes. This is in line with what is expected, as described in Figure 3.3.1. Since the same power output is still required to maintain a certain N_1 speed, the N_2 spool speed will increase. This is also

displayed by the slightly decreasing N_2 deviation in Figure 6.1. The efficiency is increased to compensate for the operating point shifting to an area of lower efficiency. However, from Figure 6.3c can be seen that the dependency of the N_2 deviation on the altitude and is not decreased. As the altitude determines the VSV/IGV angle deviation between cruise and take-off, the algorithm should erase this dependency.

As explained in the former section, the algorithm can decrease the objective function more by decreasing the W_f and the $T_{t,49}$ deviation. This is also indicated by the magnitude of the flow capacity modifier for the closing of the VSVs/IGVs, which is low. Therefore, the algorithm did not adapt the dependency of the N_2 deviation on the altitude.

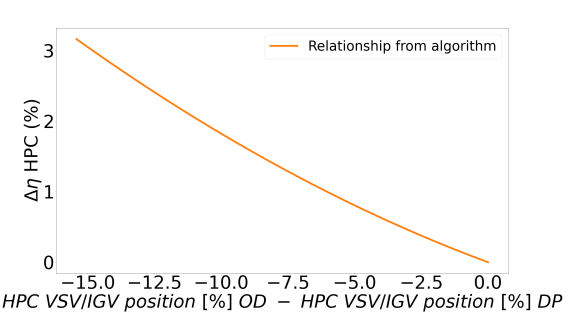

(a) HPC VSV/IGV position versus efficiency deviation relationship

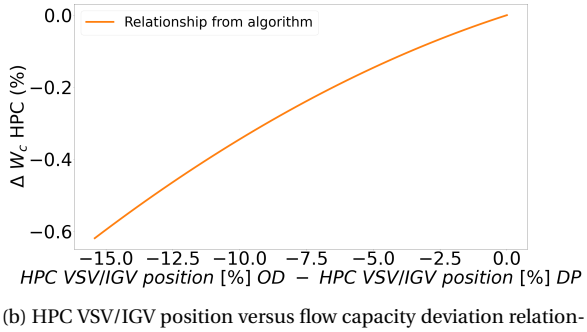

(b) HPC VSV/IGV position versus flow capacity deviation relationship

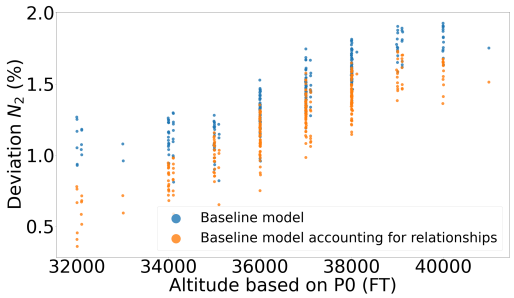

(c) N_2 deviation versus altitude

Figure 6.3: HPC VSV/IGV relationships determined by algorithm on baseline GEnx-1B model

HPT active clearance control

In Figure 6.4, the determined relationships for the HPT performance are displayed. The lower x-axis displays the actual calculated HPT clearance at cruise minus the clearance at take-off in mm. The upper x-axis displays this difference divided by the blade average HPT blade length to be able to put it in perspective with literature. The y-axis displays the performance deviation. Figure 6.4c displays the relation between the $t_{t,49}$ deviation and the actual HPT clearance. The direction of the relationships that are determined follow literature. Decreasing the clearance increases the efficiency and decreases the flow capacity. The extent to which the performance is increased or decreased is high compared to literature. Yoon From [63] follows, a decrease of 1% clearance of the span difference for an unshrouded turbine can result in a 2 % increase in efficiency. The results are not in line with literature, as a 0.5 % clearance decrease relative to blade span results in a 2.5% increase in efficiency. Again, this is caused by the fact that the algorithm benefits from decreasing the $T_{t,49}$ deviation. Since the HPT performance strongly influences this value, and the model output value for $T_{t,49}$ too high by a large margin, the algorithm goes to the bounds to decrease this error. That is what is seen in Figure 6.4c. The relationship between the clearance and the deviation is completely changed. The trend now follows the curve from Figure 6.4a. This is caused by the fact that the algorithm can not reach 0% deviation.

The flow capacity relationship is also high compared to theory. Following Holeski [15], a 1% relative clearance decrease can result in a 0.5% in flow capacity reduction. This is not in accordance with the results from the algorithm, as a 0.5% of relative clearance decrease is linked to a 1% in flow capacity reduction.

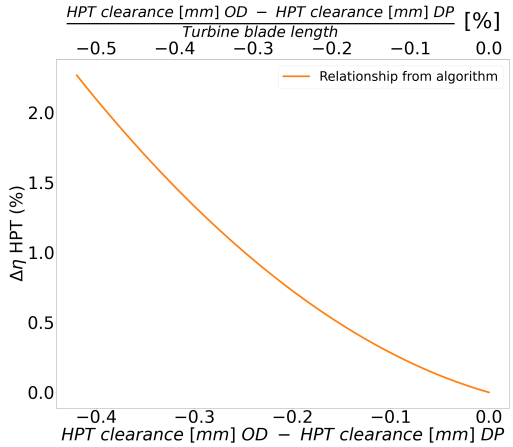

(a) HPT clearance versus efficiency deviation relationship

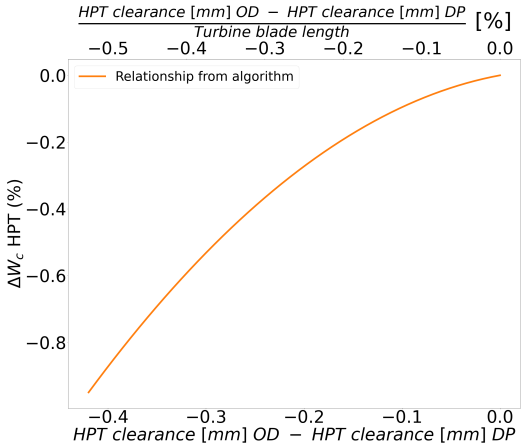

(b) HPT clearance versus flow capacity deviation relationship

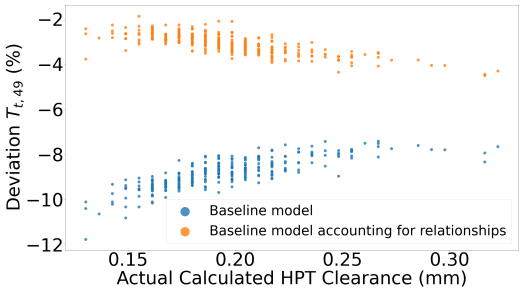

(c) $T_{t,49}$ deviation versus the actual calculated clearance

Figure 6.4: HPT clearance relationships determined by algorithm on baseline GEnx-1B model

LPT active clearance control

In Figure 6.5, the results from the algorithm for the LPT are displayed. The x-axis displays the valve position at cruise (OD) minus the valve position at take-off (DP). Figure 6.5c shows the dependency of $P_{s,3}$ and the ACCHPT valve position. At cruise, the valve is more open. Since the valve is scheduled based on altitude, the algorithm essentially compensates for performance change with altitude.

As is clear, the determined relationships are against the pre-set bounds. The algorithm getting stuck against its bounds indicates that, to obtain a lower objective function value, larger performance deviations were required. This effect also has another consequence. When looking at Figure 6.2e, it is clear that the $P_{s,3}$ error has two areas of deviation levels. As the LPT performance deviations strongly influence the $P_{s,3}$ measurement, operating points with a low LPTACC value would experience a smaller influence on the $P_{s,3}$ compared to an operating point with a high LPTACC value. This effect divides the deviation of $P_{s,3}$ in Figure 6.2e, in two levels. The two groups are also clearly visible in Figure 6.5c, in the high and low valve position difference. As no information is known about the actual clearance, a comparison with literature is not possible.

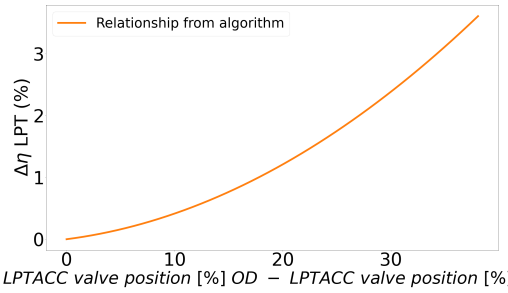

(a) LPTACC valve position versus efficiency deviation relationship

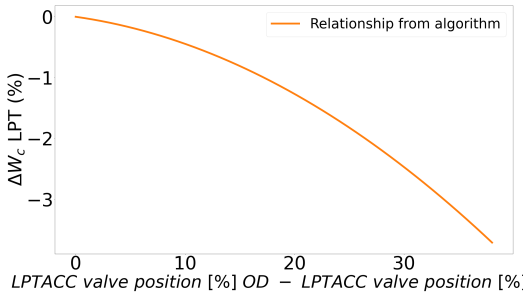

(b) LPTACC valve position versus flow capacity deviation relationship

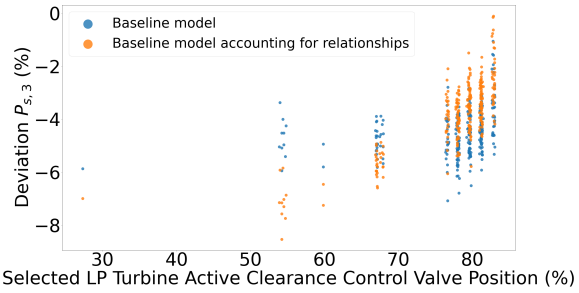

(c) $P_{s,3}$ versus the LPTACC valve position

Figure 6.5: LPTACC relationships determined by algorithm on baseline GEnx-1B model

6.1.3. Performance of engine components

As discussed, these results raise the question if the mass flow and efficiency of the LPS are correct. To further analyse the results, this section displays the actual efficiency at which the components operated.

The efficiency is dependent on both the operating position in the component map as well as the performance deviation induced by the algorithm. As the LPS is not influenced by the SPPs, only the operating condition determines its performance. Figure 6.6 shows three efficiencies:

- The average efficiency of the baseline GEnx-1B model not accounting for relationships at take-off.
- The average efficiency of the baseline GEnx-1B model not accounting for relationships at cruise.
- The average efficiency of the baseline GEnx-1B model accounting for relationships at cruise.

The comparison with the take-off condition is useful to put the results into context because those efficiencies represent the design point of the model.

As is visible, the efficiencies for the baseline model not accounting for the relationships at cruise are lower than the efficiencies at take-off. This is caused by the fact that the operating points in the component maps change when changing operating conditions. This effect causes the model to operate less efficiently, contributing to the deviation between the on-wing measurements and the model output.

As can be seen from the results of the baseline model that accounts for the relationships, the algorithm correctly increases the efficiency of the HPC, HPT and LPT. Yet, the efficiencies of the turbines are higher than expected for modern turbofan engines. Also, a 2.5% average efficiency increase is not expected from the reduction in clearance. From this analysis can be concluded that the algorithm is not capable of determining relationships for models with modelling error that is not caused by the secondary performance parameters. This is essentially caused by smearing and aggravated by the reduction of measurement sensors.

Therefore, the following section will display the results from the improved model with the adapted low pressure system.

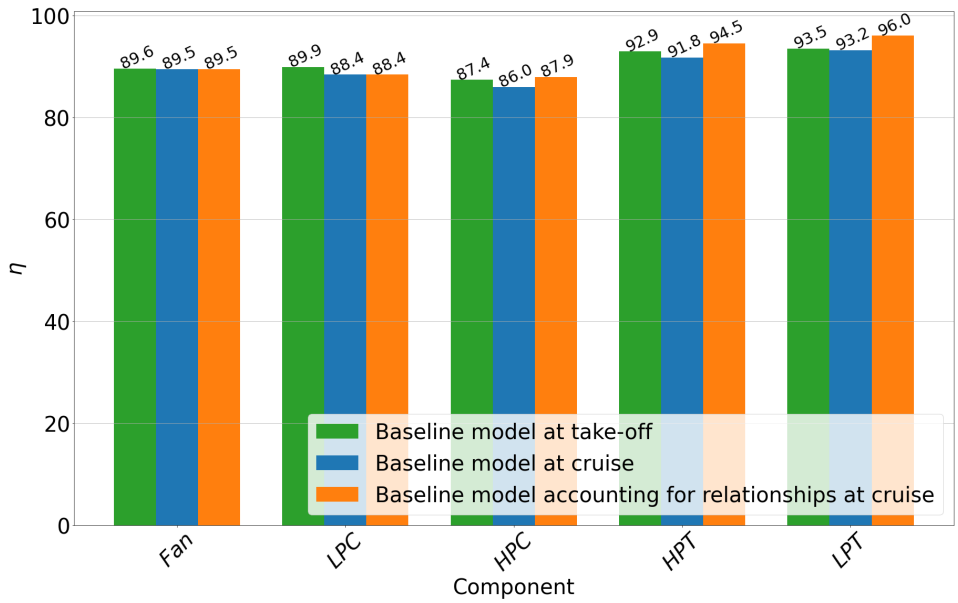

Figure 6.6: Average component efficiencies baseline GEnx-1B model

6.2. Results algorithm on improved model

In this section, the algorithm is run on the improved model with the modified low pressure system. This improved model features a $\Delta\eta$ and ΔW_c for the fan and LPC. This is done to increase the accordance of the model with the on-wing data since the results from section 6.1 indicate that the fan and LPC efficiencies are too low and the mass flows are incorrect.

The results in terms of accuracy increase are displayed in the first part, after which the individual influence of the secondary performance parameters is discussed.

6.2.1. Accuracy increase

In Figure 6.7, the results from the algorithm in terms of accuracy increase are displayed. The blue columns display the accuracy of the improved model. The orange columns display the results when the relationships from the algorithm are used in the improved model. Figure 6.8 shows the individual deviation from the measured value. As mentioned before, a negative value means that the model output is higher than the on-wing measurement.

Absolute deviation

As is clearly visible, the algorithm is capable of decreasing the deviation between the model and the on-wing data. For most measurements, a decrease in deviation is achieved. The N_2 average deviation is reduced by a large margin. The model's N_2 speed is increased, which is in line with the closing of the VSVs/IGVs. The decrease in fuel flow is in line with increasing the efficiencies, with the direct consequence of reducing the $T_{t,49}$. Again, the $T_{t,25}$ is barely influenced. The $P_{s,3}$ is increased strongly. This is probably due to the LPT performance increase, as the LPT has a strong influence on the $P_{s,3}$. The average modelling error is reduced by 65%.

Altogether, the algorithm is capable of decreasing the deviation between the on-wing measurements and the model output based on the secondary performance parameters.

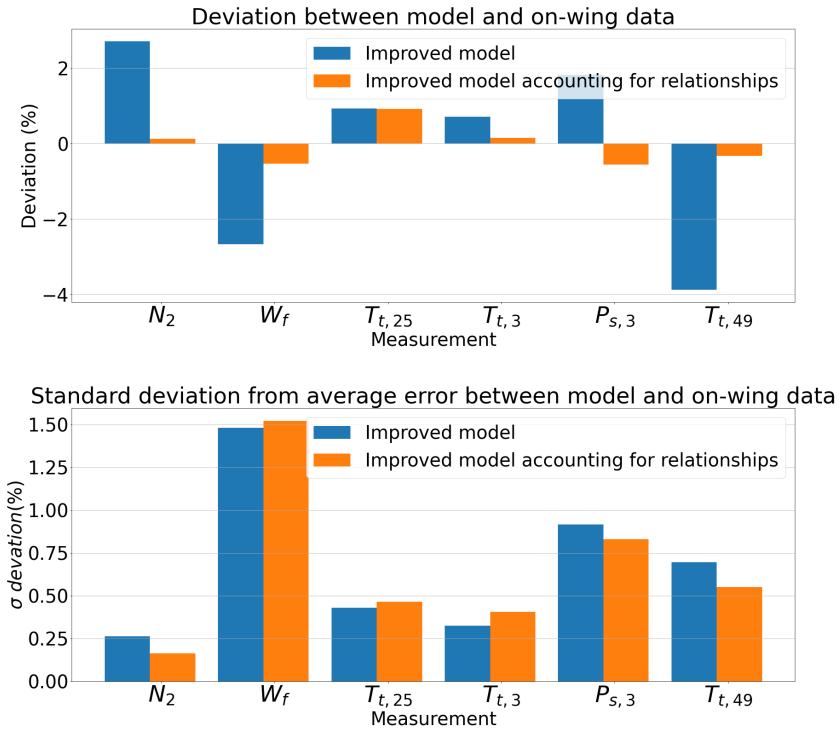

Figure 6.7: Algorithm deviation results between model output and on-wing measurements for improved GEnx-1B model

Standard deviation of error

As already mentioned, the standard deviation of the error is an important parameter to judge the working of the algorithm. In contrast to the results from the algorithm on the baseline model, the algorithm is capable of decreasing the standard deviation of the error for the improved model.

This is visible in Figure 6.7 and Figure 6.8. The N_2, $T_{t,49}$ and $P_{s,3}$ standard deviation is decreased. This indicates that the dependency of the measurement deviation and the secondary performance parameter is removed. Hence compensating for the SPP is successful. This can also be further explained by the fact that the performance of the HPC, HPT and LPT mainly influence the N_2, $T_{t,49}$ and the $P_{s,3}$ values.

From Figure 6.8 can also be concluded that there are still dependencies of measurement deviations on the corrected N_1 speed, that are not reduced. These dependencies are still present due to inaccuracies in the component maps. This, in combination with the sensor noise, keeps the standard deviation of the error at a certain minimum level.

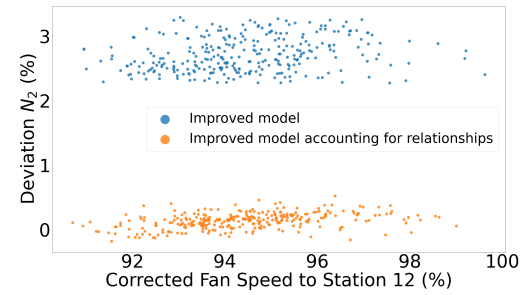

(a) N_2 deviation from improved GEnx-1B model accounting and not accounting for relationships

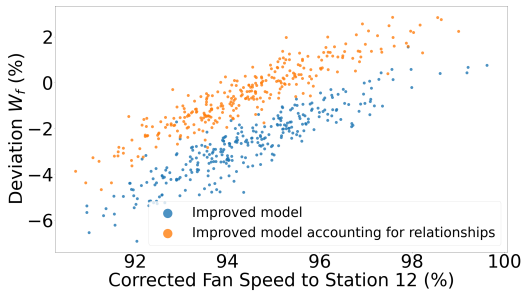

(b) W_f deviation from improved GEnx-1B model accounting and not accounting for relationships

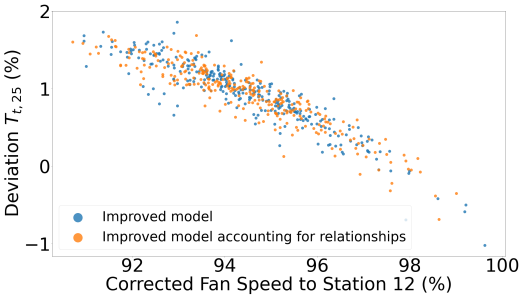

(c) $T_{t,25}$ deviation from improved GEnx-1B model accounting and not accounting for relationships

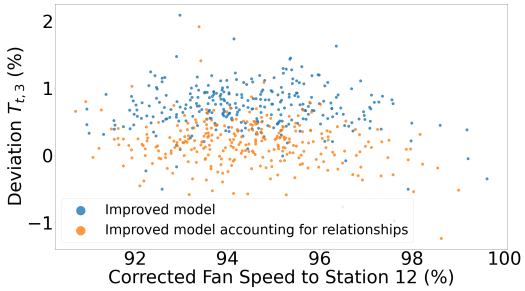

(d) $T_{t,3}$ deviation from improved GEnx-1B model accounting and not accounting for relationships

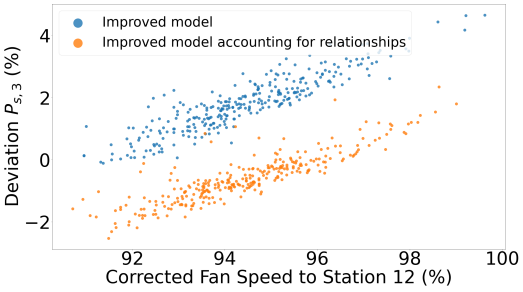

(e) $P_{s,3}$ deviation from improved GEnx-1B model accounting and not accounting for relationships

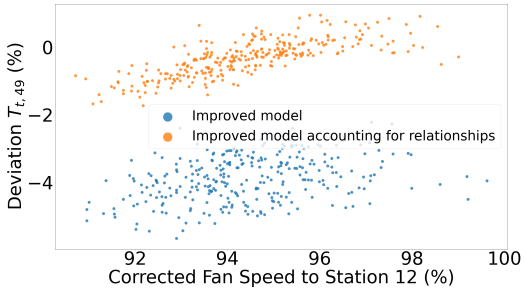

(f) $T_{t,49}$ deviation from improved GEnx-1B model accounting and not accounting for relationships

Figure 6.8: Deviation of parameters for improved GEnx-1B model accounting and not accounting for relationships

6.2.2. Individual relationships

In this section the relationships are displayed that were determined for the improved GEnx-1B model.

HPC variable geometry

In Figure 6.9, the determined relationships are displayed. Also, the dependency of the N_2 deviation on the altitude is displayed. The flow capacity is decreased largely with the closing of the IGVs/VSVs. This is a large contributor to the increase in N_2 speed. This is again in line with theory as explained in subsection 6.1.2. Also,

the efficiency is increased by a maximum of 1.2%. This is done to keep the efficiency at an acceptable level since the mass flow capacity deviation reduces the efficiency by moving the operating point further away from the surge line to an area of lower efficiency. So basically, the compressor will operate at approximately the same efficiency and corrected mass flow, only with a higher corrected spool speed. This will be substantiated by subsection 6.2.3, in which the operating efficiencies are displayed. The effect of this deviation is clearly visible in the results from Figure 6.8a. The standard deviation of the N_2 error is reduced significantly. This is also clear from Figure 6.9c, in which it is visible that the dependency of the N_2 deviation on the altitude is reduced. The reduction of the slope of a linear regression through the points is 27%. The VSV/IGV difference between cruise and take-off is dependent on the altitude. So the reduction of the dependency of the N_2 deviation on the altitude indicates that this model accounts for the secondary performance parameter of variable geometry.

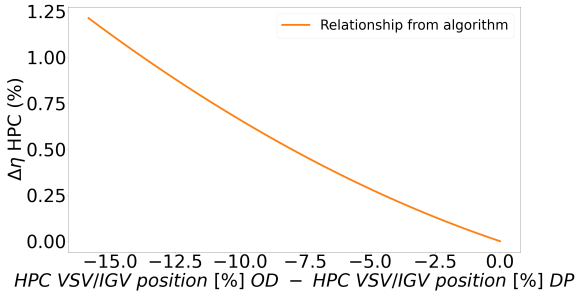

(a) HPC VSV/IGV position versus efficiency deviation relationship ships

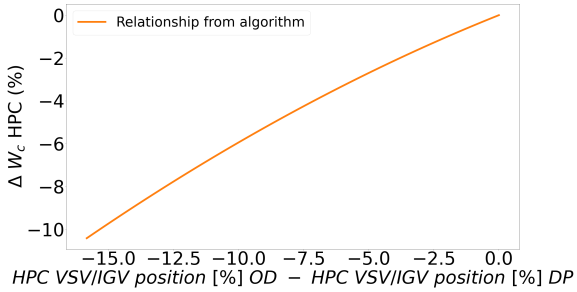

(b) HPC VSV/IGV position versus flow capacity deviation relation-

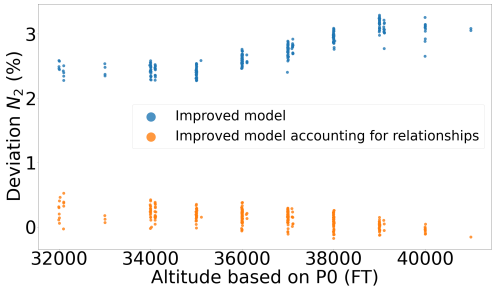

(c) N_2 deviation versus altitude

Figure 6.9: HPC VSV/IGV relationships determined by algorithm on improved GEnx-1B model

HPT active clearance control

In Figure 6.10, the determined relationships for the HPT clearance are set out. Again, two x-axes are defined for the actual clearance decrease and the clearance decrease relative to the turbine blade length. Clearly, the corrected mass flow is reduced. This is what is expected when the clearance is reduced. Also, the efficiency in increased. The comparison with literature results in the conclusion that the algorithm overestimates the effect of the clearance on the efficiency. As mentioned before, the expected performance increase for unshrouded blades amounts up to 2% per 1% clearance decrease relative to the turbine blade length. The clearance decrease relative to the blade span is maximum 0.5%, which should add up to a 1% efficiency increase. From the analysis, a maximum of 2.5% is found. This can be caused by other modelling errors, for which the HPT performance increase compensates. The flow capacity is only reduced slightly, this is better in line with literature. A maximum of 0.33% in flow capacity reduction is linked to a 0.5% of relative clearance decrease. Following Holeski [15], a 1% relative clearance decrease results in a flow capacity reduction of 0.5%.

From Figure 6.10c can be concluded that the absolute $T_{t,49}$ error is decreased. Also, the dependency of the $T_{t,49}$ deviation on the actual calculated HPT clearance is slightly reduced. The reduction of the slope of a linear regression through the points is 16%. This indicates the working of the algorithm.

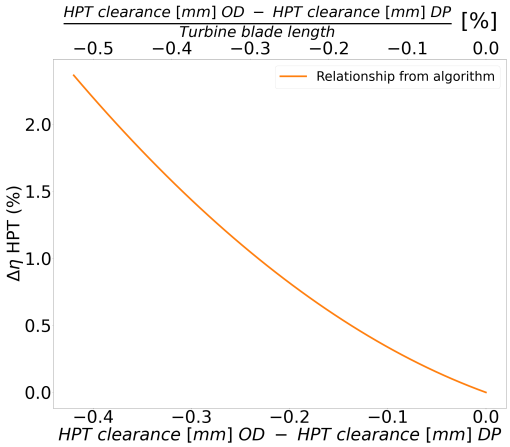

(a) HPT clearance versus efficiency deviation relationship

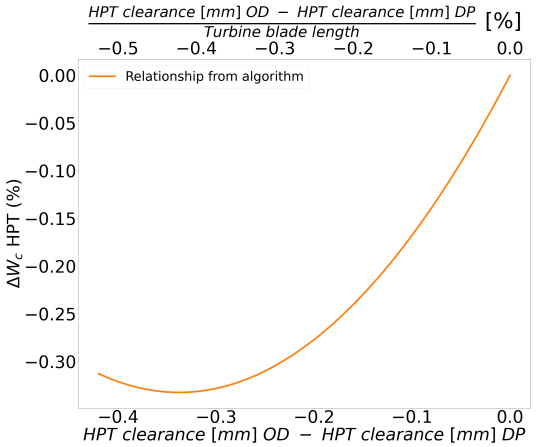

(b) HPT clearance versus flow capacity deviation relationship

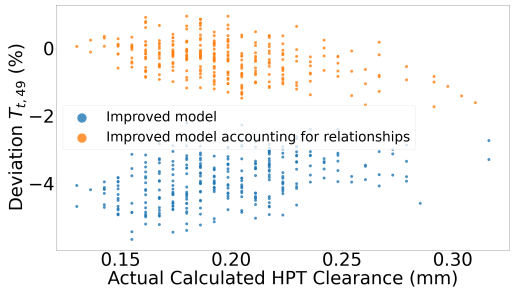

(c) $T_{t,49}$ deviation versus the actual calculated clearance

Figure 6.10: HPT clearance relationships determined by algorithm on GEnx-1B model with modified LPS

LPT active clearance control

In Figure 6.11, the relationships for performance deviation of the LPT are displayed. The algorithm determined relationships that reduce the flow capacity and increase the efficiency for increasing the position of the ACCLPT valve. As indicated before, the valve is scheduled with altitude. It essentially accounts for the performance increase with altitude. Since no further information is known about the actual clearance, the magnitude of the performance deviation can not be compared to literature. However, it is expected that the turbines operate more efficiently during cruise, since the engines are designed to operate at their optimal efficiency during cruise. Therefore, this is a successful result for compensating for operating conditions. From Figure 6.11c can also be concluded that the algorithm reduced the dependency of the $P_{s,3}$ measurement deviation and the valve position. The reduction of the slope of a linear regression through the points is 43%. This is important because the $P_{s,3}$ value is strongly influenced by the LPT performance.

6.2.3. Performance of engine components

Again, the model can be analysed further by visualising the efficiencies at which the components operate. Figure 6.12 shows three efficiencies:

- The efficiency of the baseline GEnx-1B model at take-off.
- The efficiency of the improved GEnx-1B model not accounting for relationships at cruise.
- The efficiency of the improved GEnx-1B model accounting for relationships at cruise.

As is visible, the efficiencies of the LPS are increased to their design values. This is an even higher efficiency than the efficiency at which the baseline model operates during take-off conditions. This is logical because it is expected that the operating efficiency during cruise is higher than during take-off.

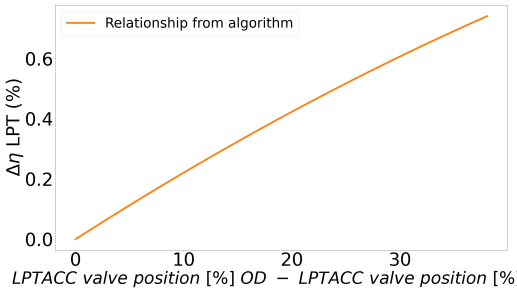

(a) LPTACC valve position versus efficiency deviation relationship

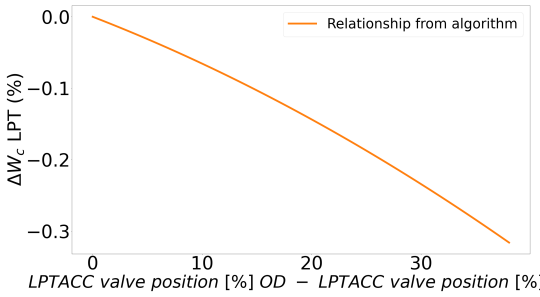

(b) LPTACC valve position versus flow capacity deviation relationship

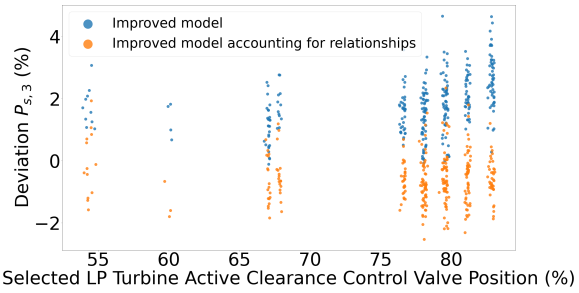

(c) $P_{s,3}$ versus the LPTACC valve position

Figure 6.11: LPTACC relationships determined by algorithm on improved GEnx-1B model

From Figure 6.12, is clear that the HPC, HPT efficiencies for the non adapted model with LPS modification at cruise are lower than the efficiencies at take-off for the standard model. As can be seen from the results of the adapted model, the algorithm correctly increases the efficiency of the HPC, HPT and LPT.

The efficiency of the HPC is corrected by the relationships for the HPC variable geometry. However, the efficiency increase is lower than the relationship from the HPC suggest. This is caused by the fact that the operating point in the compressor map is changed by the ΔW_c to a lower efficiency region, meaning the $\Delta\eta$ also has to compensate for this efficiency loss. Altogether, these running efficiencies are closer to what is expected from modern gas turbines compared to the analysis on the baseline model.

From these results can be concluded that the algorithm is capable of reducing the error between the model and the on-wing measurements. This is all done on the basis of the secondary performance parameters. The following section will display the results of the application of these determined relationships on different GEnx-1B engines.

6.3. Application of relationships on various GEnx-1B engines

To understand if the relationships are only suitable for one engine, this section displays the results of using the determined relationships from the algorithm in combination with the improved model for different GEnx-1B engines. For this analysis, five datasets with 300 operating points from engine ESN956XXXB to ESN956XXXF are evaluated. In Figure 6.13, the average errors are given for the five GEnx-1B engine datasets with approximately the same EGTMHD. Both the results from the improved model and the improved model that accounts for the relationships are displayed. As is clear from the figures, the improved model that accounts for the relationships has a lower error between the model and the on-wing data for the other GEnx-1B engines. The average modelling error is decreased from 1.8% to 0.7%. This is a decrease of 61%. The maximum remaining error is 2% for the $P_{s,3}$ measurement from engine D. This error is probably caused by engine-to-engine differences.

Figure 6.14 displays the standard deviation of the errors between the model output and on-wing measurements. The standard deviations are mostly decreased. The average decrease in standard deviation is 7%. This substantiates the belief that the algorithm is capable of finding relationships that compensate for the secondary performance parameters, as they also work when applied to different GEnx-1B engines. This

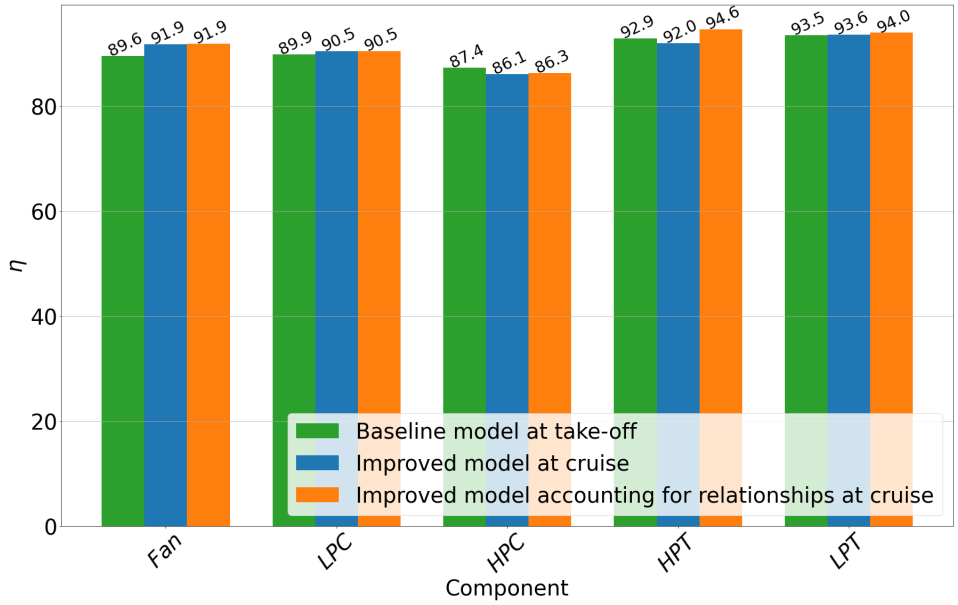

Figure 6.12: Average component efficiencies GEnx-1B model with LPS modification

means that the determined relationships can be used to perform GPA on different engines as well, and no overfitting to the 956XXXA engine dataset has occurred.

6.4. Conclusion

This section evaluated the results from the algorithm for the two models and the application of the relationships on different GEnx-1B engines. It is concluded that the algorithm does not operate properly on the baseline model due to the fact that it has to overcome too large a performance difference. The results from the algorithm on the improved model are promising. The N_2, W_f, $p_{s,3}$, $t_{t,3}$ and the $T_{t,49}$ errors are reduced significantly. This was also true when applying the determined relationships on different engines. Therefore, the algorithm can be used to decrease the modelling error caused by secondary performance parameters: VSVs/IGVs for the HPC and active clearance control for the HPT and LPT. Also, the direction of the relationships based on the secondary performance parameters was consistent with literature. However, the magnitude of the relationships is large compared to expectations. This will further be discussed in chapter 8. The following chapter will perform an on-wing gas path analysis with both the improved GEnx-1B model not accounting for the relationships and the improved GEnx-1B model with embedded relationships.

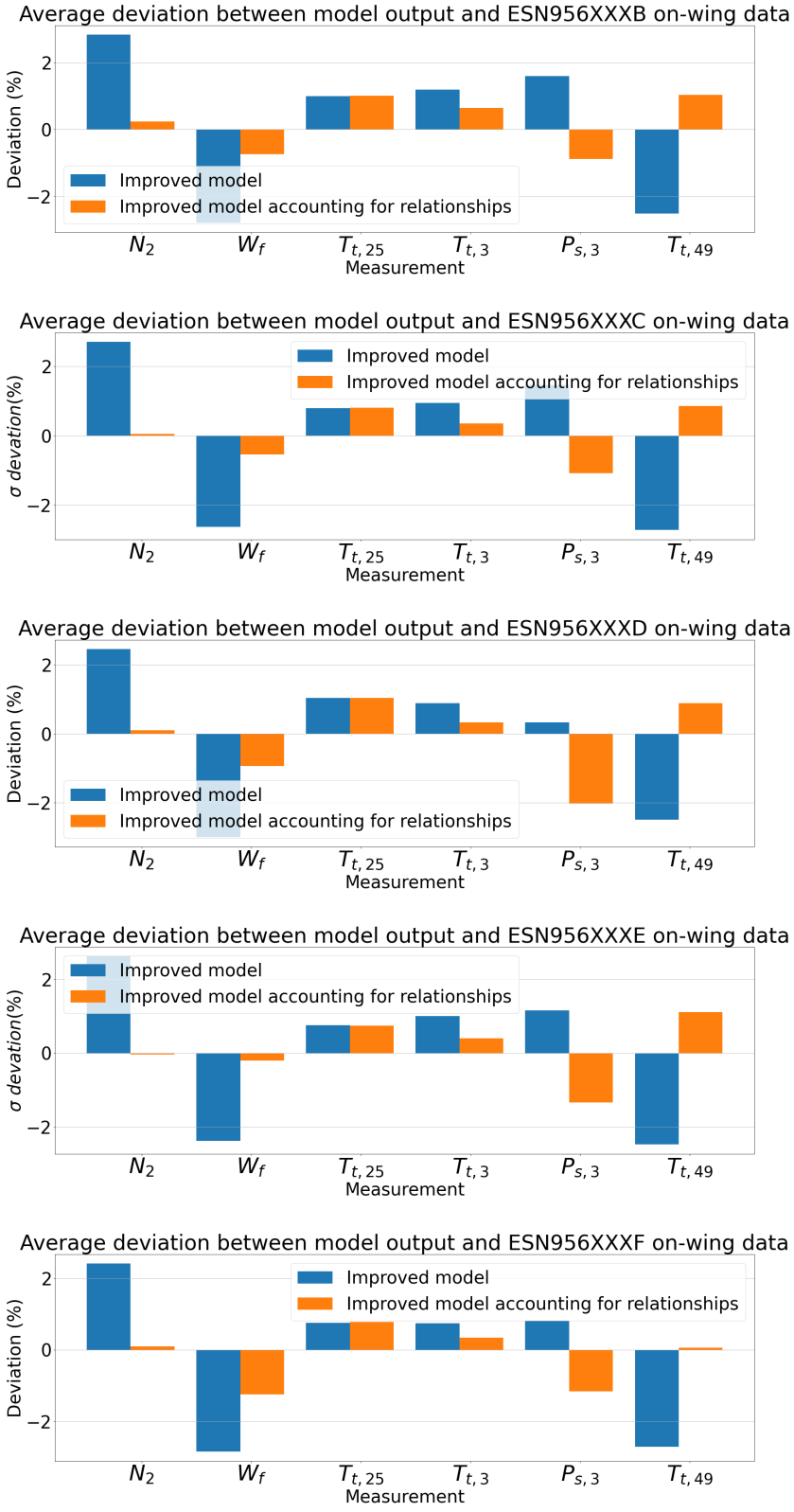

Figure 6.13: Deviation results between model output and on-wing measurements with relationships applied on multiple GEnx-1B engine datasets

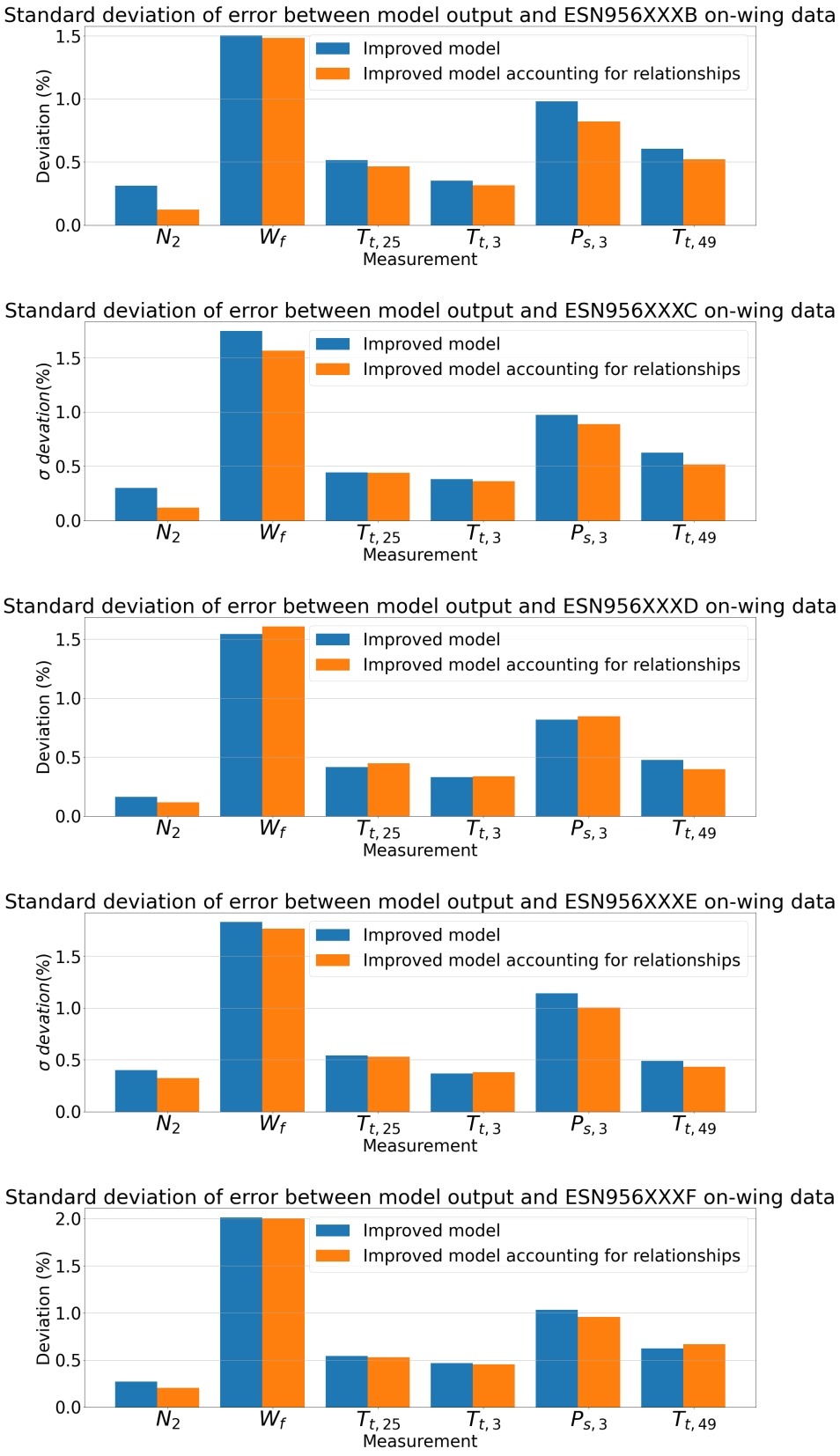

Figure 6.14: Standard deviation results between model output and on-wing measurements with relationships applied on multiple GEnx-1B engine datasets

7

Gas Path Analysis on GEnx-1B on-wing data

In this chapter, a gas path analysis is performed with the improved GEnx-1B model with the relationships embedded and compared to the GPA results from the improved model without embedded relationships. This chapter is divided into four sections. The first section introduces the background of the engine and the case on which the working of the determined relationships is validated. The second section explains the GPA methodology. The third section displays the GPA results. Finally, conclusions are drawn.

7.1. Engine background

The engine that is used to validate the working of the determined relationships is the ESN956XXXA. This is also the engine for which the relationships were determined. As already mentioned, this engine suffered an EGT redline exceedance. Such an event requires instant engine removal for inspection. The cause of the redline exceedance was an HPT stage 1 blade burn-down. This burn-down also damaged the LPT through impact damage. As GPA should identify this failure, this is an ideal case to validate the increased accuracy of the gas path analysis caused by accounting for the relationships. Aside from the redline exceedance event, water washes are also identified. A water wash is a procedure by which the fouling on the engine compressor blades is removed, enhancing the performance of the compressors. This should be clear from the GPA results.

7.2. GPA methodology

The GPA methodology that is used is described in subsection 3.1.6 and further specified by Rootliep [37]. The performed analysis is a single operating point analysis for cruise conditions using the EA-GPA tool and the variable bounds method [37]. Two analyses are performed:

- An analysis with the improved GEnx-1B model that does not account for the relationships.
- An analysis with the improved GEnx-1B model that does account for the relationships.

Both models feature the modified low pressure system. A comparison will be made on how well it identifies the water wash and HPT blade burn-down. Also, the spread of the GPA results will be quantified as a root mean square error of the GPA evaluations.

7.3. GPA results

In this section, the results from the gas path analysis are displayed. First, the results from the individual components are displayed. In the graphs, the red area specifies the time frame of the overhaul after the HPT blade burn-down. The vertical black lines indicate the water washes. The time is anonymised due to confidentiality. The total time duration is 4 years. In the second section, the root mean square error of the GPA results is quantified.

7.3.1. Fan

In Figure 7.1, the GPA results from the fan are displayed. As is visible, no clear difference between the two models is present. The GPA results are fairly constant over the whole time period. This is in line with the expectations because the fan module does not suffer from severe deterioration. The small variation is also partly due to the variable bounds method restricting the fan deterioration. Around the water washes, a small peak in flow capacity and efficiency can be noted. This is in line with what is expected. The HPT blade failure is also notable in the efficiency and flow capacity, which is not desired as the fan did not experience any damage. This is probably caused by smearing. Accounting for the relationships does not seem to influence the fan GPA results.

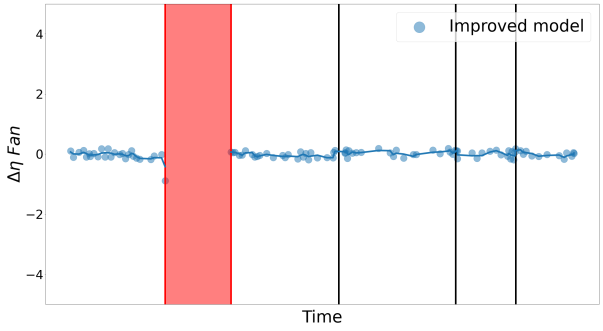

(a) Improved model not accounting for relationships

(b) Improved model accounting for relationships

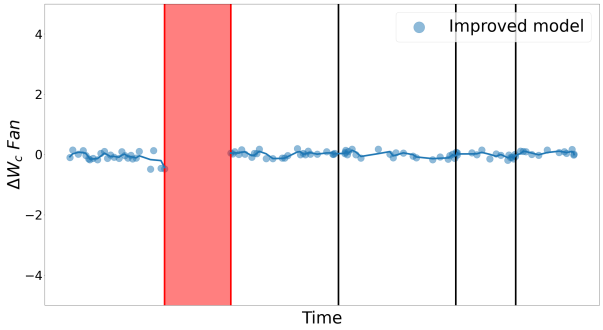

(c) Improved model not accounting for relationships

(d) Improved model accounting for relationships

Figure 7.1: Fan GPA results

7.3.2. LPC

In Figure 7.2, the GPA results from the LPC are displayed. As is clear, there is a noticeable difference between the model that accounts for the SPPs and the model that does not. The efficiency and flow capacity peaks after the water washes are more apparent for the model that does account for the SPPs. This is probably caused by the accounting for the SPPs which takes away uncertainties in the GPA analysis leading to better identification of deterioration. The HPT blade failure does not show up in the LPC flow capacity and efficiency for both models, which is expected as this component did not suffer from the failure.

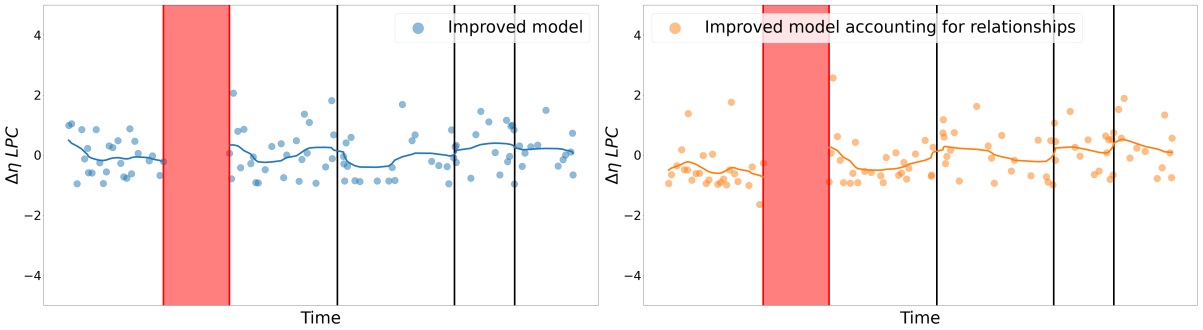

(a) Improved model not accounting for relationships

(b) Improved model accounting for relationships

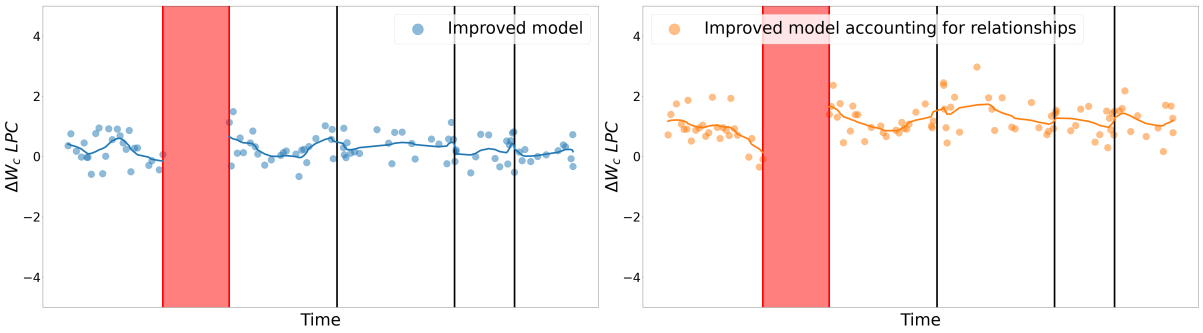

(c) Improved model not accounting for relationships

(d) Improved model accounting for relationships

Figure 7.2: LPC GPA results

7.3.3. HPC

In Figure 7.3, the results from the two models are displayed. As is clearly visible from Figure 7.3a and Figure 7.3b, the water washes are clearly visible in the efficiency graphs for both models. In Figure 7.3c and Figure 7.3d, the flow capacity of the HPC is displayed. It is visible that the HPC flow capacity shift caused by the water wash is more distinct for the model that accounts for the relationships. This is also expected because of the large influence of the VSVs/IGVs on the HPC flow capacity. For both models, the HPT blade failure does not show up as HPC deterioration. This is desirable since the HPC was not affected by the failure. However, the overhaul has a strong effect on the flow capacity, which is not expected as no maintenance is performed on this component. This phenomenon can have two explanations. One possible cause is the re-rigging of the variable stator vanes leading to a different setting of VSV/IGV angles than the algorithm was run for. The second cause can be a water wash that is performed during the test cell run, enhancing the performance of the compressor.

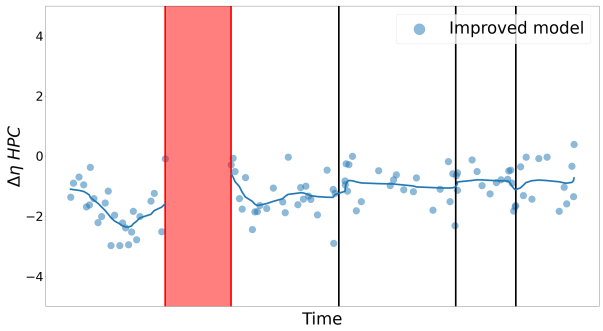

(a) Improved model not accounting for relationships

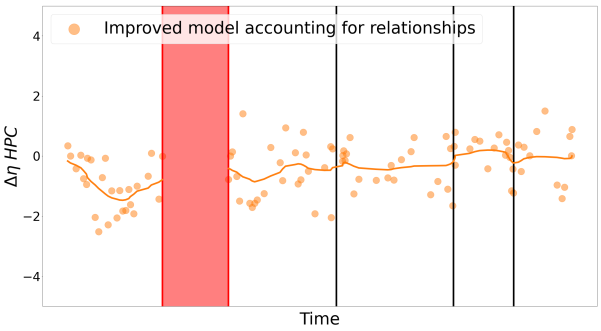

(b) Improved model accounting for relationships

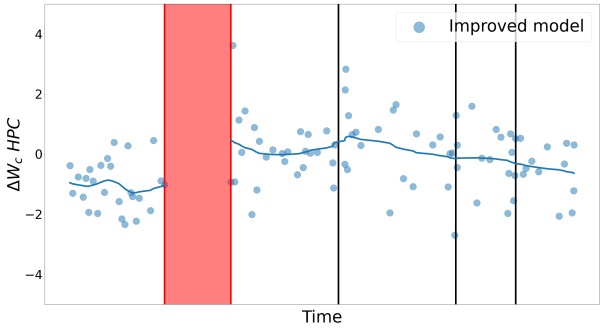

(c) Improved model not accounting for relationships

(d) Improved model accounting for relationships

Figure 7.3: HPC GPA results

7.3.4. HPT

In Figure 7.4, the results from the HPT are displayed. As is clear, a slight HPT efficiency and flow capacity change is visible after a water wash for both models. As the goal of a water wash is to decrease the compressor fouling, no impact is expected on the HPT. This is probably caused by smearing. Besides, the indication of the HPT blade burn-down is clearly visible. The efficiency is decreased, and the flow capacity is increased before the actual HPT blade failure. Both these trends are in line with what is expected. The actual HPT blade burn-down event is clear from the efficiency and flow capacity deviation of -4% and +2%, respectively. Also, the performance restoration is clear after the overhaul. No difference in identifiability of the HPT blade burn-down is seen between the two models. The difference between the two models is visible in the spread of the HPT GPA results. The scatter of the flow capacity is lower for the model that accounts for the relationships, which indicates the working of the algorithm. This is also confirmed by subsection 7.3.6.

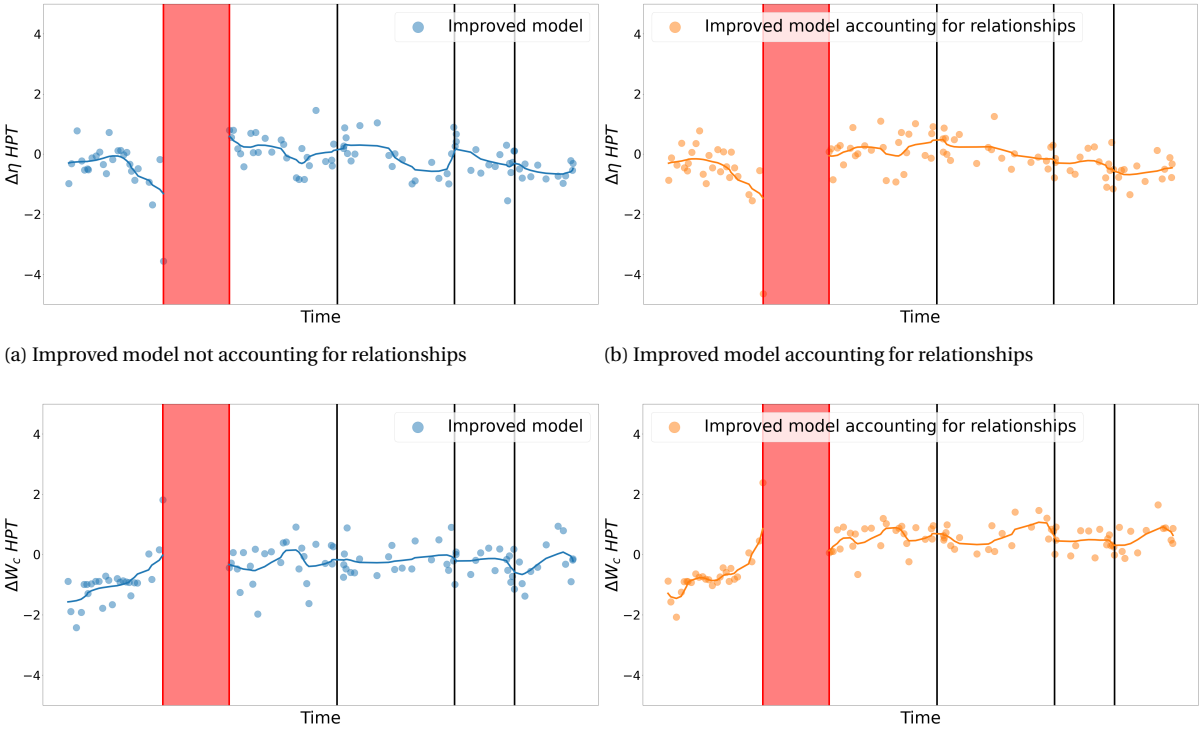

(a) Improved model not accounting for relationships

(b) Improved model accounting for relationships

(c) Improved model not accounting for relationships

(d) Improved model accounting for relationships

Figure 7.4: HPT GPA results

7.3.5. LPT

In Figure 7.5, the results from the LPT are displayed. As in line with theory, both models do not indicate a large performance increase caused by a water wash. As mentioned, the HPT blade failure also damaged the LPT component. The performance decrease is clearly indicated by both models in the decrease in efficiency. The increase in flow capacity is better represented by the model that accounts for the relationships. Furthermore, the model that accounts for the relationships features a reduction in scatter for the flow capacity GPA results. This will also be confirmed in subsection 7.3.6. The following section will further discuss the scatter of the GPA results.

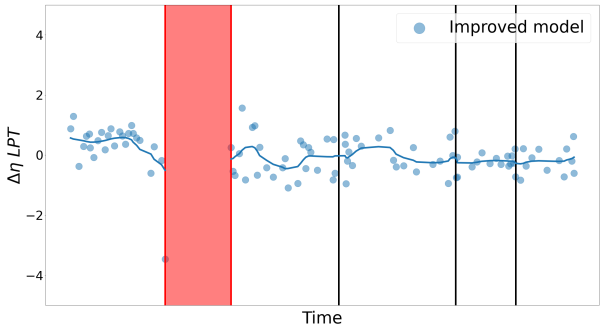

(a) Improved model not accounting for relationships

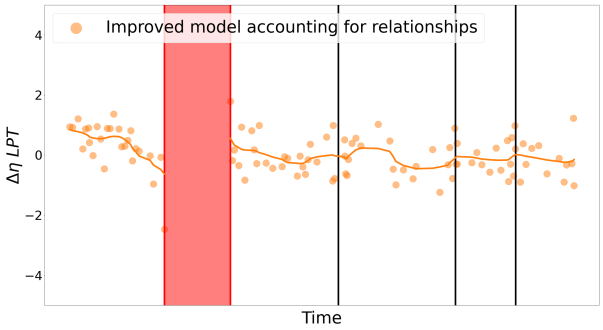

(b) Improved model accounting for relationships

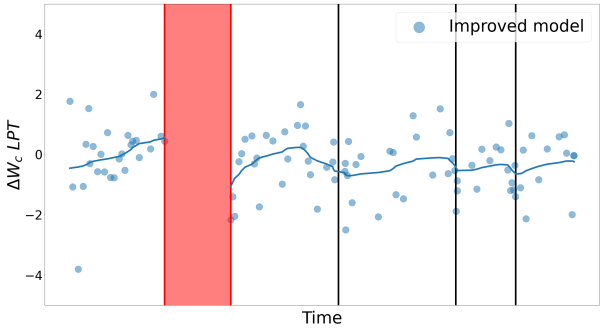

(c) Improved model not accounting for relationships

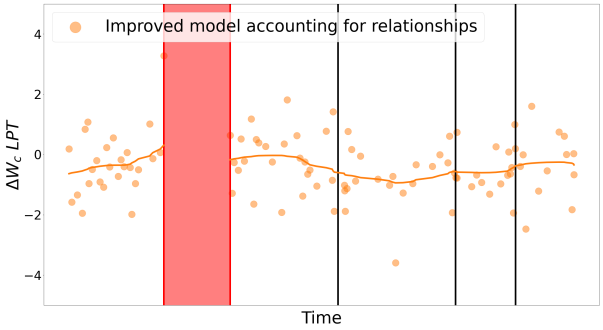

(d) Improved model accounting for relationships

Figure 7.5: LPT GPA results

7.3.6. GPA root mean square error

In Figure 7.6, the root mean square error (RMSE) from the GPA evaluations is given for both models. This is done to quantify the scatter of the GPA evaluations. This value is determined by calculating the RMSE of the individual GPA evaluations with respect to a linear regression that is constructed between the individual water washes and the HPT failure event. This is an important metric because it quantifies the unmodelled effects. Hence, a lower RMSE means a more accurate GPA assessment. As expected, the RMSE for most component evaluations is reduced. The average RMSE overall engine health parameter evaluations is reduced by 8%. This is a successful result and also indicates the working of the algorithm.

7.4. Conclusion

From the results in this chapter is concluded that accounting for secondary performance parameters by using the determined relationships increases GPA accuracy. The model that accounts for the relationships shows better correspondence with known engine history information. Also, the GPA results scatter is decreased. The following chapter will discuss the results of this thesis.

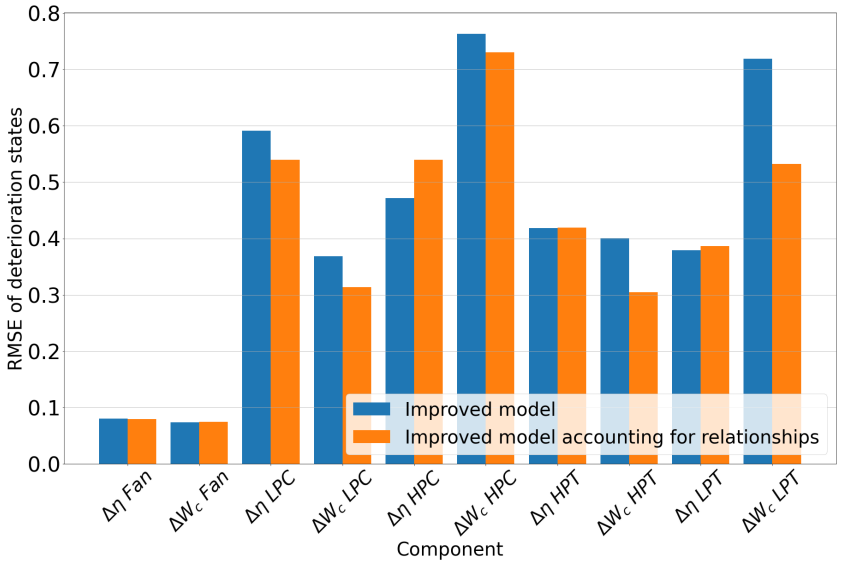

Figure 7.6: RMSE of GPA evaluations

8

Discussion

This chapter will put the findings of this thesis into context and will discuss their relevance and limitations. First, the major findings are summarised, after which the results from the algorithm on the baseline model are discussed. Afterwards, the results from the improved model are discussed. Subsequently, the results of using the relationships on different engines are treated. Lastly, the GPA results are discussed.

8.1. Major findings

The main research question of this thesis was: can relationships based on secondary performance parameters and determined by an evolutionary algorithm increase the accuracy of GPA engine models for various operating conditions? To answer this question, this research identified the following major findings.
The results from the verification of the algorithm on simulated data indicate that the algorithm can accurately identify secondary performance parameter effects. The validation of the algorithm using GEnx-1B on-wing data and the baseline engine model resulted in unrealistic relationships. The validation using the improved engine model suggests that the algorithm can identify relationships between secondary performance parameter effects and the consequent component performance deviation that are in line with literature. Accounting for these relations increased model accuracy and consequently GPA accuracy. The following section will discuss the results from the algorithm in the baseline GEnx-1B model.

8.2. Results baseline model

As indicated in section 6.1, the application of the algorithm on the baseline model resulted in the algorithm failing to determine relationships that were in line with literature. Since the deviation between the model output and the on-wing measurements was too large, the relationships could not reduce the deviation to zero percentage. Mainly the fuel flow and the exhaust gas temperature deviated by a large margin. This is likely caused by an incorrect operating point in the fan and LPC map at cruise conditions.

Following Kurzke, [29] the operating point in the fan map moves away from the surge line when going from take-off to cruise due to the nozzle getting choked during cruise conditions. This is accompanied by the operating point shifting to an area of higher corrected flow and efficiency and lower pressure ratio. However, this does not happen in the current model. An analysis indicated that this behaviour was caused by an incorrect velocity coefficient in the bypass nozzle of the design point model. This caused a large residual modelling error.

As mentioned, the algorithm tries to reduce the difference between the on-wing measurements and the model output to zero percentage. Therefore, the algorithm compensates for the large residual modelling errors by overestimating the magnitude of the secondary performance parameter effects. This effect is aggravated by the reduction of gas path sensors in modern turbofan engines. However, Stamatis [45] indicated that using multiple operating points in the algorithm can mitigate the reduced sensor problem. The multi-operating point method is also used in the proposed algorithm. The results indicate that using this method did not mitigate the reduced sensor problem in this application.

It is determined that the algorithm is not able to accurately separate the effect of residual modelling error from secondary performance parameter effects.

8.3. Results improved model with modified low pressure system

As mentioned, the results from the baseline model suffer from incorrect mass flows through the fan and LPC. Therefore, an improved model is introduced, which is the baseline model modified by decreasing the mass flow through the fan and the LPC and increasing the efficiency towards their design efficiency. However, a reduction in fan and LPC corrected mass flow goes against the expected engine behaviour when going from take-off to cruise operating conditions.

As explained, the corrected mass flow through the fan should increase when going from take-off to cruise for large bypass turbofan engines. In the current models, this does not happen as explained in the previous section. To increase the engine model accuracy, the work required by the fan is decreased. This can be done in two ways, decreasing the pressure ratio or the mass flow. For this analysis, the mass flow is decreased to reduce the large error in $T_{t,25}$, fuel mass flow and exhaust gas temperature to a reasonable level. The modifications made influence the results of the algorithm and thereby the generalisability of the results.

The results from the algorithm on the improved model provide insight into the ability to reduce the modelling error by determining relationships based on secondary performance parameter settings.

From literature follows that the closing of the IGVs/VSVs of the HPC mainly changes the relationship between the corrected flow and rotational speed. Closing the vanes should result in lower corrected flow associated with the corrected speed lines [27]. This should increase the N_2 rotational speed for constant N_1 speed [29]. The results from using the relationships are in accordance with literature as the corrected flow is decreased and the N_2 speed is increased. Decreasing the turbine clearance should increase the efficiency and decrease the flow capacity [6, 63]. The algorithm determined relationships that increased the efficiency for smaller clearances and decreased the flow capacity. The direction of the relationships is in line with literature. However, the magnitude of the efficiency increase is large [63]. This can still be caused by residual errors in the low pressure system. Also, the literature is only a reference value. The exact influence of the clearance can vary for different turbines. The LPTACC relationships have a small magnitude but managed to reduce the dependency of the $P_{s,3}$ deviation on the ACCLPT valve position. This is a successful result for compensating for the LPT performance difference at various operating conditions. However, it can not be compared to literature because no actual clearance is known.

These results indicate correct compensation for the secondary performance parameters regarding the direction of the performance deviation captured in the relationships. Accounting for these relationships in the engine model reduces modelling error. This is a satisfactory result.

As mentioned, the results of the algorithm are influenced by the quality of the model used in the case study. Therefore, to validate the algorithms ability to identify the secondary performance parameter effect with more certainty, a higher accuracy engine model is required.

8.4. Application of relationships on multiple engines

For the multi-engine analysis from section 6.3, five engines are chosen with an approximately equal EGT margin hot day. The determined relationships are tested on multiple GEnx-1B engines. From the results can be concluded that the error is strongly decreased, indicating that severe overfitting on ESN956XXXA has not occurred. Still, some errors are present. This can be explained by the fact that the various engines may have the same EGT margin but not the exact same deterioration grade of the engine. The differences may be present due to engine-to-engine differences. Another possible explanation can be that the training dataset of the algorithm contained data points from flights with a different EGTMHD compared to the selected 5 GEnx-1B engines, as the data points are randomly selected from the time period specified in section 5.5. In this time period, the EGTMHD varies slightly. If the relationships could be calibrated using a set of engines, the relationships would be created for the absolute baseline performance of the average GEnx-1B engine. This might be possible when the first GEnx-1B engines start receiving full shop visits.

8.5. Gas path analysis on GEnx-1B on-wing data

With the improved model that accounts for the relationships, a gas path analysis is performed. The results are compared to the GPA analysis from the improved model that does not account for the relationships. Overall, a decrease in RMSE of the GPA evaluations is achieved by accounting for the relationships. Besides, using the relationships resulted in better identification of the water washes and the turbine blade failure. However, the RMSE of the GPA evaluations is still high. This is probably caused by errors in the LPC and fan map. Therefore, the LPC and fan component maps should be tuned for more accurate results. Besides, as already explained,

the effect of the velocity coefficient in the nozzles from the model should be investigated to achieve better results.

9

Conclusions & recommendations

Based on the results in this report, the main conclusions are drawn, and an answer is given to the research question: Can relationships based on secondary performance parameters and determined by an evolutionary algorithm increase GPA model accuracy and consequently GPA accuracy? Also, recommendations are provided for further research.

9.1. Conclusions

The goal of this thesis is to research the possibility to increase the accuracy of the GEnx-1B model at cruise conditions based on the additional information on the secondary performance parameters. The main areas of interest are GEnx-1B engine data, secondary performance parameters, GPA model development, and algorithm development. Combining these concepts led to the development of an algorithm that determines relationships between secondary performance parameters and component performance deviation based on on-wing performance data. This thesis investigates if accounting for these relationships increases engine model accuracy and consequently GPA accuracy. The conclusions from this research are displayed below:

- **Secondary performance parameters:** Engine performance is influenced by secondary performance parameters like variable geometry, bleed flows, clearance control and the power off-take. Modern turbofan engines collect Continuous Engine Operating Data (CEOD), in which information on the secondary performance parameter settings is stored. From CEOD analysis, it is concluded that the secondary performance parameter settings are significantly different at cruise conditions compared to take-off conditions.

- **Methodology:** The proposed method uses a differential algorithm, which is a sub-form of the evolutionary algorithm class, combined with on-wing performance data to determine relationships between secondary performance parameter settings and the consequent performance deviation of the component. The differential algorithm is used as optimiser because of its ability to deal with noisy data and local minima. On-wing performance data is used because of the great amount of information on the secondary performance parameters.

- **Verification of method:** The introduced method is verified using simulated data from the standard BIGFAN GSP model. The algorithm proved capable of accurately identifying the effects of secondary performance parameters on three components using 12 engine measurements. Reducing the number of available measurements to 6 makes the identification of individual secondary performance parameter effects more prone to error. Overall, it is concluded that the algorithm can determine relationships that reduce modelling error if accounted for in engine models.

- **Validation of method using baseline GEnx-1B model:** The method is validated using on-wing cruise data from the ESN956XXXA GEnx-1B engine and the baseline GEnx-1B model created by Moorselaar [50]. The results from the algorithm on the baseline model show that the algorithm is not able to determine relationships that are in line with literature. This is caused by smearing, which is wrongfully attributing performance deviation caused by one component to another component. The modelling

error in the LPC and fan component is attributed to secondary performance parameter effects that influence the HPC, HPT and the LPT. It is concluded that the algorithm is not able to accurately separate residual modelling errors from the secondary performance parameter effects.

- **Validation of method using improved GEnx-1B model:** Further validation is performed using on-wing cruise data from the ESN956XXXA GEnx-1B engine and the improved GEnx-1B model, which has a modified fan and LPC component. The results from the algorithm with the improved GEnx-1B model display relationships between the secondary performance parameters and the component performance deviation that are in line with literature. Embedding these relationships in the improved GEnx-1B model reduced the modelling error to within a margin of 1%. The average modelling error is reduced by 65%.

- **Relationships from algorithm applied on other GEnx-1B engines:** The determined relationships are generated by the algorithm for ESN956XXXA engine data. These relationships were embedded in the improved GEnx-1B model. This model is tested using CEOD datasets from 5 different GEnx-1B engines with equal EGTMHD. For these engines, the deviation between on-wing data and model output is decreased to within a maximum of 2%. The average modelling error is reduced by 61%. It is concluded that accounting for the relationships also reduces modelling error when applied to data from different GEnx-1B engines.

- **GPA accounting for relationships:** Using the improved GEnx-1B model with the relationships embedded, a gas path analysis is performed on historical on-wing data and compared to GPA results from the model without embedded relationships. The GPA results from the GEnx-1B model with the embedded relationships better correspond with known engine history information such as water washes and a turbine blade failure. Also, the root mean square error of the GPA results, which is an indicator of the scatter, is decreased by 8%. It is concluded that accounting for the relationships increases GPA accuracy.

- **Main conclusion:** The main conclusion from this research is that the introduced algorithm can determine relationships between secondary performance parameters and component performance deviation that are in line with literature. Accounting for these relationships in engine models increases model accuracy for cruise conditions. Consequently, the gas path analysis accuracy is improved.

9.2. Recommendations

The algorithm has shown promising results. Still, improvements can be made. In this section, the recommendations for KLM ES and further research are listed.

- In this research, the assumption was made that the difference between the on-wing measurements and the GEnx-1B model output was mainly caused by the secondary performance parameters. This turned out to be an invalid assumption. For further validation of the algorithm, an engine model is required that does not contain additional modelling error.

- From the results of this thesis was concluded that the baseline GEnx-1B model does not accurately represent the cruise operating point. An analysis of the GEnx-1B model pointed out that this might be caused by the velocity coefficient in the nozzle being too low. However, further research should be performed to validate this claim.

- The objective function used in this thesis aims to decrease the deviation between on-wing measurements and model output. To increase the chance of the algorithm resulting in relationships that are in line with literature, multi-objective optimisation can be performed. By implementing an objective function that contains a penalty for a solution that is not in line with literature, better results might be obtained.

- For KLM ES it is advised to improve the GEnx-1B model's compressor maps. By verifying the physicality of implemented compressor maps, the model accuracy can be increased. For instance, component map tuning can be performed by taking compressor physics into account to make sure they are in line with physical behaviour.

- In this research, the algorithm is run on an engine that does not fully represent the engine new state. In the future, Performance Restoration Shop Visits will take place for the GEnx-1B engines. These engines

will better represent the new state of the GEnx-1B engine. This enables the algorithm to determine relationships that are not influenced by deterioration. Also, the algorithm could be run on a dataset created with data from various GEnx-1B engines. This could prevent overfitting on one engine altogether.

Bibliography

[1] P. A. Beishuizen. Improving Compressor Maps of the GE CF6-80C2 Engine. *MSc Thesis, Delft University of Technology*, 2012.

[2] G E Confidential. GEnx Engine Data Classification Overview GE Position on Rights to Operational and Proprietary Engine Data. pages 1–5, 2019.

[3] D. M. den Haan. GSP Gas Path Analysis on CF6-80 Engines at KLM Engine Services. *MSc Thesis, Delft University of Technology*, 2010.

[4] J. D. Denton. The 1993 IGTI Scholar Lecture: Loss Mechanisms in Turbomachines. *Journal of Turbomachinery*, 115(4):621–656, 1993. ISSN 0889-504X. doi: 10.1115/1.2929299.

[5] S L Dixon and C A Hall. *Fluid Mechanics and Thermodynamics of Turbomachinery Seventh Edition Library of Congress Cataloging-in-Publication Data*. 1978. ISBN 9780124159549.

[6] P. C. Escher. Pythia: An object-orientated gas path analysis computer program for general applications, 1995. URL `http://dspace.lib.cranfield.ac.uk/handle/1826/3457`.

[7] Alison B. Evans. The effects of compressor seventh-stage bleed air extraction on performance of the F100-PW-220 afterburning turbofan engine, 1991. URL `http://lb-primo.hosted.exlibrisgroup.com/primo_library/libweb/action/display.do?tabs=detailsTab&ct=display&fn=search&doc=TN_nasa119910010772&indx=1&recIds=TN_nasa119910010772&recIdxs=0&elementId=0&renderMode=poppedOut&displayMode=full&frbrVersion=&dscnt=0`.

[8] GE Aviation. Datasheet GEnx. Technical report, 2004. URL `https://www.geaviation.com/sites/default/files/datasheet-genx.pdf`.

[9] GE Aviation. GEnx-1B Turbofan Engine Installation Manual. 2018.

[10] GE Aviation. GEnx-1B Engine Manual. 2021.

[11] T.U.J. Grönstedt. Identifiability in multi-point gas turbine parameter estimation problems. *Proceedings of ASME Turbo EXPO 2002*, pages 1–9, 2002.

[12] D M Den Haan. Introduction to Gas Turbine Performance and Gas Path Analysis. 2009.

[13] R. Hackney, T. Nikolaidis, and A. Pellegrini. A method for modelling compressor bleed in gas turbine analysis software. *Applied Thermal Engineering*, 2020. doi: 10.1016/j.applthermaleng.2020.115087.

[14] Karel Hajmrle, Petr Fiala, Anthony P. Chilkowich, and Lawrence T. Shiembob. Abradable seals for gas turbines and other rotary equipment. *Proceedings of the ASME Turbo Expo 2004*, 4:673–682, 2004. doi: 10.1115/gt2004-53865.

[15] Donald E. Holeski. Effect of rotor tip clearance on the performance of a 5-inch single-stage axial-flow turbine. 1966.

[16] Robert Holmes. The origin of species. *Economist (United Kingdom)*, 412(8974), 2016. ISSN 00130613. doi: 10.7312/bird12662-005.

[17] ITU-R. Reference standard atmospheres P Series Radiowave propagation. *Recommendation ITU-R P.835-6*, 5, 2012.

[18] Joachim Kurzke. *Propulsion and Power Subsystems*. Number September. 2018. ISBN 9783319759777.

[19] Manoj Kumar, Mohamed Husain, Naveen Upreti, and Deepti Gupta. Genetic Algorithm: Review and Application. *SSRN Electronic Journal*, 2(2):451–454, 2020. ISSN 1556-5068. doi: 10.2139/ssrn.3529843.

[20] R. Kurz and K. Brun. Degradation of gas turbine performance in natural gas service. *Journal of Natural Gas Science and Engineering*, 1(3):95–102, 2009. doi: 10.1016/j.jngse.2009.03.007.

[21] R. Kurz, K. Brun, and M. Wollie. Degradation effects on industrial gas turbines. *Journal of Engineering for Gas Turbines and Power*, 131(6):1–7, 2009. doi: 10.1115/1.3097135.

[22] Rainer Kurz. Gas Turbine Degradation. *43rd Turbomachinery & 30th Pump Users Symposia*, pages 1–36, 2014.

[23] Rainer Kurz and Klaus Brun. Fouling mechanisms in axial compressors. *Journal of Engineering for Gas Turbines and Power*, 134(3), 2012. ISSN 07424795. doi: 10.1115/1.4004403.

[24] Brun K. Kurz R. Degradation in gas turbine systems. *Journal of Engineering for Gas Turbines and Power*, 123(1):70–77, 2001. ISSN 07424795. doi: 10.1115/1.1340629.

[25] J. Kurzke. Calculation of installation effects within performance computer programs. *Advisory Group for Aerospace Research and Development*, 114(May):1–7, 1992.

[26] J. Kurzke. How to get component maps for aircraft gas turbine performance calculations. *American Society of Mechanical Engineers 1996 International Gas Turbine and Aeroengine Congress and Exhibition*, 5, 1996. doi: 10.1115/96-GT-164.

[27] Joachim Kurzke. About simplifications in gas turbine performance calculations. *Proceedings of the ASME Turbo Expo*, 3:493–501, 2007. doi: 10.1115/GT2007-27620.

[28] Joachim Kurzke. Effects of inlet flow distortion on the performance of aircraft gas turbines. *Journal of Engineering for Gas Turbines and Power*, 130(4), 2008. ISSN 07424795. doi: 10.1115/1.2901190.

[29] Joachim Kurzke and Ian Halliwell. *Propulsion and Power: An Exploration of Gas Turbine Performance Modeling*. Number January. 2018. ISBN 9783319759791. doi: 10.1007/978-3-319-75979-1.

[30] B. Lambiris, K. Mathioudakis, A. Stamatis, and K. Papailiou. Adaptive modeling of jet engine performance with application to condition monitoring. *Journal of Propulsion and Power*, 10(6):890–896, 1994. doi: 10.2514/3.23828.

[31] Scott B. Lattime and Bruce M. Steinetz. High-Pressure-Turbine Clearance Control Systems: Current Practices and Future Directions. *Journal of Propulsion and Power*, 20(2):302–311, 2004. ISSN 15333876. doi: 10.2514/1.9255.

[32] L. Marinai, D. Probert, and R. Singh. Prospects for aero gas-turbine diagnostics: A review. *Applied Energy*, 79(1):109–126, 2004. doi: 10.1016/j.apenergy.2003.10.005.

[33] R. Nicoara, V. Vilag, J. Vilag, and Z. Kolozvary. Axial Turbine Performance Estimation During Dynamic Operations. *International Journal of Aeronautical and Space Sciences*, 2020. doi: 10.1007/s42405-020-00312-4.

[34] M Otten. Introduction to engine condition monitoring using gas path analysis. 2021.

[35] H. Pieters. Gas Path Analysis with GSP for the GEM42 turboshaft engine. *MSc Thesis, Delft University of Technology*, 2005.

[36] B. Röell. Performance Comparison at KLM Engine Services Test-cell & On-wing Turbofan Performance Comparison at KLM Engine Services. *MSc Thesis, Delft University of Technology*, 2019.

[37] T.O. Rootliep. Turbofan Condition Monitoring using Evolutionary Algorithm based Gas Path Analysis at KLM Engine Services Turbofan Condition Monitoring using Evolutionary Algorithm based Gas Path Analysis. *MSc Thesis, Delft University of Technology*, 2020.

[38] RTO-TR-AVT-036. *Performance Prediction and Simulation of Gas Turbine Engine Operation for Aircraft, Marine, Vehicular, and Power Generation*, volume 323. 2007. ISBN 9789283700616.

[39] Suresh Sampath, Stephen Ogaji, Riti Singh, and Douglas Probert. Engine-fault diagnostics: An optimisation procedure. *Applied Energy*, 73(1):47–70, 2002. ISSN 03062619. doi: 10.1016/S0306-2619(02)00051-X.

[40] H.I.H. Saravanamuttoo, H. Cohen, G. F. C. Rogers, A.C. Nix, and P. V. Straznicky. *Gas Turbine Theory*. 2017. ISBN 9781292093093.

[41] A. Schäffler. Experimental and analytical investigation of the effects of reynolds number and blade surface roughness on multistage axial flow compressors. *Journal of Engineering for Gas Turbines and Power*, 102(1):5–12, 1980. ISSN 15288919. doi: 10.1115/1.3230232.

[42] U.W. Schaub, E. Vlasic, and S.H. Moustapha. Effect of tip clearance on the performance of a highly loaded turbine stage. *Advisory Group for Aerospace Research and Development*, (October 1993):Paper 29, 1993.

[43] David J. Smith. Power-by-the-hour: The role of technology in reshaping business strategy at Rolls-Royce. *Technology Analysis and Strategic Management*, 25(8):987–1007, 2013. ISSN 09537325. doi: 10.1080/09537325.2013.823147.

[44] Z. S. Spakovszky, J. B. Gertz, O. P. Sharma, J. D. Paduano, A. H. Epstein, and E. M. Greitzer. Influence of compressor deterioration on engine dynamic behavior and transient stall-margin. *Proceedings of the ASME Turbo Expo*, 1(99), 1999. doi: 10.1115/99-GT-439.

[45] A. Stamatis. Jet Engine Fault Detection with Discrete Operating Points Gas Path Analysis. *Aircraft Engineering and Aerospace Technology*, 68(2):3–9, 1996. ISSN 00022667. doi: 10.1108/eb037626.

[46] R. Storn and K. Price. Differential Evolution – A Simple and Efficient Heuristic for Global Optimization over Continuous Spaces RAINER. *journal of global optimization*, pages 341–359, 1997. ISSN 08153191.

[47] GSP Development Team. GSP 11 User Manual. 2016. URL `http://www.gspteam.com/Files/manuals/UM/GSP_UM_11.pdf`.

[48] L.A. Urban. Gas path analysis applied to turbine engine condition monitoring. *Journal of Aircraft*, 10(7):400–406, 1973. ISSN 00218669. doi: 10.2514/3.60240.

[49] E. van Dorp. Development and implementation of a GSP gas path analysis tool for gas turbine diagnostics. *MSc Thesis, Delft University of Technology*, (August), 2009.

[50] M. P. R. van Moorselaar. Gas Path Analysis on the GEnx-1B at KLM Engine Services. *MSc Thesis, Delft University of Technology*, page 113, 2018.

[51] S. van Vuuren. Humidity Effects on Turbofan Performance in a MRO context. *MSc Thesis, Delft University of Technology*, 2019.

[52] M.L. Verbist. *Gas path analysis for enhanced aero-engine condition monitoring and maintenance*. PhD thesis, Delft University of Technology, 2017.

[53] M.L. Verbist, R. Pecnik, and J.P. van Buijtenen. Component map tuning procedure using adaptive modeling. *Proceedings of ASME Turbo Expo 2012*, pages 1–9, 2012.

[54] W.P.J. Visser. *Generic Analysis Methods for Gas Turbine Engine Performance*. PhD thesis, 2015.

[55] W.P.J. Visser, O. Kogenhop, and M. Oostveen. A generic approach for gas turbine adaptive modeling. *Journal of Engineering for Gas Turbines and Power*, 128(1):13–19, 2006. ISSN 07424795. doi: 10.1115/1.1995770.

[56] A.J. Volponi. Gas turbine engine health management: Past, present, and future trends. *Journal of Engineering for Gas Turbines and Power*, 136(5):1–20, 2014. doi: 10.1115/1.4026126.

[57] Allan J. Volponi. *Gas turbine parameter corrections*. 2020. ISBN 9783030410766. doi: 10.1007/978-3-030-41076-6.

[58] P.P. Walsh. *Gas turbine performance*. Blackwell Science, 2004.

[59] Piero Colonna William C. Reynolds. *Thermodynamics Fundamentals and Engineering Application*. Number 9. 2018. ISBN 9788578110796.

[60] William C. Reynolds; Piero Colonna. *Thermodynamics: fundamentals and engineering applications*, volume 53. Cambridge University Press, 2018. ISBN 9780521862738.

[61] Jinguang Yang, Min Zhang, Cheng Peng, Michele Ferlauto, and Yan Liu. Stator re-stagger optimization in multistage axial compressor. *Propulsion and Power Research*, 10(2):107–117, 2021. ISSN 2212540X. doi: 10.1016/j.jppr.2021.03.002. URL https://doi.org/10.1016/j.jppr.2021.03.002.

[62] Y.G.Li. Performance-analysis-based gas turbine diagnostics. *Journal of power and energy*, (April):363–377, 2002.

[63] S. Yoon, E. Curtis, J. Denton, and J. Longley. The effect of clearance on shrouded and unshrouded turbines at two levels of reaction. *Journal of Turbomachinery*, 136(2):1–9, 2013. doi: 10.1115/1.4023942.

[64] M. Zedda and R. Singh. Gas turbine engine and sensor fault diagnosis using optimisation techniques. *35th Joint Propulsion Conference and Exhibit*, 18(5), 1999. doi: 10.2514/6.1999-2530.

Appendices

A

Gas path analysis on next-generation turbofan engines at KLM ES

MSc Assignment for Michiel Ottens, Propulsion Power (FPP), Faculty of Aerospace Engineering

Introduction

KLM Engine Services (ES) is part of Air France Industries KLM Engineering Maintenance Group, overhauling approximately 200 aircraft engines annually. The overhaul shop visit ends with a standardized performance test, to assess compliance to certification rules and customer contracts, before it is released for operation on-wing. At two different locations, the following turbofan engine types are tested:

- CFM56-7B KLM EM Testcell / Schiphol-Oost
- CF6-80E1 KLM EM Testcell / Schiphol-Oost
- CF6-80C2 KLM EM Testcell / Schiphol-Oost
- GEnx-1B Zephyr Testcell / Charles de Gaulle Airport, Paris
- CFMI LEAP-1A -1B (in gradual introduction)

Over the years KLM ES Engineering has used GSP (Gas turbine Simulation Program) as a supporting tool to analyze and evaluate engine performance data. Gas Path Analysis (GPA) techniques are used to translate engine performance data into component condition information. For optimal performance analysis accuracy, parameter inputs from all gas path sensors at the various engine stations are required. With new engine types such as the GEnx and the LEAP, the OEM does no longer provide the ability to install the additional sensors at the various engine stations, hence data input is limited, resulting in reduced potential to accurately analyze performance. This issue has been overcome by implementing a Multiple Operating Point Analysis (MOPA) in a GSP performance model, solved with a Evolutionary Algorithm (EA) optimizing routine.

The other feature that distinguishes next-generation turbofan engines from their older counterparts is the introduction of Continuous Engine Operating Data (CEOD). CEOD include data required for detailed analysis of in-flight engine performance. By selecting specific points representing operating conditions suitable for accurate performance and GPA analysis, accurate assessment of engine component health can be made.

The objective of the assignment is to develop the MOPA-EA method into an on-wing condition monitoring tool for the GEnx-1B engine to be used for work scope decision support.

Key objectives

- Develop a system that automatically extracts and processes CEOD data for MOPA-EA.
- Improve the hybrid MOPA-EA GPA tool to decrease runtime and increase component health assessment accuracy.

Assignment

Your work will include the following elements:

1. A literature study on turbofan engine performance modelling and test analysis, including GPA with reduced number of measured of parameters.
2. Introduction to current KLM performance and EGTM condition monitoring practice and relation to the maintenance concept.
3. Introduction to GSP (test analysis and gas path analysis models) as applied to KLM engines.
4. Familiarization with current MOPA-EA GPA tool.
5. Develop a concept how to integrate the tool into the maintenance process as a work scope decision support tool.

Report

Results of the work must be reported in English, with a copy of this assignment and an executive summary.

Coaching

The work will be performed in close collaboration with KLM Engine Services (Michel Nollet/Juan Regueiro)
Date 19 November 2019

Professor,	Delft University supervisor,	Supervisor at KLM
Prof. dr. ir. P. Colonna	Dr. ir. W.P.J. Visser	Juan Regueiro

B

Thermodynamics of gas turbine theory

In this appendix, the theoretical framework for this research is introduced. First, the ideal Joule-Brayton cycle and its corresponding thermodynamic laws are discussed. Secondly, the real Joule-Brayton cycle is explained. Lastly, the modelling and calculation methods for design point are given.

B.1. Ideal Joule-Brayton cycle

As introduced in chapter 2, the gas turbine works following the ideal Joule-Brayton cycle. These steps can also be visualised in an h-s diagram as in Figure B.1.

- Step 0-2 Ideal expansion in the inlet.
- Step 2-3 Isentropic compression in the compressor.
- Step 3-4 Isobaric heat addition in the combustor.
- Step 4-gg Isentropic expansion in the turbine.
- Step 5-0 Isobaric heat rejection from the nozzle.

For this ideal cycle the following assumptions are made:

1. The airflow through the gas turbine is a perfect gas.
2. The compression and expansion process is adiabatic and reversible.
3. No pressure loss occurs in the ducting, inlet, combustion chamber and nozzle.
4. Kinetic energy changes between the components can be neglected.

As is visible in Figure B.1, the compression and expansion is isentropic. The gg point in the graph is denoting the location in the turbine at which all the work needed to drive the compressor, is extracted. To calculate the properties of temperature and pressure throughout the gas turbine, fundamental laws of thermodynamics are introduced in the following section.

B.2. Fundamental laws

To theoretical framework of turbomachinery is based on basic physical laws of fluid mechanics and thermodynamics. The introduction of these laws is necessary to derive relations between the various components in the gas turbine. The following laws and equations will be discussed:

- The continuity equation
- The first law of thermodynamics
- The second law of thermodynamics

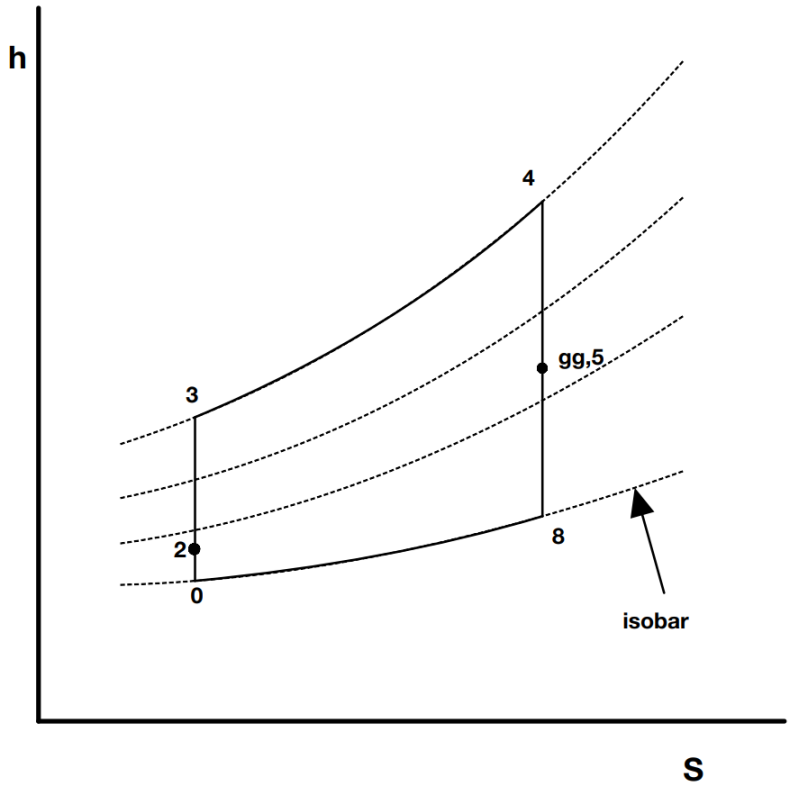

Figure B.1: Entropy-enthalpy graph of a gas turbine

B.2.1. The continuity equation

The continuity equation states that the rate of the mass that flows into the system is equal to the rate at which mass leaves the system plus the rate of mass accumulation in the system. This law is visible in Equation B.1, in which c is the velocity, $\dot{m}$ is the mass flow rate, ρ the density and A_n the area perpendicular to the flow direction. With regards to steady-state turbomachinery, this equation can be rewritten to Equation B.2 because no accumulation of mass occurs in the individual components and the control volumes are often ducts or passages. In this equation, the subscripts 1 and 2 denote the inlet and outlet of the component.

$$\mathrm{d}\dot{m} = \frac{\mathrm{d}m}{\mathrm{d}t} = \rho c d A_n \tag{B.1}$$

$$\dot{m} = \rho_1 c_1 A_{n1} = \rho_2 c_2 A_{n2} \tag{B.2}$$

B.2.2. The first law of thermodynamics

The first law of thermodynamics states that energy can neither be created nor destroyed[59]. In the case of a gas turbine, this law can be applied to form the steady flow energy equation visible in Equation B.3 [5].

$$\dot{Q} - \dot{W} = \dot{m}\left[(h_2 - h_1) + \frac{1}{2}\left(c_2^2 - c_1^2\right)\right] \tag{B.3}$$

This equation can be further simplified by using the total enthalpy. The total enthalpy is the combination of the specific enthalpy and the kinetic energy given in Equation B.4. This results in Equation B.8. Since for a perfect gas, the c_p does not vary with temperature, the total enthalpy can also be given as in Equation B.5. The use of working with total properties is that the kinetic energy in the flow can be taken into account by forcing the flow to stagnation adiabatically. Using this result, properties in gas turbines can be measured by pitot tubes and the flow velocity can be taken into account without measuring it. This same analogy holds for the total temperature and pressure visible in Equation B.6 and Equation B.7 respectively.

$$h_0 = h + \frac{1}{2}c^2 \tag{B.4}$$

$$h_0 = c_p \cdot T_0 = h + \frac{1}{2}c^2 \tag{B.5}$$

$$T_0 = T + c^2/2c_p \tag{B.6}$$

$$\frac{p_0}{p} = \left(\frac{T_0}{T}\right)^{\gamma/(\gamma-1)} \tag{B.7}$$

Consequently, Equation B.3 can be rewritten as Equation B.8. Because the property calculations for various gas turbine components can be derived from it, this relation is of great importance for turbomachinery analysis.

$$Q - W = (h_{02} - h_{01}) = c_p\,(T_{02} - T_{01}) \tag{B.8}$$

For a component which causes an adiabatic compression, $Q = 0$ and Equation B.9 is applicable.

$$W = -c_p\,(T_{02} - T_{01}) \tag{B.9}$$

Similarly for a component in which heat is added and no work is done, $W = 0$ and Equation B.10 is applicable.

$$Q = c_p\,(T_{02} - T_{01}) \tag{B.10}$$

Also Equation B.7 can be used to derive the relation for an isentropic compression between the inlet and outlet of a component by using Equation B.11

$$\frac{p_{02}}{p_{01}} = \left(\frac{T_{02}}{T_{01}}\right)^{\gamma/(\gamma-1)} \tag{B.11}$$

These relation described are relations for isentropic processes. However, in practice, the behaviour of components is not ideal. The second law of thermodynamics deals with this matter and is introduced in the subsequent section.

B.2.3. Second law of thermodynamics

The second law of thermodynamics deals with entropy. Entropy is described as a measure of the microscopic randomization, disorder and unpredictability of a certain medium [60]. Contrary to ideal processes which are isentropic, in real processes entropy is generated. Entropy production can never be negative. The entropy generated in gas turbines can be seen as a loss of energy available to do work. The quantity of entropy generated relative to the potential ideal energy can be described by efficiencies of gas turbine components. The following section will deal with the calculation of the real cycle.

B.3. Real cycle

To relate the ideal thermodynamic process to actual performance, isentropic efficiencies are defined. By means of these efficiencies, the ideal equations from section B.2 can be adapted to be applied on real thermodynamic cycles. Apart from the thermodynamic efficiencies, several other efficiencies are of importance for gas turbine cycle calculations. The other considered efficiencies are:

- Combustion efficiency
- Mechanical efficiency
- inlet efficiency
- Nozzle efficiency

Besides the efficiencies, the real cycle also works with a non-ideal gas. Although it behaves close to ideal, the C_p and γ value vary with gas composition, pressure and temperature for a non-ideal gas. Often these are assumed constant, as is done for the following real cycle analysis.

B.3.1. Isentropic efficiency

As states in subsection B.2.3, real thermodynamic processes are inherent to entropy generation and are therefore not isentropic. The extent to which these processes are not isentropic is determined by the ratio between actual work and ideal work, also called isentropic efficiency. For the compressor and turbine, these equations are defined as follows.

For the compressor, the isentropic efficiency is defined as in Equation B.12 and Equation B.13.

$$\eta_{comp} = \frac{T'_{02} - T_{01}}{T_{02} - T_{01}} \tag{B.12}$$

$$\eta_{is,comp} = \frac{\left(\frac{p_{02}}{p_{01}}\right)^{\frac{\gamma-1}{\gamma}} - 1}{\frac{T_{02}}{T_{01}} - 1} \tag{B.13}$$

For the compressor, the isentropic efficiency is defined as in Equation B.14 and Equation B.15.

$$\eta_{turb} = \frac{W}{W'} = \frac{T_{03} - T_{04}}{T_{03} - T'_{04}} \tag{B.14}$$

$$\eta_{is,turb} = \frac{1 - \frac{T_{04}}{T_{03}}}{1 - \left(\frac{p_{04}}{p_{03}}\right)^{\frac{\gamma-1}{\gamma}}} \tag{B.15}$$

B.3.2. Combustor efficiency

The last relevant thermodynamic efficiency for gas turbine modelling is the combustor efficiency. The combustor efficiency is defined as the actual extracted energy over the maximum potential energy available in the fuel. This efficiency can be calculated following Equation B.16 in which LHV is the lower heating value of the fuel. $\dot{m}_f$ is the fuel mass flow and $\dot{m}$ is the air mass flow.

$$\eta_{cc} = \frac{\dot{m} \cdot c_{p_{gas}} \left(T_{0,4} - T_{0,3}\right)}{m_f \cdot LHV_f} \tag{B.16}$$

B.3.3. Mechanical efficiency

Since the compressor and turbine are mechanically coupled by a shaft, there is a mechanical loss present in the form of a bearing friction loss.

$$\eta_{\text{mech}} = \frac{c_p(T_{02} - T_{01})}{W_{\text{turb}}} \tag{B.17}$$

B.3.4. Inlet efficiency

The inlet of a turbofan engine is a slightly diverging duct to decrease the Mach number at the fan face below M=0.6 and increase the pressure. Since the aircraft is moving at a certain velocity, the ambient air can be seen relative to the airplane as approaching the aircraft with a certain Mach number. Recalling Equation B.6, Equation B.7, and the isentropic efficiency of the inlet Equation B.18, Equation B.19 can be constructed in which T'_{01} is the temperature that would be reached in case of isentropic compression.

$$\eta_i = \frac{T'_{01} - T_{amb}}{T_{01} - T_{amb}} \tag{B.18}$$

$$T'_{01} - T_{amb} = \eta_i \frac{c^2_{amb}}{2c_p} \tag{B.19}$$

With the fact that $M = c/(c_p(\gamma-1)T)^{1/2}$ this equation can be rewritten as a function of the flight mach number in Equation B.20.

$$\frac{p_{01}}{p_{amb}} = \left[1 + \eta_i \frac{\gamma-1}{2} M^2_{amb}\right]^{\gamma/(\gamma-1)} \tag{B.20}$$

B.3.5. Nozzle efficiency

For the calculations regarding the nozzle, two variants are available. For the case of an unchocked and choked nozzle. For both cases, an equation will be given. To determine if the nozzle is choked, Equation B.21 is established. If this equation surpasses the value of the critical pressure ratio, the nozzle is choked. If not, the nozzle is not choked and the flow can expand to the ambient pressure.

$$critical\ pressure\ ratio = \frac{p_{07}}{p_{\text{critical}}} = \left[1 - \frac{1}{\eta_j}\left(\frac{\gamma-1}{\gamma+1}\right)\right]^{\left(\frac{-\gamma}{\gamma-1}\right)} \tag{B.21}$$

Unchoked

As stated, the unchoked nozzle results in an outlet pressure that is equal to the ambient pressure. For the outlet temperature, Equation B.22 can be used. In which η_j is defined as in Equation B.23.

$$\frac{T_{\text{in}}}{T_{\text{out}}} = \frac{1}{1-\eta_j\left(1-\frac{p_{\text{amb}}}{p_{07}}\frac{\gamma-1}{\gamma}\right)} \tag{B.22}$$

$$\eta_j = \frac{T_{07}-T_{08}}{T_{07}-T'_{08}} \tag{B.23}$$

Choked

For a choked nozzle, the pressure ratio is constrained by the critical pressure ratio, and the temperature by the critical temperature ratio. Since the Mach number is equal to 1 in the throat of the nozzle, the mass flow can not be increased by decreasing the ambient pressure. The relation for the critical temperature ratio is given in Equation B.24.

$$TR_{\text{crit}} = \frac{T_{0in}}{T_{crit}} = \frac{\gamma+1}{2} \tag{B.24}$$

The relation for the critical pressure for a choked nozzle is defined as in Equation B.21.

With these relations, a real cycle design point calculation can be performed. The following section describes the calculation scheme.

B.4. Real cycle design point calculation

In this section, a real engine design point calculation is performed by making use of the above-mentioned equations. A design point is a region for which the gas turbine is designed and will operate the majority of its lifespan. Since the real cycle incorporates efficiencies, the h-S diagram of the Joule-Brayton cycle is also different from the ideal cycle diagram. The real cycle diagram is visible in Figure B.2.

In Figure B.2, station numbers are used. These station numbers are defined as in Figure B.3 and Table B.1. This follows the standard ARP engine station numbering and nomenclature [58]. This standard will be used throughout this whole research to indicate the station numbers for high bypass gas turbines. In the following section, an design point engine calculation is performed from inlet to outlet.

Station number	Station	Station number	Station
2	Fan hub inlet	4	Combustor outlet
12	Fan tip inlet	49	HPT outlet
21	LPC inlet	18	Bypass Nozzle throat
14	Bypass stream	5	LPT outlet
25	HPC inlet	7	Core nozzle inlet
3	HPC outlet	8	Core nozzle throat

Table B.1: Standard ARP engine station numbering [58]

B.4.1. Inlet

The first component the air passes through is the inlet, to calculate the total pressure and temperature in the inlet, Equation B.20 and Equation B.18 are used respectively. This means that the ambient conditions, efficiencies and flight Mach number are inputs for the calculation.

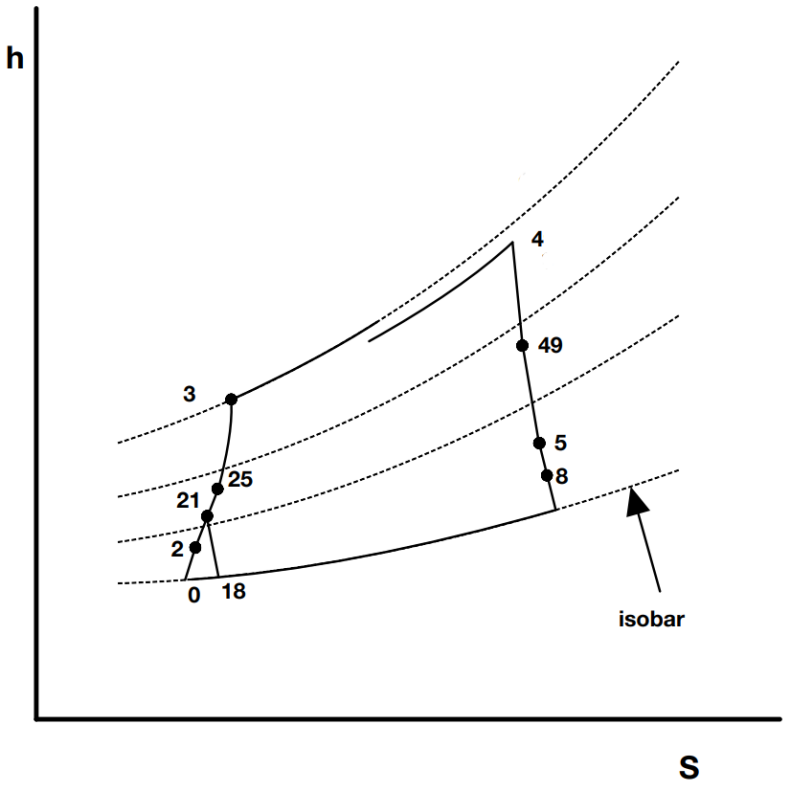

Figure B.2: Entropy-specific enthalpy graph of a real gas turbine cycle

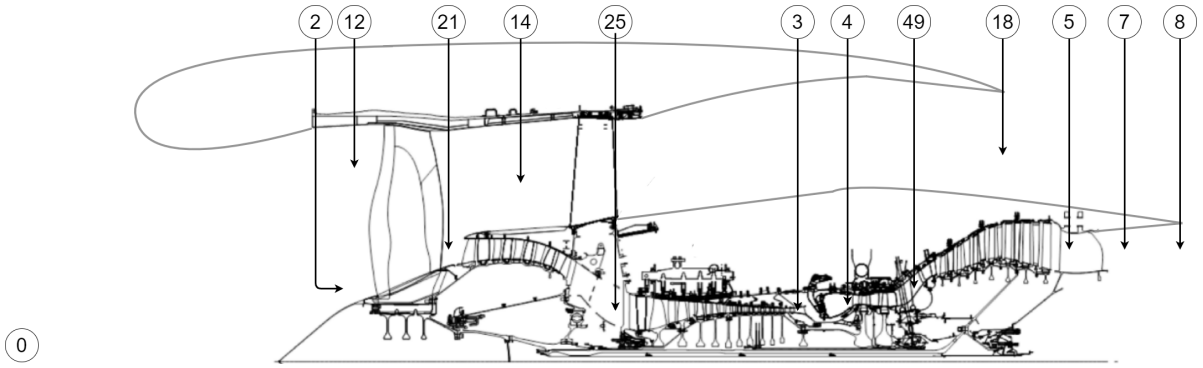

Figure B.3: GEnx-1B station numbering [9]

B.4.2. Fan, low-pressure and high-pressure compressor

The fan, low-pressure and high-pressure compressor all work as a compressor and therefore the relation between the inlet and outlet pressure is given by the pressure ratio. The pressure ratio is often defined for these turbomachinery components. From the given pressure ratios and efficiencies, the total temperature ratios over these components can be calculated using Equation B.13. For this equation, the input isentropic efficiency is defined.
Right behind the fan, the airflow is divided into the bypass flow and core flow. The relation between the bypass ratio and the mass flows is given by Equation B.25.

$$BPR = \frac{\dot{m}_{bypass}}{\dot{m}_{core}} \tag{B.25}$$

B.4.3. Combustor

The combustor is modelled by using the relation given in Equation B.16, for which the combustor efficiency is given. In the combustor, pressure losses also occur. These pressure losses are defined as in Equation B.26, in which the pressure ratio is defined.

$$p_{t,4} = PR_{combustor} * p_{t,3} \tag{B.26}$$

B.4.4. Low-pressure and high-pressure turbine

The calculated properties at the outlet of the low and high-pressure turbine are determined based on the work performed in the compressors. The fan and low-pressure compressor are coupled via the N1 axis, to the low-pressure turbine. Also the high-pressure compressor is coupled to the high-pressure turbine via the N2 axis. The energy extracted in the turbines multiplied by the mechanical efficiency is equal to the work performed in the compressors and fan. This relation is given in Equation B.17. By using the relation from Equation B.15, the outlet pressure of the components can also be calculated. Note that the isentropic efficiency is an input to the calculation.

B.4.5. Nozzles

The last station at which the air exits the gas turbine is the nozzle. For both the core and bypass nozzle, the chocked and unchoked case exist. These scenarios are discussed below. The criteria for which the flow is chocked is given in Equation B.21. The resulting thrust that the gas turbine generates is given in Equation B.27.

$$F_N = F_{\text{core}} + F_{\text{bypass}} \tag{B.27}$$

Unchoked

For the unchoked scenario, the thrust for the core and the bypass nozzle is given by Equation B.28 and Equation B.29 respectively. The temperature of the exit flow is determined by Equation B.22 and the pressure is determined by the ambient pressure. By using the outlet temperature, the outlet v_8 and v_{18} can be calculated to perform the real thrust computation. To approximate the boundary layer losses in the nozzles, a nozzle isentropic efficiency is used.

$$F_{\text{core}} = \dot{m}_{core}\,(v_8 - v_\infty) \tag{B.28}$$

$$F_{\text{bypass}} = \dot{m}_{bypass}\,(v_{18} - v_\infty) \tag{B.29}$$

Choked

In the choked scenario, the nozzle flow can not fully expand and the thrust equation includes a pressure component. The temperature of the exit flow is determined by Equation B.24 and the pressure is determined by the critical pressure ratio as in Equation B.21 in which the nozzle losses are included. Using the equation for the speed of sound from Equation B.32 the nozzle exit velocity can be calculated.

$$F_{\text{core}} = \dot{m}_{core}\,(v_8 - v_\infty) + A_8\left(p_8 - p_a\right) \tag{B.30}$$

$$F_{\text{bypass}} = \dot{m}_{bypass}\,(v_{18} - v_\infty) + A_{18}\left(p_{18} - p_a\right) \tag{B.31}$$

$$v_{nozzle\ exit} = \sqrt{\gamma_g R T_{nozzle\ exit}} \tag{B.32}$$

Combining the by using the conservation equation of mass and the perfect gas law, the pressure thrust component can be determined following Equation B.33, Equation B.34 and finally Equation B.30. This concludes the cycle calculation.

$$\rho_8 = \frac{p_8}{R \cdot T_8} \tag{B.33}$$

$$A_8 = \frac{\dot{m}}{\rho_8 v_8} \tag{B.34}$$

C

Additional figures methodology

C.1. Results reduced sensors

In this appendix, the additional results from the proof of concept are displayed.

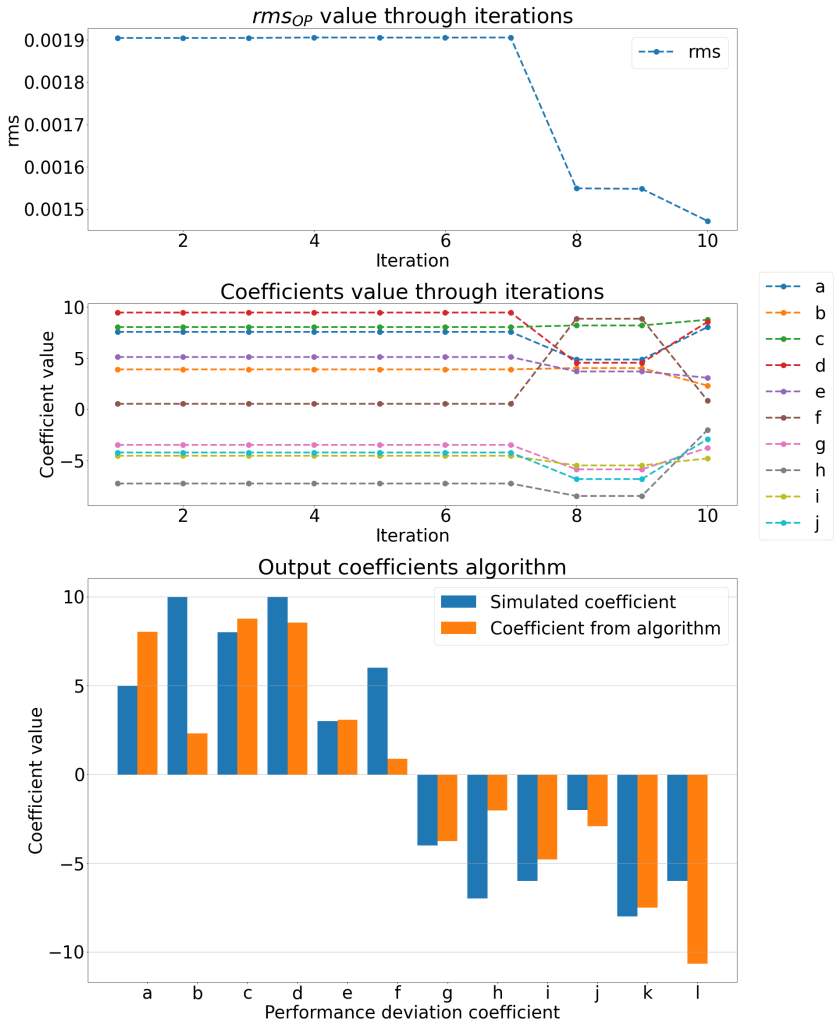

Figure C.1: Results from simulation with reduced sensors

C.2. Results noise methodology

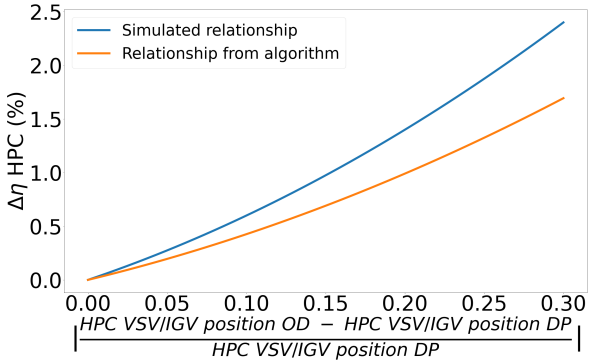

(a) $\Delta\eta$ vs HPC IGV/VSV relationships

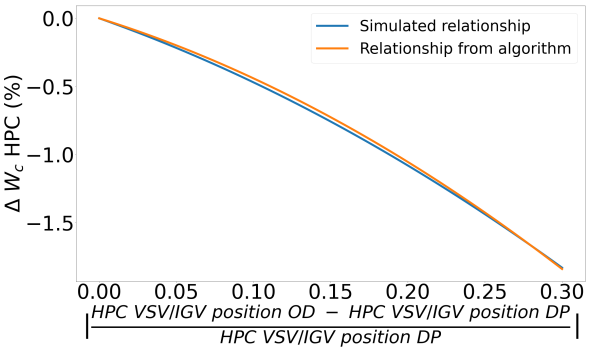

(b) ΔW_c vs HPC IGV/VSV relationships

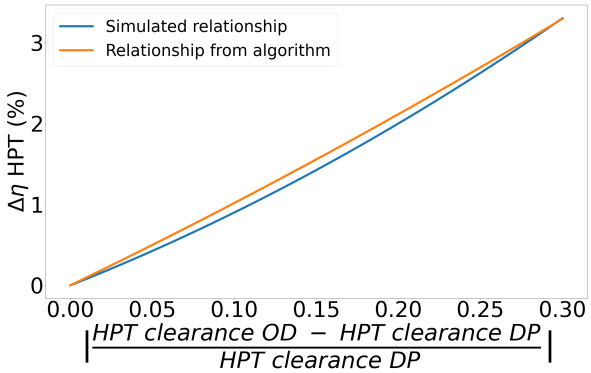

(c) $\Delta\eta$ vs HPT clearance relationships

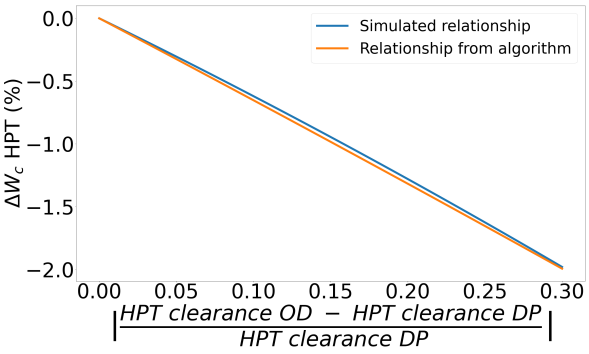

(d) ΔW_c vs HPT clearance relationships

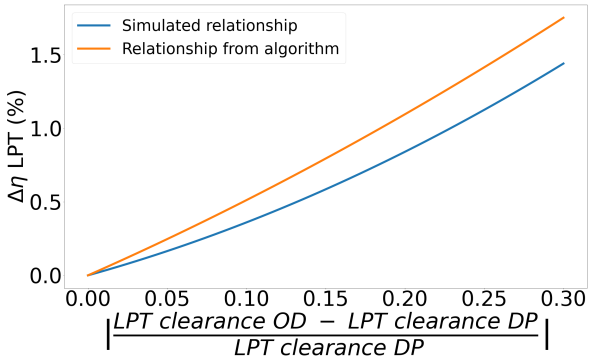

(e) $\Delta\eta$ vs LPT clearance relationships

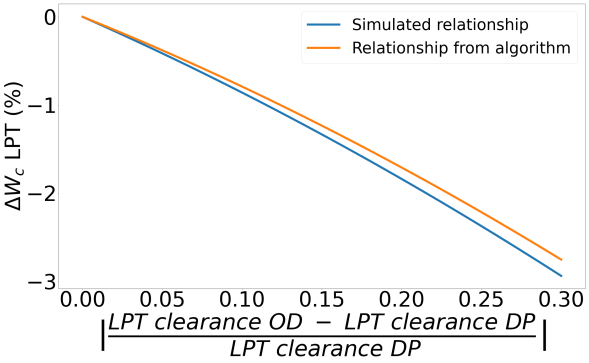

(f) ΔW_c vs LPT clearance relationships

Figure C.2: Simulated relationships vs relationships from algorithm with noise

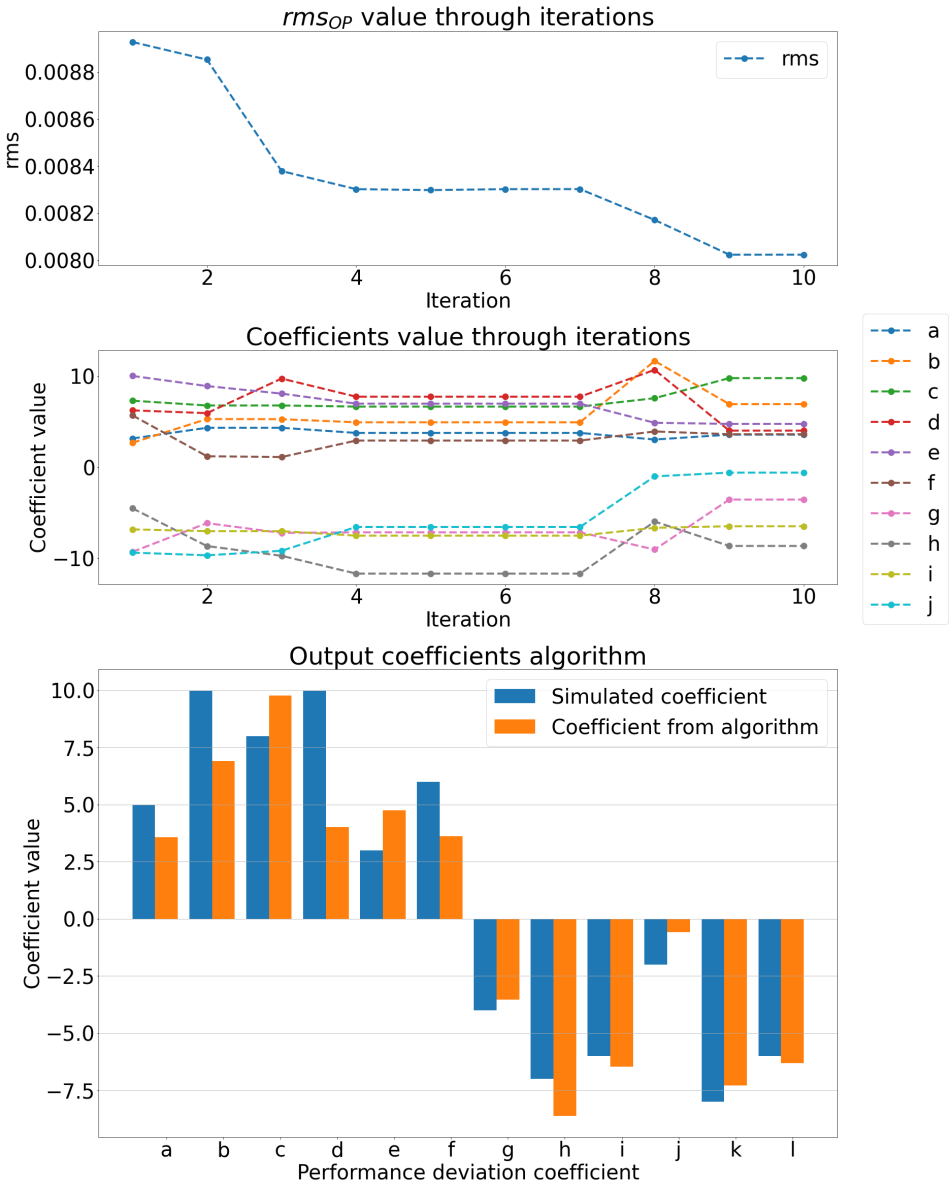

Figure C.3: Results from simulation with noise

C.3. Bounded results methodology

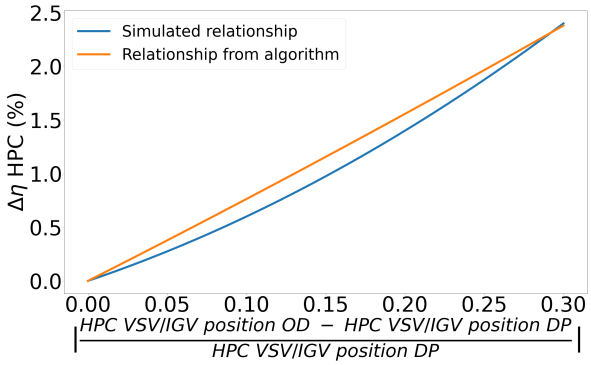

(a) $\Delta\eta$ vs HPC IGV/VSV relationships

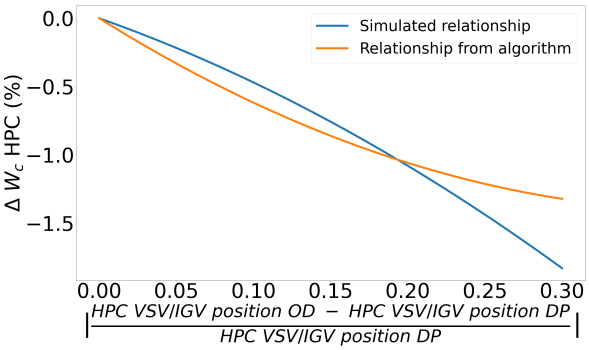

(b) ΔW_c vs HPC IGV/VSV relationships

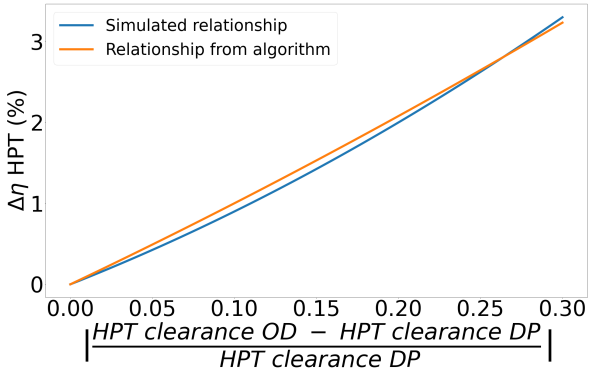

(c) $\Delta\eta$ vs HPT clearance relationships

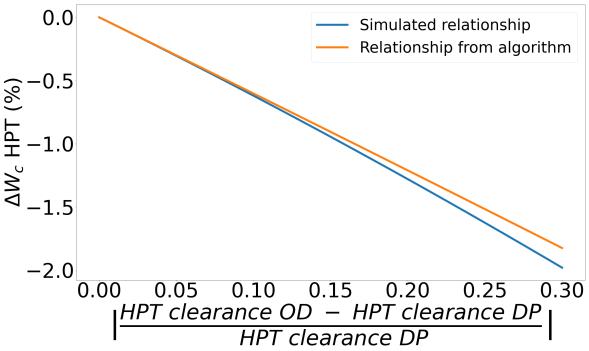

(d) ΔW_c vs HPT clearance relationships

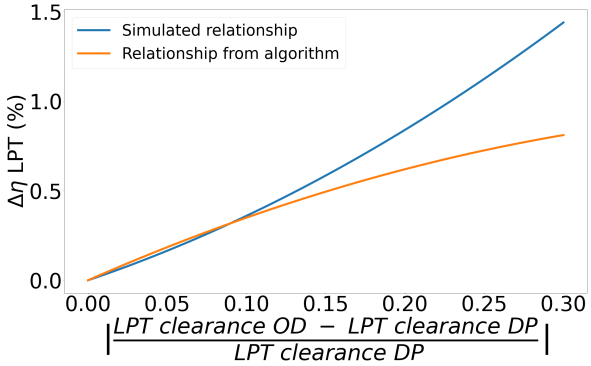

(e) $\Delta\eta$ vs LPT clearance relationships

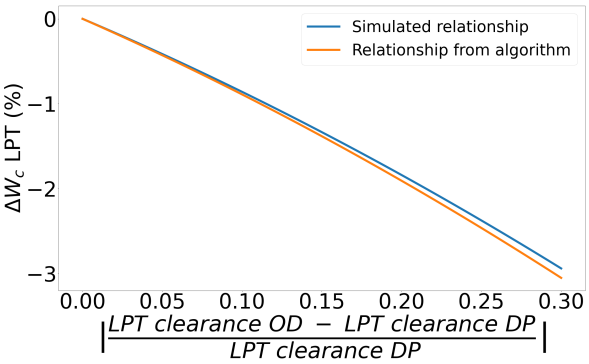

(f) ΔW_c vs LPT clearance relationships

Figure C.4: Simulated relationships vs relationships from algorithm with larger bounds

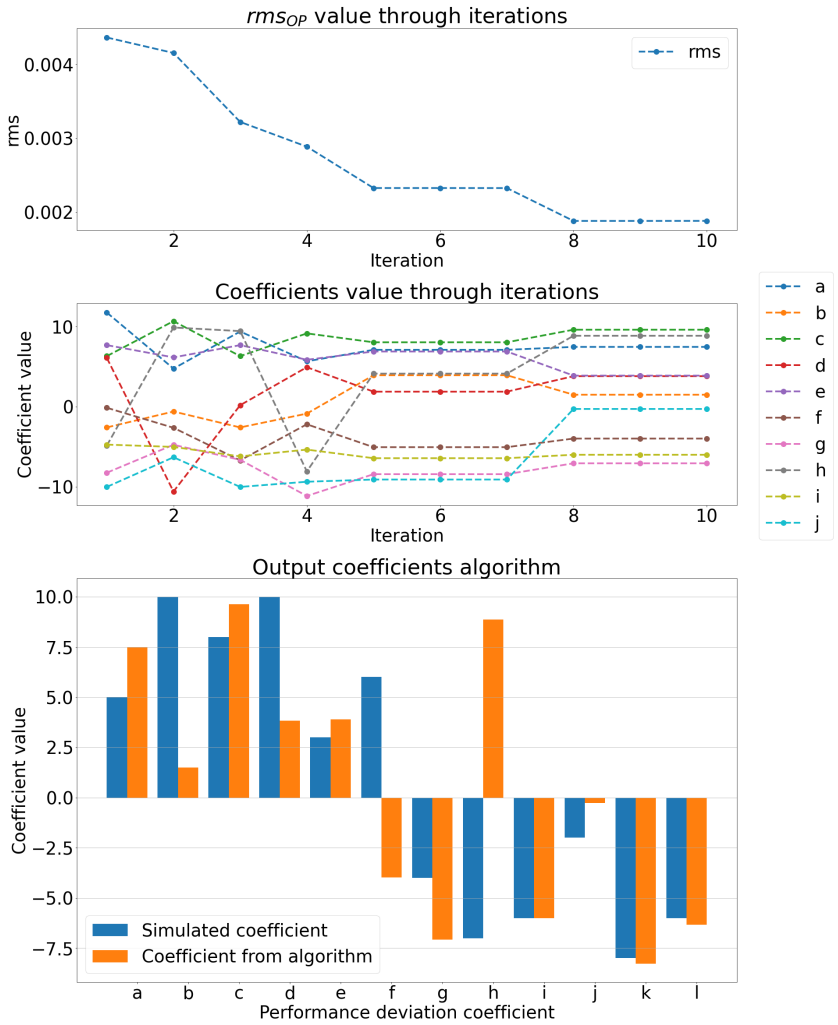

Figure C.5: Optimiser results from unbounded algorithm

D

Sensitivity analysis algorithm

To indicate the effect of varying the algorithm settings, this appendix contains a sensitivity analysis. In this analysis, one parameter is changed and the other parameters are kept constant.

The constant baseline values are displayed below:

- CR=0.7
- F=[0.5,1]
- NP=5
- Q=10
- OP=30

The results are judged by capturing the rms_{OP} and the rms_{curves} of the last iteration. Also, the running time is evaluated. The results from this analysis are displayed in Figure D.1. The results are plotted against the changed algorithm parameter.

Crossover constant
The crossover constant CR determines the chance that a variable from the target vector is replaced by the variable from the mutant vector to form the trial vector. A large CR decreases the number of generations it takes for the algorithm to converge but will decrease the variety in the populations. A small CR will lead to slower convergence but will therefore enhance the search in a wide solution space to prevent local minima convergence. As changing CR does not change the running time of the algorithm, the best performing value can be chosen without compromising on run duration. The lowest rms_{OP} value is found for a CR of 0.5. However, the lowest rms_{curves} is found for a CR of 0.9. Since rms_{curves} is the measure of the actual ability of the algorithm to reproduce the SPP relations, this is the leading variable to judge the performance. So a CR of 0.9 is the most logical choice. But, the difference in rms_{curves} between the two CR values is small and a higher CR increases the chance of getting stuck in a local minimum. Therefore, the choice is made to favour the CR of 0.5 over 0.9. Accordingly, this value will be used during the case study.

Amplification factor
The amplification factor F determines the strength of the mutations. With a low amplification factor, fast convergence takes place. A high amplification factor slows down convergence but increases the searching radius. F is a value between 0 and 2 and is specified in the algorithm as a range between two values. The algorithm randomly selects a value in the specified range to use as the amplification factor for a certain generation.

As $F = [1, 1.5]$ yields the lowest rms_{curves}, this seems the logical choice. But the corresponding rms_{OP} is very high indicating that the algorithm has not converged. Therefore, this rms_{curves} value is not expected again if the algorithm was run again. So, the choice is made to use $F = [0.5, 1]$, which is accompanied by a low rms_{OP} and rms_{curves}.

Maximum iterations
The maximum number of iterations Q influences the running time almost linearly, this is visible in Figure D.1. The effect on rms_{OP} when going from Q=5 to Q=10 is most pronounced. The effect of going from Q=10 to Q=15 is negligible. The effect of Q on rms_{curves} is clear, more iterations means a lower rms_{curves}. However, additional iterations cost more time. Therefore, Q is kept at 10.

Operating points
The number of operating points OP at which the difference between the measurements and the model output is calculated, is also specified by the user. Again the algorithm running time is influenced by the number of evaluated operating points. There is no clear relation between rms_{OP} and the number of operating points. Also, there is a positive relation between rms_{curves} and increasing OP. Therefore it is kept at 30.

Population size
The population size NP determines the number of target, trial and mutant vectors created. More vectors enlarge the searching space within one iteration but will come at the cost of a longer computational time. Storn [46] suggest using 5 to 10 times the number of variables in the optimisation. Again there is no clear relation between NP and the rms_{OP} and rms_{curves}. Therefore, the choice has been made to use 5 times the number of variables. So for optimisation of 12 variables, $5 \cdot 12 = 60$ trial vectors will be tested per generation.

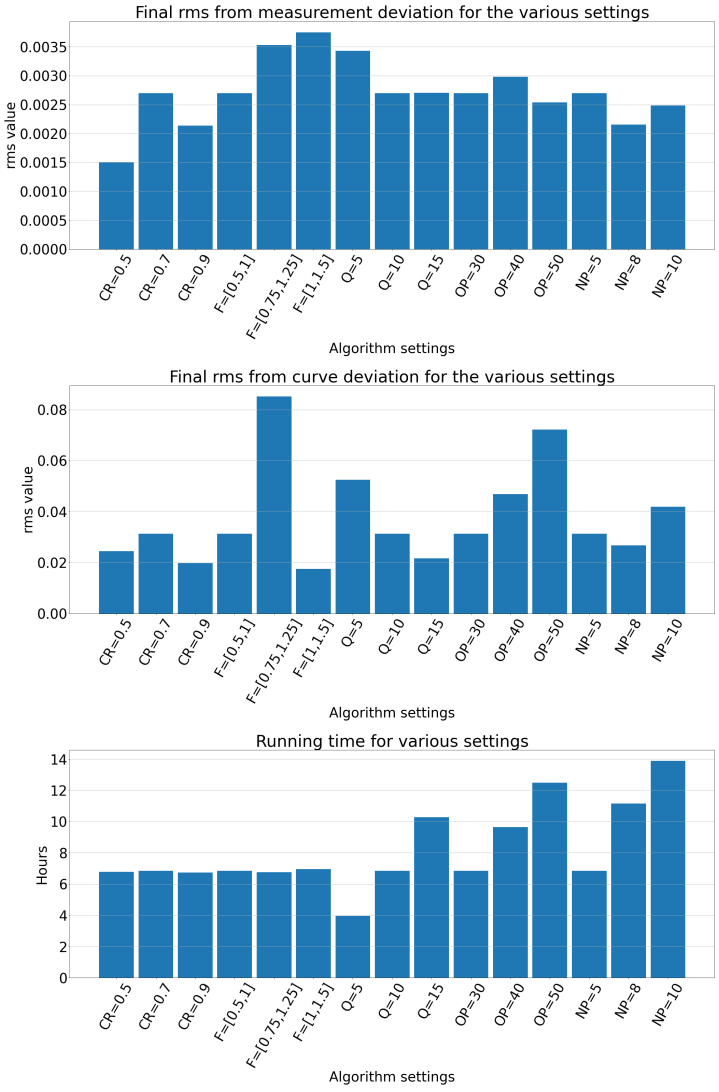

Figure D.1: Final rms value and running time from sensitivity analysis

E

GSP input & data pre-processing

This appendix explains how is dealt with further on-wing effects and data pre-processing.

E.1. Input parameters in GSP

The on-wing situation changes the environmental conditions. How these effects are treated, is introduced in this section. The effect considered are: the humidity effect and the inlet.

E.1.1. Humidity effect

As mentioned in subsection 3.3.2 the humidity plays a role in GPA. Since the cruise altitude is above 6000m, the absolute humidity at cruise is taken as 10%.

E.1.2. Inlet

The inlet bellmouth in the test cell is different compared to the on-wing inlet situation. This can lead to less accurate GPA results from on-wing data because the test cell model is calibrated with test cell data. However, as input to the model, $P_{t,2}$ is used. This parameter takes the different inlet into account since it measures the total pressure at the fan face.

E.2. Data pre-processing

Besides on-wing effects, on-wing data also introduces other uncertainties. The uncertainties discussed are the measurement error, operational steady-state assumption and thermal steady state assumption. To overcome them, data pre-processing is required. How this is performed, will be discussed in this section.

E.2.1. Measurement error

The sensors of the GEnx-1B engine all have their accuracy and range. Since the measurement error of these sensors can propagate through into the GPA results, it is of interest to know their accuracy. The range of the sensors en accuracy is visible in Table E.1. In section 4.4, an analysis was performed with noisy data. The algorithm proved capable of working with noisy data. Therefore, no sort of filtering is applied.

Sensor	Accuracy	Units
N1,N2	±0.12	RPM
W_f	±3.5% of measurement	pph
$T_{t,12}$, $T_{t,25}$, $T_{t,3}$, $T_{t,49}$	±0.4% of measurement	$^\circ C$
$P_{t,2}$	±0.01	psia
$P_{s,3}$	±0.36	psia

Table E.1: Accuracy of sensor set GEnx-1B engine [9, 10]

E.2.2. Operational steady-state

A steady-state point is needed to perform the GPA. In the on-wing situation, the snapshots already provide a near steady-state point, but the CEOD also contains lots of transient data. To perform a thrust worthy steady-state analysis, the data point should be free of the transient effects. This is done by filtering for values of a low ΔN_2, as this data is available in the CEOD. A value of $\pm 0.05\% \Delta N_2$ is used to filter out the transient points.

E.2.3. Thermal steady state assumption

As mentioned in subsection 3.3.3 GPA assumes a certain steady thermal state of the engine. During on-wing take-off, this assumption does not always hold. As CEOD offers the possibility to use mid-flight cruise data, thermal stabilisation can be assured. A thermal steady-state point is satisfied by filtering out operating points that are within one hour from take-off.